Sede Amministrativa
UNIVERSITÀ DEGLI STUDI DI MODENA E REGGIO EMILIA

Dottorato di Ricerca in Fisica
XIX Ciclo

Hall probes magnetometry for the study of molecular nanomagnets

Andrea Candini

Relatore: Prof. M. Affronte

Tesi presentata per il conseguimento del titolo di Dottore di Ricerca

Contents

Chapter 1

Introduction

The ability to understand, predict and control the properties of matter in reduced dimensions is the crucial key for the design and development of future technology. When magnetic materials reduce in size we may actually observe a crossover from classical to quantum behavior and new theoretical and experimental tools are required. The challenge is therefore to find and exploit novel phenomena.

The approach to magnetism at the nano scale is two-fold: one aspect is material engineering, to design and create novel materials those properties are experimentally characterized and theoretically predicted; the other approach is the simultaneous development of innovative techniques, to prepare, study and even manipulate these samples down to the smallest scale.

From the point of view of material engineering, molecular magnets are fascinating since they offer the opportunity to control magnetism starting from the very bottom, i.e. at the molecular level. In addition, their truly reduced dimension (≈ 1 nm) makes it possible to observe novel phenomena due to the quantum mechanical nature of the spin systems: quantum tunnelling of the magnetization, spin states superposition, quantum coherence etc. . . .

On the experimental side, Hall micro-probe magnetometry is considered an appealing technique, since it is one of the few showing high field sensitivity, in a reduced dimension (1 μm or even below) and almost without any limitation in temperature or applied fields. Current state of art Hall sensors have enough sen-

sitivity to detect individual magnetic nano-dots. More interesting, the possibility to develop probes with lateral sizes in the $10 - 100$ nm range can provide true nanometer-scale devices, with enough sensitivity to measure even single molecules or single spins.

With this thesis I develop the use of the Hall probe magnetometry technique for the study of novel families of molecular nanomagnets. During my work, indeed I have implemented Hall micro-probes magnetometry in a commercial Quantum Design PPM-system and employed this set-up to measure the magnetization of small crystals ($10 - 100$ μm in size) of molecular magnets. In addition, I've developed Hall nano-sensors that can be used as ultra-sensitive magnetometers.

This thesis is organized as follows: I will firstly introduce the reader to molecular nanomagnets and to Hall probe magnetometry, then in **Chapter 2** the whole experimental set-up will be presented and finally **Chapters 3-6** will be dedicated to show part of the results I obtained. In **Chapter 3** I will describe the fabrication and characterization of Hall nano-probes with lateral size as small as 100 nm and high flux sensitivity, obtained by focused ion beam milling; **Chapters 4-6** will concern about my research on molecular nanomagnets. The high magnetocaloric effect of Fe_{14} molecular cluster and the tunability of competition between dipolar coupling and single molecule anisotropy in Fe_{17} nanomagnet will be discussed in **Chapter 4**. In **Chapters 5** and **6** I will respectively present our characterization of linked antiferromagnetic molecular rings that can be used as quantum gates for quantum computing and of a new family of molecular clusters (Ni_{10}) showing very slow dynamic at high temperature that can not be explained within the usual framework of phonon-assisted relaxation. In the final **Chapter** (**7**), general conclusions of the work and future perspectives will be discussed.

1.1 Molecular Nanomagnets

The chemical approach to material science offers a reliable way of designing and assembling materials in which the properties can be tuned at the molecular level. Molecular magnetism certainly plays an important role in the study of molecule-based materials [1]. This field, born in the beginning of the 70's, is continuously attracting increasing interest, and it is now become a rich research topic, thanks to the efforts and nice results of many groups, both chemists and physicists. Among the current trends in molecular magnetism, a primary part is taken by the study of oligonuclear compounds that behave like small magnets: the so-called molecular nanomagnets [1].

Nanomagnetism is defined as the discipline dealing with magnetic structures of sub-micron dimension; it is a rapidly expanding area of research that appears able to provide a large number of novel applications, from high density magnetic media, to new type of devices where the charge property of the electron is combined with its spin (i.e. *spintronic*) [5, 6]. Magnetic molecules represent the ultimate possible size of a nanomagnet, providing a unique opportunity to observe the coexistence of classical and quantum properties.

Molecular nanomagnets, the prototype of which is considered the Mn_{12}-acetate molecule [7–9], consist in clusters of a finite number of magnetic centers (transition-metal or rare-earth ions, or even organic radicals) strongly coupled with each other, surrounded by shells of ligand molecules. The resulting *intra*-cluster interactions far exceed *inter*-cluster ones, such that every magnetic molecule can be considered a single (nano)-object. Usually these molecules are well ordered, forming crystals of macroscopic sizes. These materials are thus in between the macro- and microscopic world, since macroscopic measurements can give access to the properties of the single molecule (ensemble average), governed by the laws of quantum mechanics. Molecular nanomagnets are to date the best candidates to observe quantum effects in magnets, such as the tunnelling of the magnetization.

[1] Exhaustive reviews about the topic of molecular nanomagnets can be found in References [2–4]

Because of these fascinating properties, these materials can be employed for completely new types of devices and applications, such as quantum computing [10] or magnetic molecular junctions [11]. In this thesis, I have studied properties of novel families of molecular nanomagnets with different purposes: ferric clusters with large total spin and small anisotropy, where the magnetocaloric effect and the interplay between dipolar coupling and single molecule behavior have been studied (Chapter 4); antiferromagnetic molecular rings linked together to perform quantum logic gates in quantum computing (Chapter 5) and a decanuclear Ni-cluster showing slow relaxation of the magnetization at high temperatures (Chapter 6).

1.2 Hall micro-probe magnetometry

The ability to fabricate and control properties of nano-scale magnetic structures has brought not only to the discovery of several new physical phenomena and possible future industrial applications, but also the development of a large number of experimental techniques to investigate 'nano-objects'. Among them, Hall micro-probe magnetometry is a very appealing one, being non-invasive and offering high field sensitivity in a reduced dimension, with almost no limitations in temperature and magnetic field. Firstly, I will briefly introduce the Hall effect and then the main characteristics of a Hall magnetometer will be discussed, including a short review of Hall probes presented in the literature.

1.2.1 The Hall effect

In 1879 Edwin H. Hall found that when a charge current is placed in a perpendicular magnetic filed, a transverse voltage (known as Hall voltage) appears, due to the Lorentz force on the charge carriers. The experiment is depicted in Figure 1.1 and it can be described within the framework of Drude model: the current is flowing through the material strip in the x-direction and a magnetic field $\boldsymbol{B}$ is applied along z; the force acting on the charge carriers can be written as [12, 13]

$$\boldsymbol{F} = q(\boldsymbol{E} + \boldsymbol{v} \times \boldsymbol{B}) \tag{1.1}$$

where q is the charge and $\boldsymbol{v}$ the drift velocity of the carriers: they are deflected by the Lorentz force toward the negative y-direction, generating the electrostatic potential E_y that prevents further accumulation. In stationary conditions, $eE_y = ev_xB_z$ with the current flowing along x. The Hall voltage is thus given by

$$V_{\mathrm{H}} = wE_y = v_xB_z = \frac{j_xB_z}{ne} \tag{1.2}$$

where w is the width of the conductor, j_x the current density along x and n the charge carriers density. Since $\boldsymbol{j} = I/wd$ (d is the thickness), the final relation is obtained

$$V_{\mathrm{H}} = R_{\mathrm{H}}IB_z \tag{1.3}$$

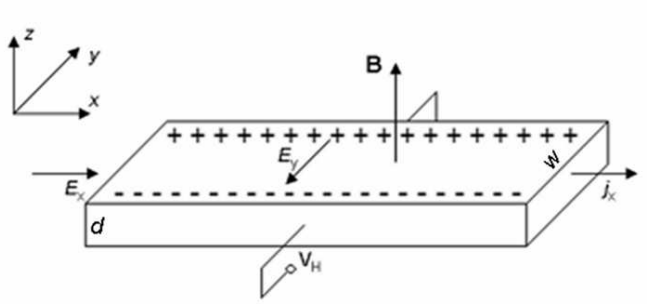

Figure 1.1: Schematic view of Hall's experiment

having defined the Hall coefficient R_{H} as

$$R_{\mathrm{H}} = \frac{E_y}{j_x \boldsymbol{B}} = \frac{1}{ned} \tag{1.4}$$

The Hall voltage V_{H} turns out to be proportional to the magnetic field and the current, and inversely proportional to the carrier density n of the conductor. Thus, the Hall effect can be used to determine n and the sign of charge carriers in a material, that is related to the shape of the Fermi surface in the framework of electronic band theory.

1.2.2 Hall devices

If n the density of charge carriers is known, the Hall effect can also be used to measure the magnetic field[2]. The simplest geometry for an Hall probe (i.e. the Hall cross) is seen in Figure 1.2. If a magnetic object is placed near the active area of the probe, then the Hall signal will be proportional to the sum of the external field $\boldsymbol{B}$ and the magnetic *stray field* coming from the sample and enters in the *active area*. Considering the geometry of Figure 1.3, it can be seen that this field is related to the magnetization. This constitutes the basis of the Hall probe magnetometer.

Depending on the mobility of the charge carriers and the temperature, there are two regimes to take into account: *diffusive* transport when the mean free path

[2]it actually measures the magnetic flux density

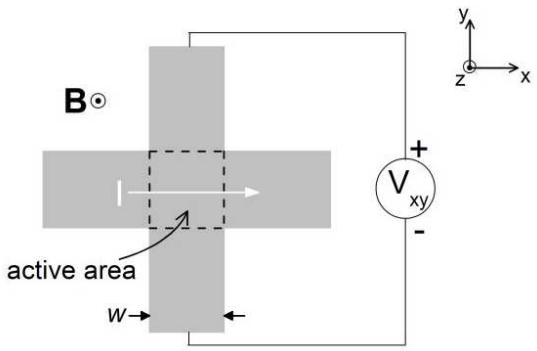

Figure 1.2: The Hall cross. The output signal is the Hall voltage V_{xy}, proportional to the driving current I and to the perpendicular component of the field $\boldsymbol{B}$ that enters in the active area of the probe.

of the charge carriers is much less than the size of the Hall cross, and *ballistic* transport when the mean free path is much larger of the probe's size. In the ballistic regime, charge carriers do not scatter while they are in the probe active area. It has been calculated [14] that the Hall response is determined simply by the *average* of the magnetic field in the intersection between current and voltage leads, even in the presence of an extremely inhomogeneous field. Conversely, in the diffusive limit, the Hall effect in an inhomogeneous field is usually computed by several techniques [15, 16] and it turns out that it depends on the specific geometry of the active area [15]. However, in both the limit cases of homogeneous and extremely inhomogeneous field the response function is always proportional to the *average* field, and, considering a symmetric cross, approximatively doubles the effective area of the probe [15, 16].

Thus, Hall sensors are actually fluxmeters, as in the case of SQUIDs magnetometers.

Sensitivity

The magnetic *field* sensitivity of a Hall sensor (usually indicated with B_{min}) expresses the minimum magnetic field, averaged in the whole active area, that can be detected. It is defined as the ratio between the Hall signal $V_{\mathrm{H}} = IR_{\mathrm{H}}\boldsymbol{B}$

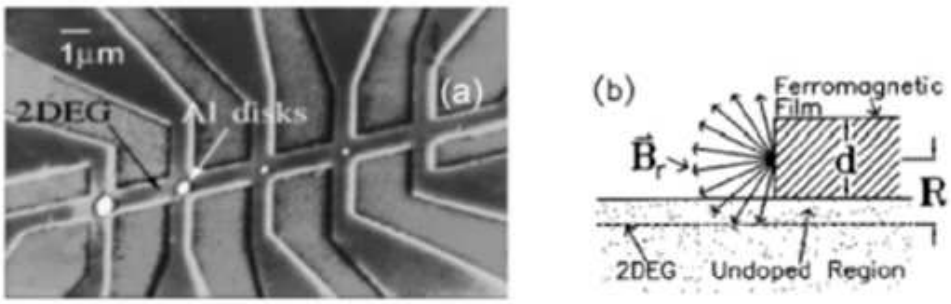

Figure 1.3: Two examples of Hall probe magnetometer. (a) The Hall device senses the external field plus the magnetization of the sample ($4\pi M = B - H$), and one probe is left empty for reference. (b)The Hall voltage as a function of an applied external field is due to the stray field (proportional to the sample's magnetization) that penetrates the active region, in this special case a 2DEG layer. Figures taken from References [20](a)and [41](b).

and the electrical noise present in the measurement.

$$B_{min} = \frac{\sqrt{{V_{\text{Johnson}}}^2 + {IR_{\text{noise}}}^2}}{IR_{\text{H}}} \tag{1.5}$$

where the two major contributions to the voltage noise are considered. $V_{\text{Johnson}} = \sqrt{4k_{\text{B}}TR_sf}$ (where $k_{\text{B}}T$, R_s and f are thermal energy, series resistance of the device and the measurement bandwidth, respectively) is the so called intrinsic or thermal noise and arises from the resistance of the voltage leads; IR_{noise} is a resistive noise that manifests itself as telegraph noise in the time trace of the Hall signal and has a $1/f$-like component in the frequency domains. It is probably due to fluctuations of the total resistance of the device [17].

As it can be seen in Equation 1.5, the Johnson noise can be suppressed increasing the value of the driving current I, but, above a certain value, the resistivity noise becomes the dominant one. In addition, also self heating effects (I^2R) impose constraints on the value of I. It turns out that there is an optimal value for the driving current (I_0, material dependent) that minimize the noise. Under this condition, B_{min} can be related to the physical parameters of the sensor, solving the equations that governs the behavior of the Hall effect [12, 15]. In

particular [18]

$$B_{min} \propto \frac{1}{\sqrt{n\mu}w\sqrt{d}} \tag{1.6}$$

being n and μ the density and mobility of charge carriers and w and d the width and thickness of the probe. Generally speaking, the field sensitivity increases with the mobility of the conductors, while it worsens scaling down the size of the probe. This can be simply understood since smaller probes and material with low carriers mobility usually have show high resistance values, thus increasing the sources of electrical noise.

Commercial high field resolution Hall probes are made of high mobility semiconductors (usually InSb for room temperature applications, GaAs/AlGaAs two dimensional electron gas (2DEG) for low temperatures). These materials are chosen for the special combination of low density of charge carriers and high mobility. The small value of n gives high Hall coefficient since $R_{\mathrm{H}} \propto 1/n$, while high mobility μ means smaller resistance. Standard probes with lateral width from 100 μm to some mm and can detect magnetic signals $B_{min} \lesssim 1$ nT/$\sqrt{\mathrm{Hz}}$ [3].

Application

Hall effect sensors are being used in industrial applications as proximity switching, position and current sensing and speed detection from the second half of the 20^{th} century. Conventional Hall probes are currently the most used devices for high precision magnetic field measurements.

In recent years miniaturized Hall probes have been widely employed as ultra sensitive magnetometers [19, 20]. Micro and submicron probes have also been mounted on scanning microscope systems, originating a new magnetic imaging technique, called scanning Hall probe microscope (SHPM) [21, 22]. Hall probe magnetometers and scanning microscopes have been successfully used to investigate properties of individual magnetic nanoparticles and their arrays [19, 20, 23–28], vortices and flux distributions in superconductors [29–32], magnetic domains and domain walls [33–37]. Other applications in which Hall probes

[3] see [18] and references therein

can be employed are detection of magnetic microbeads for bio-chemical applications [38,39], and imaging and development of new high density magnetic recording media [40–42]. Recently, also the detection of magnetic resonance signals with an Hall sensor as the sensitive element has been demonstrated [43, 44].

Hall micro-probes and nano-probes

Miniaturized Hall sensors are usually made of GaAs/AlGaAs 2DEG systems, have lateral sizes in the micron (or even sub-micron) scale and typical field sensitivity ranging from 10^{-6} to 10^{-8} T/$\sqrt{\text{Hz}}$ below $\approx$ 100 K [19, 20, 22, 31], while lower carriers mobility and higher resistance limit this sensitivity to 10^{-4} T/$\sqrt{\text{Hz}}$ at room temperature [17, 45, 46]. Even if the *field* sensitivity is worse than for larger probes, reduced sizes offer a better coupling with the magnetic signal originated by the sample, that in the dipole approximation decreases as $1/r^3$. As already pointed out, the Hall voltage is proportional to the average field in the whole active area, hence smaller sensors optimize flux trapping and can be used to measure small magnetic objects.

To exemplify this concept, let consider a *field* sensitivity of $\delta B \approx 10^{-8}$ T/$\sqrt{\text{Hz}}$ in a probe with size $w \approx 1$ μm: this means a *flux* sensitivity $\delta\Phi \approx 10^{-5}\Phi_0$ ($\Phi_0 = h/2e = 2.07 \times 10^{-15}$ Tm^2) and a *moment* sensitivity [4] $\delta m \approx 10^3$ μ_B [20]. A better field resolution ($\delta B \approx 10^{-9}$ T/$\sqrt{\text{Hz}}$) but in a probe with $w \approx 10$ μm would result in a *flux* sensitivity $\delta\Phi \approx 10^{-4}\Phi_0$ and finally in a much worse *moment* sensitivity $\delta m \approx 10^6$ μ_B.

It has been predicted [20] and recently also calculated [47] that the ultimate limit for the moment sensitivity of an Hall sensor can be even a single electron. However, up to date, the smallest magnetic signal detected still $\approx 10^5$ μ_B [27], while a (10^3 μ_B sensitivity has only been calculated with currently state-of-art systems [20]. Major difficulties arise from the need to reduce the sensor width to the nanometer scale: indeed to match the flux created by a single spin of moment $m = 1$ μ_B the sizes of the probe should be shrinked down to ≈ 10 nm, maintain-

[4] with moment sensitivity is intended the smallest magnetic moment that can be detected by the sensor

ing the same field sensitivity. Miniaturization of Hall devices to less than 100 nm would be also of great importance for scanning microscopy to obtain high spatial resolution, comparable to MFM technique. GaAs/AlGaAs heterostructures are limited by charge depletion, that drastically deteriorate their performances whenever the size is reduced. Even if 2DEG probes with effective active area of $\approx 0.25 \times 0.25$ μm^2 and noise level of 10^{-7} T/$\sqrt{\text{Hz}}$ below 77 K have been reported [31], controlling charge depletion that occurs at the side walls in this materials is still a difficult task, especially at room temperature.

To overcome the limitations of the GaAs/AlGaAs heterostructures many research efforts are being spent to investigate different materials and/or procedures for fabrication. The final goal is to combine spatial resolution in the nanometer range and high magnetic sensitivity, even at room temperature [17, 48–51].

Semimetal Bi films are usually considered a suitable alternative for 2DEG probes, due to their low carrier concentration and consequent large Hall coefficient [17, 46, 50, 51]. The smallest active area obtained so far with Bi films is $\approx 50 \times 50$ nm^2, with magnetic sensitivity of 0.8 G, which corresponds to a flux resolution of $10^{-5}\Phi_0$ [52]. Bismuth is however very sensitive to ambient atmosphere and this makes these probes very fragile. In addition, the electrical behavior of the Bi probe is found to be largely affected by growing conditions [17,50]. Metallic films can in principle be manufactured down to tens of nanometer [17]; the best results reported so far are Au probes with $\approx$500 nm and $\approx \Phi_0$ in term of lateral and magnetic flux resolution, respectively. Recently, Hall probes made of magnetic metals (Co) and fabricated by e-beam induced deposition, have been tested [53]; their large field sensitivity (10^{-5} T/$\sqrt{\text{Hz}}$) arises from the *extraordinary* Hall effect. Finally, also thin film of semiconductor materials can be a suitable alternative. The use of $\leq$100 nm thick films can overcome the problem of charge depletion, whereas high current I can partially compensate the loss of the Hall sensitivity $V_{\text{H}}/B = R_{\text{H}}I/d$ due to the film thickness d. Using thick films can in addition allow the detection of different field components [54]. It has been demonstrated that high quality InSb (that has a very high room temperature mobility) at 300 K has noise characteristics better than GaAs 2DEGs [39,51,55]. Best results include

micro probes with lateral size of 0.9 μm and $B_{min} = 6$ mG/$\sqrt{\text{Hz}}$ [56]. Researches on novel types of materials with very high room temperature mobility are still in progress [48,49]. In Chapter 3 I will report on the fabrication and characterization of probes with lateral size as small as 100 nm, made by focused ion beam milling of thin films of gold and of epitaxial gallium-arsenide.

Finally, mesoscopic Hall magnetometers with sizes ranging from few microns up to tens of microns can also be employed for study small magnetic crystals with dimensions of $\approx 10 \rightarrow 100$ μm^3. In the work described in this thesis, I used this technique to study properties of micro crystal made of molecular magnets [57–63].

Chapter 2

Experimental Techniques

In this chapter I will describe the experimental methods used during my thesis work. Firstly, I will briefly introduce the Quantum Design Physical Properties Measurements System and then describe how I implemented Hall micro-probe magnetometry using this apparatus. Finally I will describe the other techniques I employed to characterize the samples presented in this work: magnetometry (Section 2.3.1) and heat capacity (Section 2.3.2).

2.1 Quantum Design PPMS

Most of the measurements described in this thesis work have been performed using the Quantum Design *Physical Properties Measurements System* (QD-PPMS) present in the Low Temperature laboratory in Modena. This is a commercial system that allows to take automated measurements in a variable temperature range ($1.9 - 400$ K) and in magnetic field [64]. It consists of a liquid Helium cryostat and a programmable controller for data acquisition. Our cryostat is equipped with a 7 Tesla superconducting magnet.

Helium-3 system To achieve temperatures below 1.9 K we employed the Quantum Design Helium-3 system. This is a close cycle system, where a turbo pump is used to pump on ^{3}He condensed in a reservoir placed in the base of the

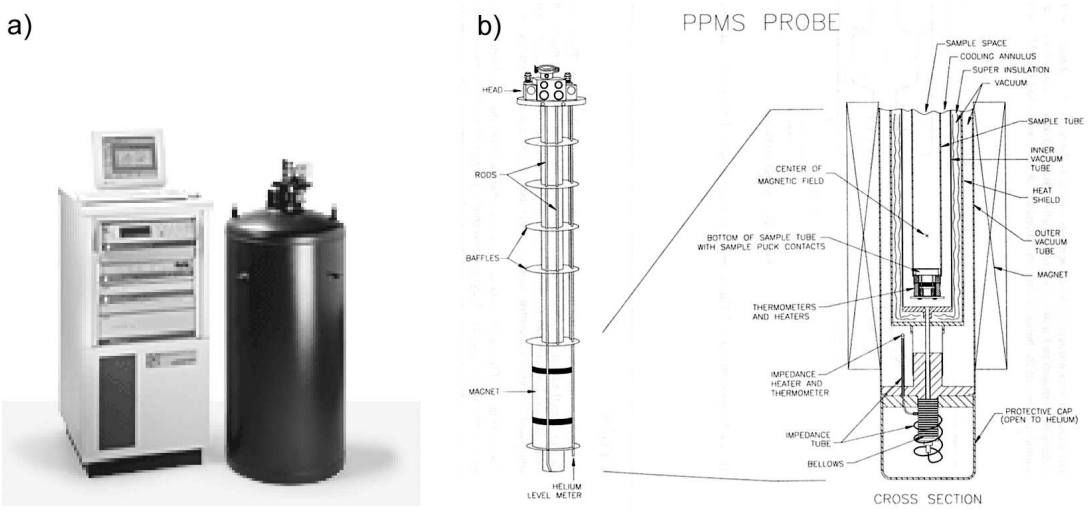

Figure 2.1: Quantum Design PPMS: dewar and controller (a) and schematic view of the probe (b). To control temperature, a vacuum pump drows helium into the annular region where heater warms the gas to the correct temperature. Magnetic field is applied in the vertical direction.

probe, thus reducing the temperature. For temperatures below 0.5 K a *one-shot* mode is activated, and all the circulating gas is condensed, closing the valve in the return line that during normal operations allows ^{3}He gas to flow continuously in the reservoir. In this way, the base temperature (≈ 0.3 K) is maintained for more than one hour.

2.2 Hall micro-probes

During my thesis work, I implemented the utilization of Hall micro-probes in the commercial PPMS apparatus. Combining them with the QD Resistance option P-400 results in a very sensitive magnetometer, capable to measure small ($\approx 10 - 100$ μm in size) magnetic crystals and maintaining all the characteristics of the PPMS (temperature and filed range and stability, automation of measurements etc...). In addition, Hall probes can be mounted in the ^{3}He insert, allowing access to temperatures down to ≈ 0.3 K. This constitutes an important improvement for the whole set up, since the standard magnetometry system

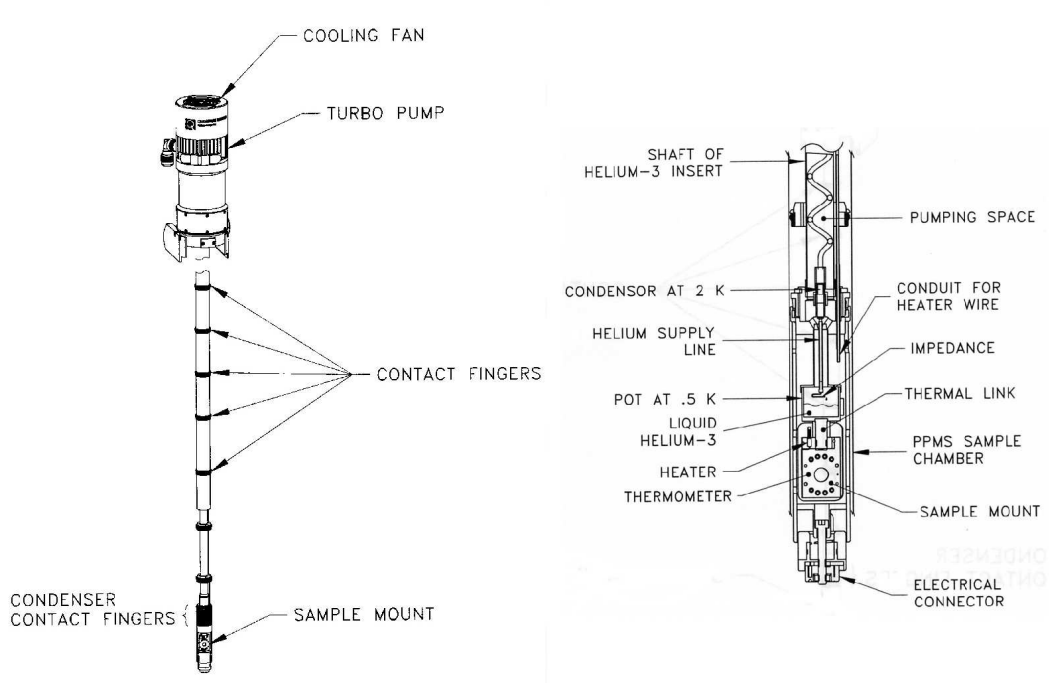

Figure 2.2: Quantum Design ^{3}He system: contact fingers assure thermal anchoring at the base temperature of 1.9 K. ^{3}He gas flows down the return line and condenses in the reservoir (where the turbo pump acts), that is thermally linked to the sample region. Temperature control is obtained by the combination of varying the speed of the pump and a sample stage heater.

(ACMS, see Section 2.3.1) is used with the liquid helium cryostat and hence is limited to ≈ 2 K.

The material chosen to fabricate the Hall devices is a GaAs/AlGaAs heterostructure with a two dimensional electron gas (2DEG) below the surface. This material has been widely employed for low temperature Hall magnetometry [19, 20, 57], for its extremely high SNR, originated by the desirable combination of small density n and high mobility μ of charge carriers. Until the lateral size of the probe is still in the micron range (in certain cases even hundreds of nm) magnetic signal of the order of 10^{-6} T can be easily detected, as reported in [17].

2.2.1 Fabrication and Characterization

The devices I use for magnetometry are fabricated by the group of Prof. L. Sorba at TASC laboratory, in Trieste. 2DEG heterostructures are grown by Dr. G. Biasiol using molecular beam epitaxy (MBE), while Dr. G. Mori, D. Ercolani and M. Tomaž make the lithographic processes.

Figure 2.3 shows the profile of the wafers. At the interface between GaAs and AlGaAs charge carriers are confined in a sheet of narrow thickness, showing two-dimensional properties. Above this 2DEG there is an undoped $Al_{0.3}Ga_{0.7}As$ spacer layer, followed by silicon-doped $Al_{0.3}Ga_{0.7}As$, that acts as electron donor for the electron gas. The spacer is needed to reduce impurity scattering and hence greatly improve the mobility. At top a GaAs cap is grown to prevent Al oxidation.

Photo-lithography and wet etching are then used to define Hall bar shape in the heterostructures and a second step of lithography is employed to put ohmic contacts to allow electrical connections to the 2DEG. Contact pads are made by evaporation of Ni-Ge-Au followed by thermal annealing at high temperature in a controlled atmosphere. During annealing Ge atoms diffuse deep in the wafer creating an ohmic electrical path to the electron gas. Figure 2.4 shows a scanning electron microscope (SEM) image of our probes.

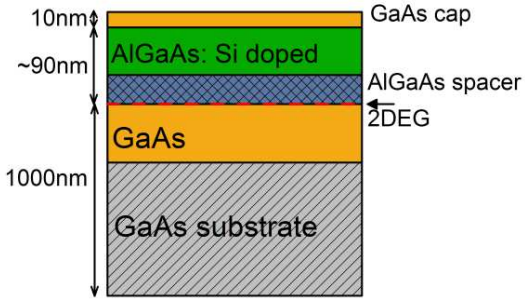

Figure 2.3: 2DEG structure of the wafers grown by MBE in the TASC laboratory, in Trieste. Starting from a commercial semi-insulating GaAs substrate, also a thick film of several microns is epitaxially grown to achieve good structure quality.

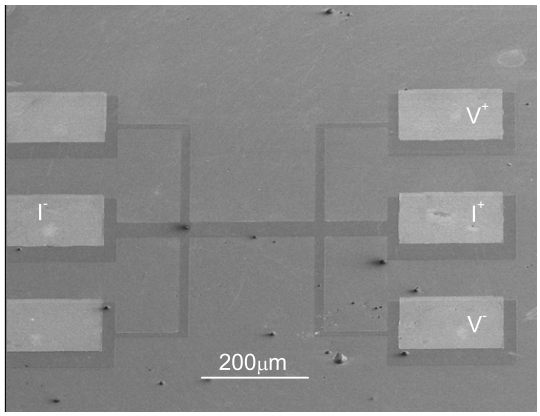

Figure 2.4: SEM image of standard Hall probes used for magnetometry. Active area sizes are 60×20 μm^2, the distance between the two crosses being 240 μm. Pads area is $\approx 200 \times 200$ μm^2. Electrical connections are also indicated.

The Hall response of the empty probes has been measured to characterize them. Typical results are shown in Figures 2.6 and 2.5, while in Table 2.1 they are summarized together with some physical properties of the electron gas. As can be seen, these GaAs/AlGaAs probes have constant Hall effect below ≈ 100 K and at low temperature the measured field resolution is 10^{-2} G.

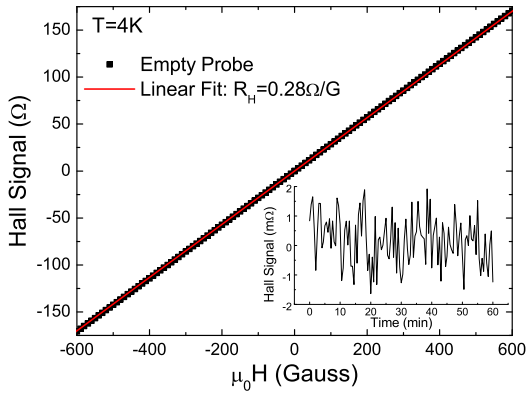

Figure 2.5: Typical Hall effect of our empty devices. Inset: measured Hall signal as a function of time. The peak to peak value of this trace can be considered as the *noise* level of the probe. With R_{H}= 0.3 Ω/G it results $B_{min} = 10^{-2}$ G. The current employed for biasing the probe was 10 μA (see Section 2.2.2)

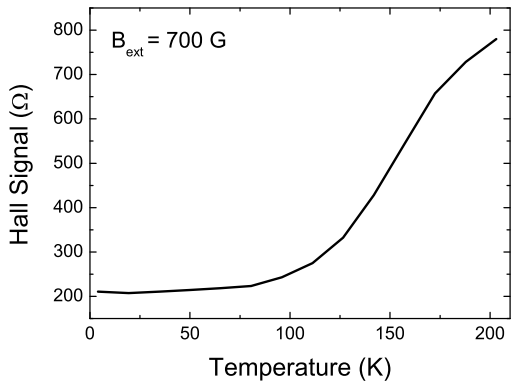

Figure 2.6: Typical Hall signal as a function of temperature for our devices. External applied field is perpendicular to the 2DEG plane . At low T R_{H} is independent of temperature. However, small deviations can occur and may become considerable when measuring tiny magnetic signals.

Table 2.1: Physical properties and results from the electrical characterization of the used Hall probes

Properties	**Value**
2DEG depth	$100 - 200$ nm
Carriers density n	$1 - 3 \times 10^{11}$ cm^{-2}
Carriers mobility μ	$10^5 - 10^6$ cm^2/Vs
R_{H}	$0.2 - 0.4$ Ω/G
measured B_{min}	10^{-2} G

2.2.2 Utilization

There are several aspects that have to be taken into account when using a micro Hall probe with the PPM-system. Here I review them, including some strategies I performed to optimize this technique.

PPMS Resistance option

Hall measurements can be simply made employing standard Resistivity P-400 option for PPMS. It consists in a four-wire resistance bridge, with up to three independent channels that can be used simultaneously. In a four-wire resistance measurement, current is passed though two *current* leads, while two separate *voltage* leads measure the potential difference.

The excitation current value can be set within the range ± 10 nA $-$ 5 mA, then the bridge reads the voltage drop and calculate the resistance. Bridge sensitivity is determined by the 20-bit analog/digital (A/D) converter, that already contains filter to automatically reject 50-Hz and 60-Hz line noise. Under typical conditions, noise level is around 20 nV, that means ≈ 20 $\mu\Omega$ with an applied current of 1 mA and ≈ 2 mΩ with $I = 1$ μA.

In the ac-mode the PPMS resistivity bridge generates a square wave signal with frequency $f = 8$ Hz. The calculated resistance is given by the average of the absolute values of the opposite voltage readings. In this way dc offsets can be eliminated.

Typical measurement times are around few seconds per point. When measuring as a function of some parameters (e.g. magnetic field or temperature) the system is stabilized in the desired conditions before starting the readings. Measurements made while continuously sweeping the field or rapidly changing the temperature are usually less accurate.

Sample mounting

Accurately positioning the sample in respect to the sensor is crucial to achieve good signal coupling and hence perform sensitive measurements. As can be seen

in Figure 2.7(a), the stray field originated by the sample's magnetization is maximum near the edge, and decrease rapidly with the distance ($\propto 1/r^3$ in the point dipole approximation). Thus the sample must be placed as close as possible to the probe's active area. A typical configuration is seen in Figure 2.7(b). Standard cryogenic grease (apiezon N) can be employed to glue the sample on the probe. Then the sample is moved to the desired position, for example using a thin and soft wire that works like a micro-tip. Particular care has to be taken to avoid damages to the 2DEG, since it is quite near the surface: a simple scratch may be enough to irreversibly deteriorate the probe behavior.

Usually, a chip of sizes $\approx 2 \times 2$ mm^2 contains a small number $(2-4)$ of almost identical Hall probes. The whole chip is glued to the PPMS resistance sample holder with silver paint, that assures good thermal contact. Shortcuts between different probes do not occur, since the substrate is made by several hundreds of microns of insulating GaAs.

A Kulicke and Soffa Model 4123 Wedge Bonder [65] is used to connect contact pads of the 2DEG probe to the ones in the sample holder. Since the resistance bridge performs four-wire measurements, four wires are connected to each probe, two for the current and two for the voltage, as evidenced in Figures 2.4 and 2.7.

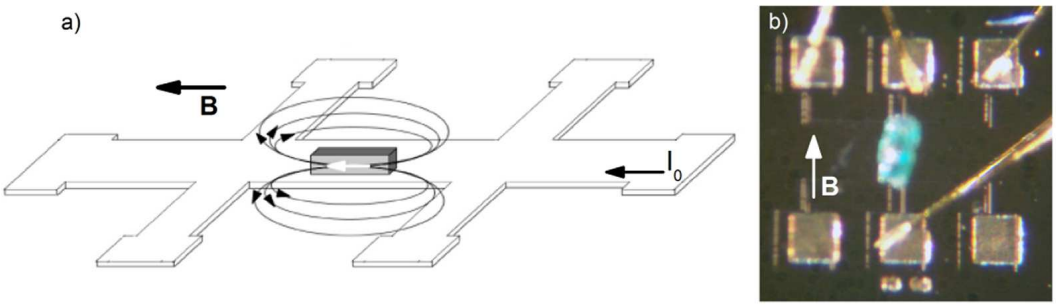

Figure 2.7: Typical sample mounting on a Hall probe. (a) Sample is magnetized by the external field and its stray field, proportional to the magnetization, is measured by the Hall sensor. (b) Picture of a Hall probe with a magnetic crystal on it. One edge of the crystal is aligned with the active area of the probe.

Finally the sample holder is plug to the insert and placed in the PPMS cryostat to perform measurements. Hall probes can be used in the PPMS liquid helium cryostat, employing standard Resistivity sample holder, the Horizontal Rotator probe or even a custom Multifunction Probe (model P-450), and in the ^{3}He system.

Although the geometry showed in Figure 2.7 is not the only possible one, it is preferable to have the external field in the same plane of the sensor. In this way the background signal is minimized (a small perpendicular component of the external field is always present due to not perfect alignment); in addition, this configuration avoid the occurrence of quantum effects at low temperature ($T < 10$ K) since the effective field sensed by the Hall probe is relatively small. When using the Helium-3 insert this geometry is imposed by the sample holder, otherwise the PPMS Horizontal Rotator option [64] can be used to align the sample holder with the magnetic field.

The Hall voltage is proportional to the magnetic flux density perpendicular to the probe's active area. Thus the measured signal is the sum of the stray field proportional to the sample's magnetization and the z-component of the external field. To subtract this background contribution, also an empty reference probe can be connected and signals of both sensors are measured simultaneously [1]. Since they belong to the same chip the two probes have very similar parameters and after subtraction only the signal from the sample is essentially left. Actually a small linear contribute may be still present, due to inhomogeneity of the charge density in the whole wafer. This is however a small error, typically of the order of 10^{-5} Ω/G.

Realization of a new insert for Hall probe magnetometry

Part of my thesis work was also devoted to develop a new insert dedicated to Hall probe magnetometry, to perform magnetization measurements in presence of electro-magnetic excitations (i.e. micro-waves and visible light). This allows to

[1] as already mentioned in Section 2.2.2 the resistivity option allows multiple channel measurements

study dynamic and switching properties of magnetic materials [58,61,66,67,114].

The whole insert is visualized in Figure 2.8. It is made by a commercial part (Quantum Design Multifunction Probe model P-450 for PPMS) and a *sample region* made in bakelite. Electrical connections are assured by twisted cryogenic wires (Lake Shore WQT-36-25), one side of which is soldered to connectors on the probe head, while the other extremity is glued to gold pads over the bakelite using epoxide silver paint (Epotek H20E). In this way Sn solderings, that at low temperature become superconducting and may originate magnetic flux detectable by the Hall probe, are avoided in the sample region. The Hall probe is hosted in a removable part, to perform wire bonding and sample mounting operations. A coaxial cable and an optical fiber directly bring E-M excitations to sample position from an external source.

The probe is biased with an ac-signal coming from a voltage source with a high resistance in series, to assure good stability. Frequency of the signal is around 1 KHz and the amplitude is set to obtain $I_0 \sim 10$ μA. On the insert head, a in-house built pre-amplifier is placed to amplify the Hall signal (gain is set equal to 100) and performing subtraction between the two voltage leads. The system is built to measure up to four channels simultaneously. Two channels are connected as shown in Figure 2.9; in this way, by subtraction of the two signals, contribution coming from the sample is enhanced, while background is minimized. Data acquisition is made by a phase-locked system (EG&G 5210 Lock In Amplifier), triggered with the voltage source, that also performs the final subtraction.

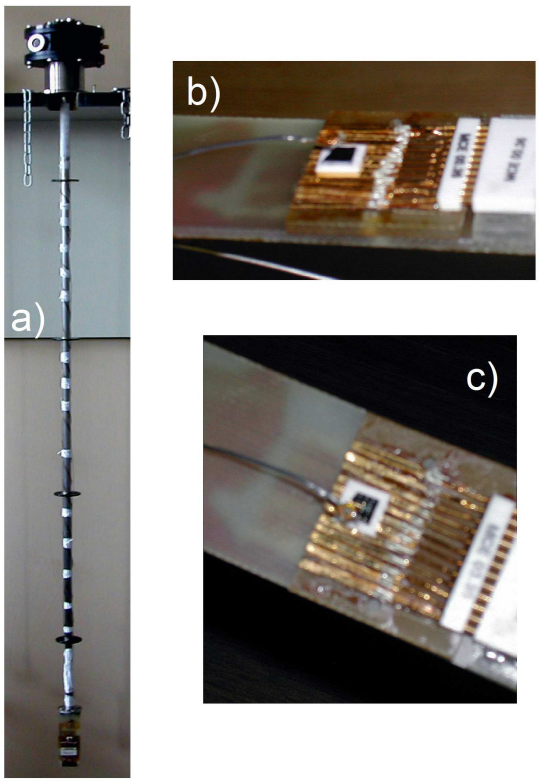

Figure 2.8: View of the Hall magnetometry dedicated insert. (a): the whole insert. (b) and (c): zoom of the sample area. Micro-wave antenna is also visible.

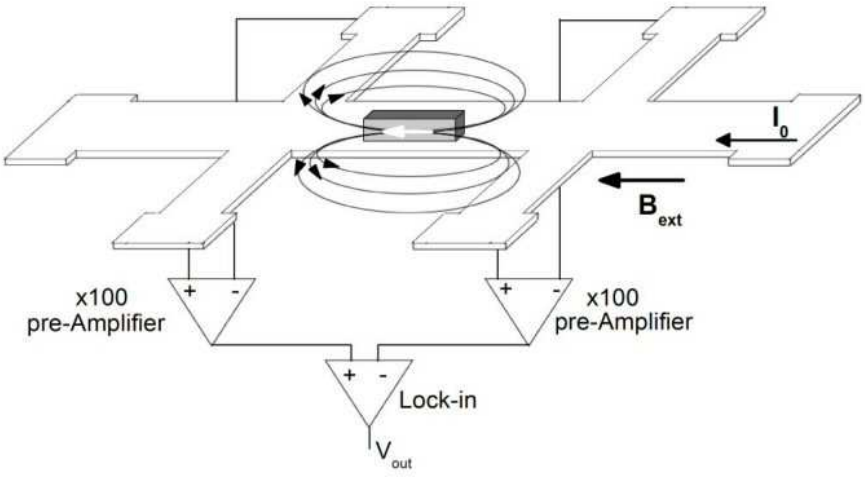

Figure 2.9: Schematic view of the electrical connections and geometry of the custom made insert. Pre-Amplifiers gain is set to 100. Up to four channels can be measured simultaneously. In optimal geometry, the sample fits exactly the distance between the two crosses: in this way after the subtraction performed by the lock-in, V_{out} is proportional to $2\times$ sample signal.

Biasing and Cooling

As already mentioned in Section 1.2.2 determining the optimal value for I_0 is crucial, since the Hall signal linearly depends on the current, but above a certain limit the probe behavior starts to deteriorate. Typically, the optimal value for biasing our probe was around 10 μA for ^{3}He temperatures, while it can be slightly higher (around 20 μA) for liquid helium temperatures up to $\approx$ 100 K. Currents of the order of tens of μA are expected for probes with sizes well above the micron scale.

Electron gas is a very sensitive element, and particular precaution have to be taken to optimize the performances of Hall measurements. Thermal shocks can seriously damage the probe; to avoid this problem, Hall devices have to be cooled and warmed very slowly, i.e. at a rate not higher than $2 - 3$ K/min and with a low value of the bias current (i.e. $I_0 < 1$ μA). Exposing the sensor to visible/infrared light at low temperature can help to recover best performances, by releasing carriers trapped in defects and impurities. However, very unlikely a Hall probe can maintain its behavior after few thermal cycles (4-5) and/or sample mountings (2-3).

Also drifts of the Hall signal are very often detected, likely originated by change of 2DEG's properties, like n or μ and consequently changes of the impedance and Hall coefficient R_{H} of the devices. To minimize these effects it is sufficient to let the system relax toward equilibrium for an appropriate time whenever some parameter that can affect the electron gas (e.g. temperature or driving current) are changed.

2.2.3 Test Measurements

The reliability of our Hall magnetometry technique has been tested measuring *well known* samples, to prove the sensitivity of the apparatus. Test measurements have been also performed exciting the samples with microwaves and visible light. Results are described in the following paragraphs.

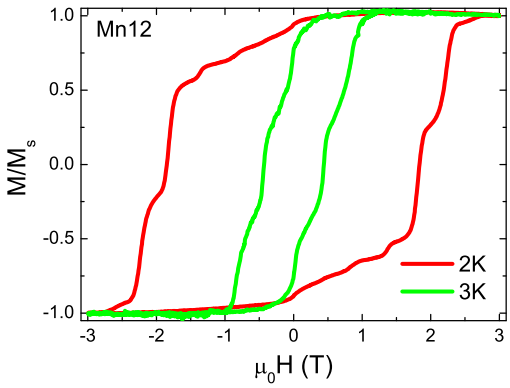

Figure 2.10: Hall probe magnetometry on a Mn_{12}-ac micro-crystal

Mn_{12} micro-crystal

Mn_{12} molecular magnet is a very well known system [2, 7–9], hence we tested our probes measuring small micro-crystals of Mn_{12}-acetate made by the group of Prof. A. Caneschi, Firenze. A 100 μm-sized single crystal was glued on the top of a probe, orienting its long side (that corresponded to the easy axis of magnetization of the Mn_{12}-ac molecule) along the direction of the magnetic field and aligning its short side to the edge of the active area. Magnetization measurements at different temperatures are shown in Figure 2.10. As it can be seen, the signal is very clean and the steps due to quantum tunnelling of magnetization are clearly observable, demonstrating the sensitivity and operativity of our set-up.

Mn_{12} thick film

Another challenging experiment was to measure magnetic signal from a *film* of Mn_{12}. Even if the deposition and study of molecular magnets on surfaces is of great importance for many applications and it is presently a field of intense researches [68–71], the detection of magnetic signals of molecular films is still a difficult task. At present time, with our Hall probe magnetometry we had enough sensitivity to detect the signal of a single drop of Mn_{12} solution (Mn_{12}-benzolate,

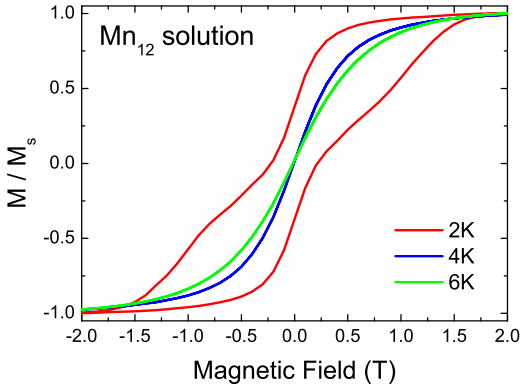

Figure 2.11: Magnetization measurements of a single drop of Bz-Mn_{12} solution casted on the top of the sensor. The result was a thick ($\approx$ few μm) film.

prepared by the group of Prof. A. Cornia, Modena) deposited directly over the sensor. This produces a thick Mn_{12} film that probably contained small crystallites, whose magnetic signal at different temperatures is shown in Figure 2.11.

Test with microwaves

Microwaves signal is powered by Anritsu generator MG3692B, a source that can provide signal from DC to 20 GHz with a power up to 20 dBm (i.e. 100 mW). A coaxial cable (LakeShore CC-SR-10) brings the signal directly to the sample position, and terminates with a small copper loop, acting as antenna. This cable is very thin (0.5 mm is the diameter of the shield) and made of stainless steel (both the inner and outer conductors). This makes it ideal for low-temperature applications, however electrical losses are considerable, especially at frequency above few GHz. Results obtained exciting a crystal of Mn_{12}-ac with different frequencies (Figure 2.12) are similar to those already present in literature [72].

For higher frequencies that those showed in Figure 2.12 we could not detect any change in the measured signal. We ascribed it to losses in the electrical line, that has a cut-off at $f > 2$ GHz. We are now implementing a slightly thicker coaxial cable made of both copper and stainless steel to minimize electrical losses.

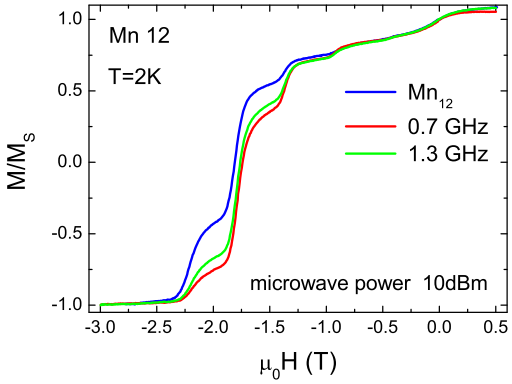

Figure 2.12: Magnetization measurements in the presence of microwave irradiation on the Mn_{12}-ac sample. Power at the source was 10 dBm. Effects of microwaves absorption on the magnetization tunnelling are clearly visible.

Test with visible light

Our light source is a 250W Quartz Tungsten Halogen (QTH) lamp (LoT Oriel Instrument); after which a monochromator is used to select the desired wavelength ($\lambda = 200 - 900$ nm); finally an optical fiber (multimode fiber, diameter $= 0.4$ μm) carries the electromagnetic signal into the probe down to the sample stage. The power with which the sample is illuminated has been measured to be ≈ 20 μW.

Preliminary measurements have been performed on a crystal of $MoCu_6$ molecular complex [73], provided by the group of Dr. V. Marvaud (Paris). Data shown in Figure 2.13 have been taken before and after irradiation for 1 hour at 10 K with blue light (510 nm). The effect of light is tiny, but a photomagnetic behavior is clearly observable. The use of laser as light sources (planned for the next future) will certainly improve the efficiency of this set-up.

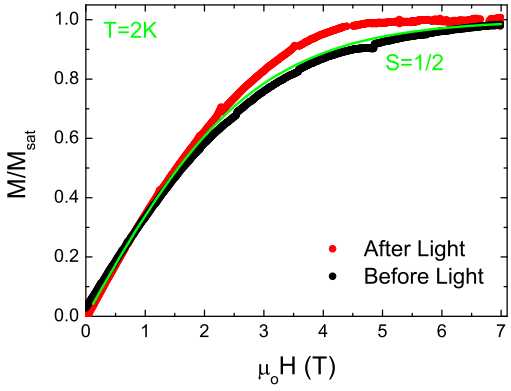

Figure 2.13: Photomagnetic effect on $MoCu_6$ molecular complex as measured with our Hall magnetometry set-up. Illumination was for 1 h at 510 nm. Effective incident light power was ≈ 20 μW.

2.3 Other Measurements Techniques

To characterize the samples studied in this work, I employed also other experimental techniques, mainly *commercial* PPMS options, that I will briefly describe in the following [2].

2.3.1 PPMS AC/DC Magnetometry System (ACMS) option

ACMS option allows to perform AC susceptibility as well as DC magnetization measurements.

ACMS set consists in concentric coils integral with the primary DC superconducting magnet. The primary coil provides an alternating excitation field by means of an ac current, while two secondary coils detect the change in magnetic flux due to the sample that is positioned in one of them. They are arranged in a first order gradiometer configuration (i.e. they are wound in counter sense) to reject background signals. A compensation coil is also wound around the driving

[2] for a more detailed description, we again refer to [64]

coil to reduce environmental noise, avoiding interaction with any material outside the measurement region (chamber walls, magnet core etc...). Quantum Design ACMS set also employs special calibration coils to precisely remove phase shifts coming from the detection apparatus and effectively separate sample signal from instrumentation effects.

DC measurements are made by means of the *extraction* technique. The sample is moved by the ACMS servo motor through the detection coils, inducing a voltage signal proportional to the magnetic moment.

Units Data measured by the PPMS acquisition program are given in units of *emu*, whereas the susceptibility χ and the magnetization M are usually expressed as *emu/mol* and $\mu_B/f.u.$ respectively. The necessary transformations are:

$$\chi(emu/mol) = \text{Data}(emu) \times \frac{\text{Molar Mass}(g/mol)}{\text{sample mass}(g) \cdot \text{excitation field}(G)} \tag{2.1}$$

$$\text{M(DC)}(\mu_B/f.u.) = \text{Data}(emu) \times \frac{\text{Molar Mass}(g/mol)}{\text{sample mass}(g) \cdot \mu_\text{B} \cdot \text{N}_\text{A}} \tag{2.2}$$

where in c.g.s. units μ_B and N_A are defined as 9.274×10^{-21} ergG^{-1} and 6.022×10^{23} mol^{-1}, respectively. The unit $(ergG^{-1})$ is equal to (emu).

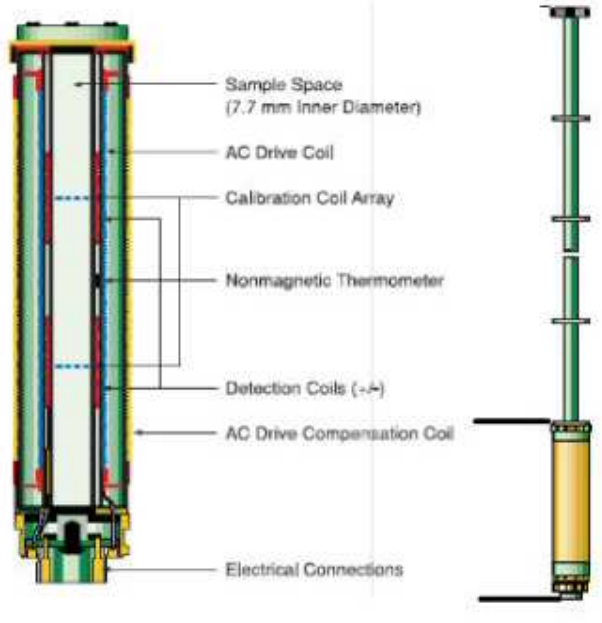

Figure 2.14: Quantum Design ACMS option.

2.3.2 PPMS Heat Capacity option

Measurement of heat capacity consists in measuring the temperature response of a sample to an applied thermal pulse. Quantum Design calorimeter is made by a small platform suspended by thin wires, where the sample is glued by Apiezon N cryogenic grease. The wires serve as electrical leads for the heater and the thermometer placed on the platform but also as a heat link between the sample and the thermal bath (a simple scheme is depicted in Figure 2.15).

Heat capacity is measured by means of the *relaxation* technique. After stabilizing the temperatures of the sample platform and puck, a small heat pulse is released to the sample for a given time t and then the temperature of the sample platform is monitored while it relaxes to the equilibrium with the thermal bath. If a power P is given and being K the thermal link to the heat bath, the heat capacity C is determined as

$$C = \frac{\tau}{K} \tag{2.3}$$

where τ is the time constant of the relaxation of the temperature:

$$\Delta T(t) = P \cdot R \exp\left(-t/\tau\right) \tag{2.4}$$

The above relation implies perfect thermal contact between sample and the calorimeter, however in most cases it is preferable to use the so called *two-tau model* that takes into account also the thermal relaxation coupling between the calorimeter and the sample itself. In this model two time constants are used to fit the relaxation of the temperature: τ_1 represents the thermal contact between the platform and the heat bath, while τ_2 the relaxation between the platform and the sample. Not surprisingly, the maximum fit quality, and hence the best measurement precision, is obtained in the quasi-exponential limit, i.e. $\tau_1 \gg \tau_2$. Indeed, a coupling factor is defined by the PPMS acquisition program as

$$c = \frac{\tau_1 - \tau_2}{\tau_1} \tag{2.5}$$

and good measurement are considered those with $c \gtrsim 90\%$.

Units Data acquired by the PPMS calorimeter are given in units of $(\mu J/K)$. To obtain the *molar* heat capacity and then normalize the data to the molar gas constant R this simple equation must be used:

$$\mathrm{C/R} = \mathrm{Data}(\mu J/K) \times \frac{\text{Molar Mass}(g/mol)}{\text{sample mass}(g)} \times \frac{1}{\mathrm{R}(J/mol\ K)} \tag{2.6}$$

where R = 8.315 J/mol K.

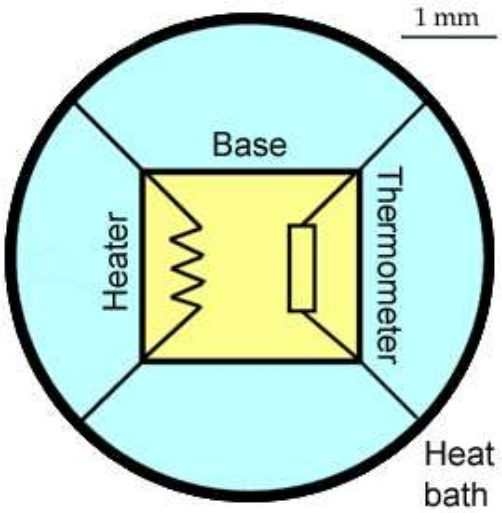

Figure 2.15: Scheme of the PPMS calorimeter. The sample is mounted on the suspended base, where both the heater and the thermometer are present. All the measurements are performed in vacuum and the base platform is connected to the thermal bath only through the four wires

Chapter 3

Hall nano probes fabricated by Focused Ion Beam

I have fabricated and charactetizated Hall nano probes made of Gold or Si-doped GaAs films and fabricated by Focused Ion Beam (FIB) milling. These Hall probes have lateral sizes of $\approx 100 - 200$ nm and hence are among the smallest reported in the literature up to date for these materials. The use of FIB milling technique is attracting increasing interest for fabrication of nano devices, since it allows quick and direct probe patterning by sub-micron resolution sputtering removal, avoiding the multiple-steps processing of conventional lithography. In addition, the possibility to design the active area at wish is a great advantage for nano scale applications where coupling between sample and sensor is crucial. I tested the Hall probes down to 4 K and discuss their performances in terms of spatial and magnetic flux resolution.

3.1 Procedures for fabrication

Thin films of gold with thickness d =100 nm were obtained by thermal evaporation at a rate of $\sim$1.6Ås^{-1} in vacuum ($\sim 10^{-6}$ torrs) on thermal oxidized silicon substrates. Gold was deposited at room temperature and post-annealing was found to be detrimental increasing the film resistivity. Silicon-doped gallium ar-

senide films were epitaxially grown by molecular beam epitaxy under ultra-high vacuum conditions on undoped GaAs(001) and the doping level was checked by Van der Pauw measurements at 1.4 K. The film thickness ranged from 1μm to 100 nm, the latter was used for the probes milled down to the smallest sizes.

Standard optical lithography was successively used to obtain probes with Hall geometry and 30-60 μm size, which were finally reduced below the micron-range by sputtering erosion using a focused ion beam system (FEI Strata DB235M FIB-Dual Beam)(seen in Figure 3.1). This system combines a FIB with a Scanning Electron Microscope (SEM) working at coincidence on the sample. This allows to monitor ion beam processing with simultaneous SEM imaging. FIB column is equipped with a Ga^+ source and has a minimum spot size of 7 nm at 30 keV, SEM column features a thermal field emission source and it has a 2 nm resolution over a wide energy range. Since the ion beam spotsize depends on the applied current, and this is directly related to the processing time, FIB patterning of the Hall probes was divided in two steps: a first coarse patterning at currents as high as 0.5 nA to reduce the width of the arms to few microns, followed by a fine patterning to reach the final sub-micron dimensions, using low current values (not higher than 30 pA). This two-steps procedure was essential to optimize the lateral resolution and produce uniform and symmetric active areas in order to avoid unwanted effects, like offsets in the transverse (Hall) signal. Figure 3.2 shows a SEM image of typical Au probe milled down to 100 nm of lateral size.

Few unpatterned probes were cut by FIB and the resistance of such gaps were preliminary measured in order to test the effects of gallium implantation. The resistance values were found to be of the same order of the substrates (GΩ for oxidized silicon under gold probes and MΩ for undoped GaAs), while the series resistances of the studied devices are up to tens of KΩ (for the smallest semiconducting probes). This made us confident that our sensors are not affected by undesired parallel conducting paths, which may have been generated by implanted Ga^+ ions.

Since As is easier to remove than Ga and the FIB machine works with Ga^+ ions, we found that the milling procedure causes an excess of gallium in the

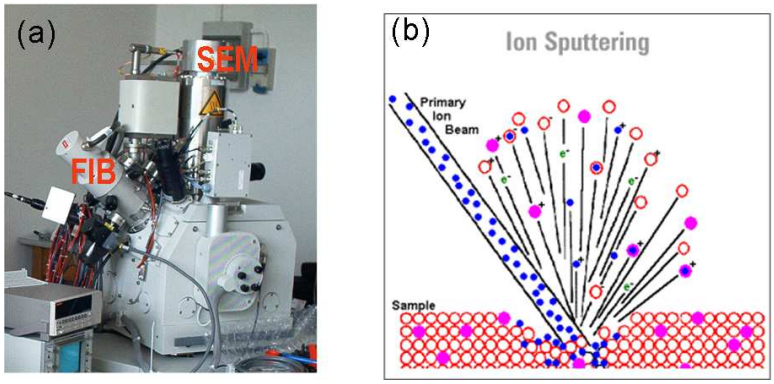

Figure 3.1: a) FEI Strata DB235M FIB-Dual Beam used in this work. b) Schematic view of the ion sputtering process.

machined GaAs samples, that is visible as droplets in the milled areas (see Figure 3.3a). This problem was overcome by introducing iodine gas (I_2) in the proximity of the sample through a micron sized needle during the milling procedure. As known, halogen gases form volatile compounds with Ga, increasing the milling rate and improving the cleanness of the structures by preventing redeposition and Ga droplets formation [74]. Figure 3.3b shows indeed that no Ga-droplets are present in the sample. Finally, because the milling rate increased by one order of magnitude, we could use the lowest current value (1 pA) without rising the working time.

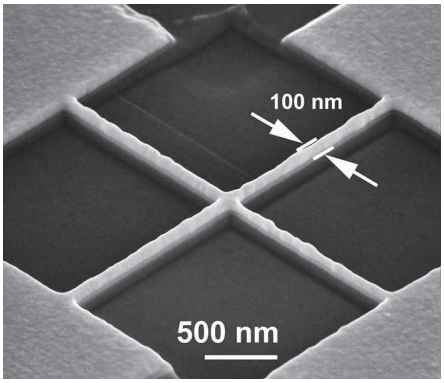

Figure 3.2: SEM image (tilted view) of a FIB milled Au Hall Probe (Probe Au#D, see table 3.1). Patterned active area is $\sim 100 \times 100$ nm^2. Film thickness is d =100 nm.

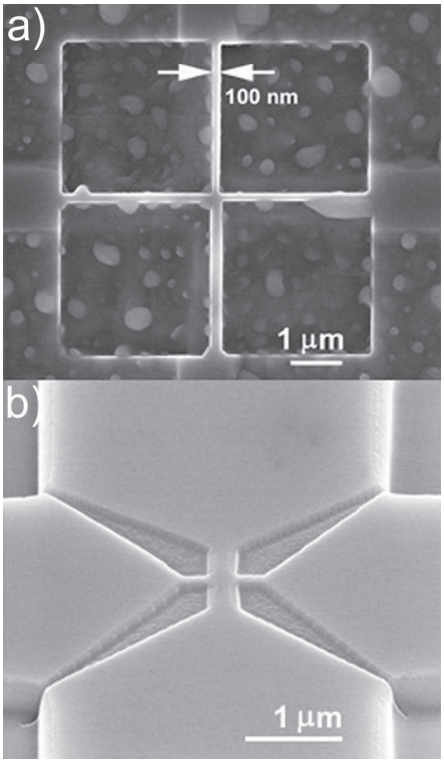

Figure 3.3: SEM image of FIB milled Si-doped GaAs Hall Probes without (a) (probe HM1329#A; see table 3.1) and with(b) the presence of I_2 gas in the working chamber during milling procedure. The width and thickness of the probe were $w \approx$100(a)-200(b) nm and d =100 nm, respectively. Note that image b) is a tilted view.

3.2 Electrical Measurements and Results

The Hall devices were electrically characterized in order to establish the minimum magnetic field (and flux) detectable by each type of probe. Electrical measurements were performed in our PPM System using either the internal P400 resistivity option or an external lock-in amplifier (see Section 2.2.2). It must be noticed that, due to the small size of the devices, ESD (electrostatic discharge) precautions must be taken during the bonding and measurement procedures to prevent electrical or mechanical damages.

The probes were excited with ac-current with intensity accurately selected to maximize the signal to noise ratio (SNR) and frequency spanning from 8Hz to 1KHz. The performances of each sensor were measured over a wide range of currents and optimal values were found to be up to 2 mA for gold probes and 20 μA for doped GaAs. Above these limits, non-linear and heating effects were indeed observed. The following figures summarize typical results obtained with our GaAs and Au probes. The Hall response to a perpendicular magnetic field and the corresponding noise (expressed as the Hall voltage as a function of time and calculated in term of magnetic field B) are shown as well. The level of noise (maximum peak to peak value), determined by our whole set-up, determines the minimum detectable field B_{min}.

3.2.1 Epitaxial GaAs Probes

The best signal to noise ratio at room temperature was found in Hall probes made of epitaxial GaAs. For this material, samples with different layer thickness and Si doping levels were grown and characterized. Results are summarized in Table 3.1. Since the ion beam has a Gaussian profile, the FIB milling procedure produces defects in the worked samples even in those regions at the border of the pattern area which are not directly milled, but fall within a half beam tail. This induces defects and depletion regions with a consequent reduction of the effective number of carriers n. An increase of the Hall coefficient R_H after milling is actually observed. This is also accompanied by an increase of the series resis-

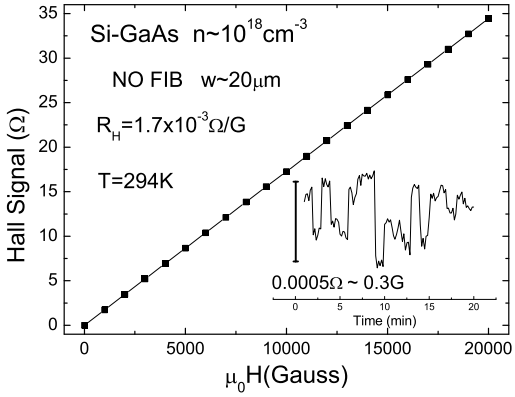

Figure 3.4: Hall response of a Si-doped GaAs micro probe before FIB milling (HM654). The thickness of the doped layer was $d = 500$ nm. The inset shows noise (calculated in terms of magnetic field B) in the measured signal vs time.

tances and the measured noise level, that results in a lower SNR, as it is seen in Figures 3.4 and 3.5, where the same probe is shown before and after FIB patterning. It turns out that the smallest lateral size of a device that preserves optimal working conditions depends on the milling procedure and the initial charge concentration. For this reason I focused my study on highly doped GaAs films, and used low ion current values, to reduce as possible ion implantation and defects. Regarding the different milling procedures, we found that the I_2 assisted approach does not seem to influence the final electrical behavior of the worked probes.

With a starting doping level of $n = 10^{18}$ cm^{-3}, the probes can be milled down to $\sim$ 500 nm lateral size and they successfully operate between 4 and 300 K, showing slight changes in the Hall coefficient and noise level (see table 3.1). Using films with $n = 3.5 \times 10^{18}$ cm^{-3}, probes with lateral size as small as $\sim$ 100 nm and field resolution of about 3 G could be obtained, as shown is Figure 3.6. The resulting flux sensitivity is very high: $< 10^{-2}\Phi_0$. Probably due to charge depletion, the latter probes can work at room temperature but not below 100 K.

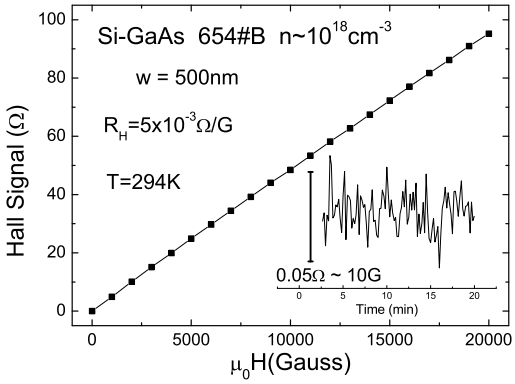

Figure 3.5: Hall response of a Si-doped GaAs nano-probe(HM654#B, see Table 3.1). The thickness of the doped layer was $w \approx 500$ nm and $d = 500$ nm.

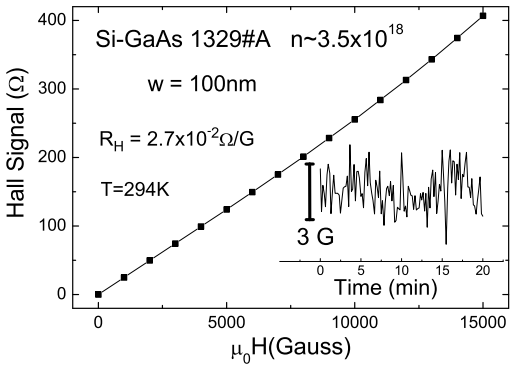

Figure 3.6: Hall response of a Si-doped GaAs nano probe (HM1329#A, see Table 3.1). The width and thickness of the probe were $w \approx$100 nm and $d =$100 nm, respectively. The inset shows noise (calculated in terms of magnetic field B) in the measured signal vs time. The corresponding flux sensitivity (minimum detectable field×active area) is $< 10^{-2}\Phi_0$.

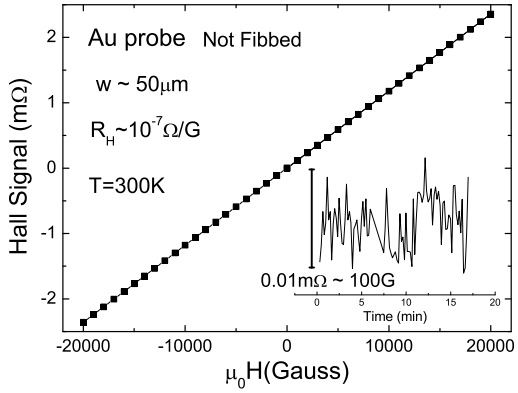

Figure 3.7: Hall response of a gold micro probe before FIB milling (HM654). The thickness of the film was $d = 100$ nm. The inset shows noise (calculated in terms of magnetic field B) in the measured signal vs time.

3.2.2 Au Probes

Au probes show a constant and reliable behavior from room temperature down to liquid helium, as shown in Table 3.1. The Hall coefficient R_H is $\sim 10^{-7}$ Ω/G, as expected for a 100 nm thick gold film ($R_H = 1/ned$, with density of carrier n=10^{23}cm^{-3}, electron charge e=1.6×10^{-19}C and film thickness d). The minimum detectable field is $\sim$ 30 mT at room temperature and it decreases to about 10 mT at 4 K. This field resolution is much worse than for semiconducting probes and it arises from the very small Hall coefficient of gold. To achieve good field sensitivity ($\sim$1 G), very high current would be needed, but this can heat or damage the probe or create relative high stray field. In our case, the maximum value we used was $I_0 < 2$ mA. On the other hand it is important to note that no size-dependent effects were observed for gold probes, as exemplified in Figures 3.7 and 3.8, where the same probe before and after size reduction with FIB is shown. Even a probe with size $\sim$ 100 nm maintains the same Hall coefficient and field sensitivity (Table 3.1).

Recently, I obtained a nano probe with lateral size of $\sim$ 70 nm, using a different geometry for further reducing ion implantation and defects. It can be seen in

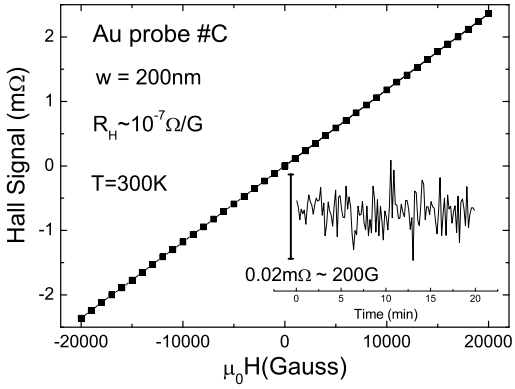

Figure 3.8: Hall response of a gold nano-probe(Au#C, see Table 3.1). Film thickness was $d = 100$ nm. Lateral size $w \approx 200$ nm.

Figure 3.9, whereas Figure 3.10 shows its electrical characterization. Again, the same behavior is nicely maintained. This makes metal films an interesting choice for the fabrication of Hall nano magnetometers because of the possibility to reach very small sizes, of the order of few tens of nm. A smaller active area will of course largely improve the ultimate flux resolution. In our case, a detectable field of 100 G in an area of 70x70 nm^2 implies a flux resolution of $< 10^{-1}\Phi_0$. This sensitivity results from the very small sizes we are able to achieve with our FIB milling technique, and it is at least one order of magnitude better than that reported in reference [17].

Table 3.1: Morphologic and electrical characteristics of the milled probes. n is the density of carriers measured before FIB milling, R_H is the Hall coefficient measured after the milling. Active Area size is the final size at which the probe was reduced by FIB milling. B_{min}=V$_{noise}$/$R_H I_0$, where V$_{noise}$ is the voltage noise measured on the milled devices with the P400 resistance bridge of the QD PPMS and I_0 the maximum used current. Φ_{min}(=B_{min}×Active Area size) is the magnetic flux resolution. The room temperature electron mobility for the semiconducting films was 5679 cm^2/Vs, 2492 cm^2/Vs and 1864 cm^2/Vs for HM523, HM654 and HM1329 respectively. Notice that probe HM1329#B shows an higher noise level than probe HM1329#A, although the size is not as small: this is probably due to a different working procedure at FIB for the former that has probably caused more damages: the measured Hall coefficient after milling is indeed much higher.

			294 K			4 K		
Probe code	n (cm^{-3})	Active area size (nm×nm^2)	R_H (Ω/G)	B_{min} (mT)	Φ_{min} (Φ_0)	R_H (Ω/G)	B_{min} (mT)	Φ_{min} (Φ_0)
Gold Probes								
Au#A	(1×10^{23})	1000×1000	10^{-7}	30	15	10^{-7}	10	5
Au#B	(1×10^{23})	500×500	10^{-7}	30	3.75	10^{-7}	10	1.25
Au#C	(1×10^{23})	150×150	10^{-7}	30	0.3	10^{-7}	10	0.1
Au#D	(1×10^{23})	100×100	10^{-7}	30	0.15	10^{-7}	10	0.05
Au#E	(1×10^{23})	70×70	10^{-7}	30	0.07	10^{-7}	10	0.02
Semiconducting Probes								
HM523	6×10^{16}	1000×1000	0.021	1	0.5	—	—	—
HM654#A	1×10^{18}	1000×1000	0.0038	0.5	0.25	0.0038	0.3	0.15
HM654#B	1×10^{18}	500×500	0.0048	1	0.12	0.0063	3	0.4
HM1329#A	3.5×10^{18}	100×100	0.027	0.3	0.0015	—	—	—
HM1329#B	3.5×10^{18}	200×200	0.16	3	0.06	—	—	—

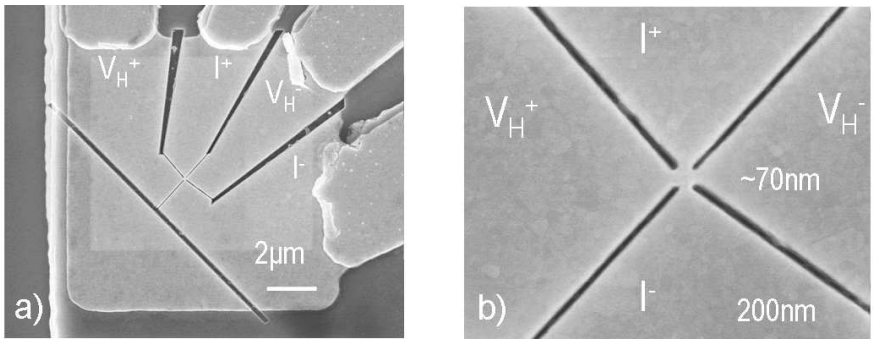

Figure 3.9: SEM image of the 70 nm FIB milled Au probe. Also electrical connection is explained. In (b) a zoom of the active area is seen.

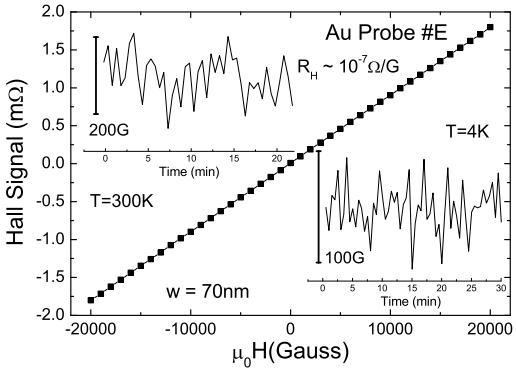

Figure 3.10: Hall response of Au#E nano probe (Active Area$\approx 70 \times 70$ nm^2, see Table 3.1). The film thickness is d =100 nm. The inset shows noise (calculated in terms of magnetic field B) in the measured signal vs time. The resulting flux sensitivity is $< 10^{-1}\Phi_0$.

3.3 Discussions

As already mentioned, the best SNR for an Hall sensor can be estimated as

$$\frac{S}{N} = \frac{I_0 R_H B}{\sqrt{4k_B T R_S}} \tag{3.1}$$

where $\sqrt{4k_B T R_S}$ is the Johnson noise. In the case of GaAs probes, given a measured series resistance of 60 KΩ, the Johnson noise expected at room temperature is around 30 nV, whereas it is about 1 nV for gold. However, I always found additional sources of noise that overcome these theoretical expectations. In the following, I will briefly discuss them.

In the case of gold films, with a Hall coefficient $R_H = 10^{-7}$ Ω/G and a maximum current $I_0 = 2$ mA, the detected noise was essentially determined by our electronic set-up. Since the noise due to amplifiers is already few tens of nV, better resolutions can be simply obtained employing low noise pre-amplifiers. A further improvement can be obtained by changing the growth conditions/substrate of Au films that may lead to an increase of the grain size to above 100 nm. This will decrease the channel resistance allowing, at least, the use of higher current or smaller thickness.

The case of doped GaAs probes is more complex. The measured values of the intensity of the noise were 10 to ∼100 times higher than the estimated Johnson value. The observed noise was not present before the milling procedure, it strongly depended on the ultimate size of the milled device (see the 10^{18}-doped film in table 3.1) and it increased with increasing current. Moreover, we observed that it was higher in probes for which the damage induced by FIB was more important (i.e. probes for which the difference between the density of carriers n before and after milling is higher). These features suggest that the source of this noise is related to fluctuations of the total impedance of the device. These are likely originated by the presence of the depletion region and of the defects produced during milling that may affect both concentration [17] and mobility of carriers and, eventually, the channel resistance. In this way, the current through the channel is no longer stable, thus leading to fluctuations of the transverse voltages.

A similar argument can be applied to the measured signal offsets. These are of particular importance for nano sensors and should be minimized for any technological application. Concerning the gold probes, the offset magnitudes were closely related to the symmetry of the patterned active area, as expected. For the smallest sensors (∼100 nm lateral sizes) the best values were close to $\sim 8\times10^{-3}\ \Omega$, which corresponds to a misalignment of $\sim$ 5 nm. This value is consistent with the resolution in positioning the ion beam. Conversely, for the semiconducting probes we found offset values higher than expected from simple misalignment of the probe arms, especially for probes showing higher noise. This suggests that the presence of defects plays the major role in determining also the offsets, causing non uniform distribution of equipotential lines. For the probe showing the best SNR (HM1329#A, see table 3.1) the measured offset was $\sim 10^2\Omega$, while for probe HM1329#B (table 3.1) it was as high as $\sim 10^3\Omega$.

3.4 Conclusions

I fabricated nano Hall devices by FIB milling of metal and semiconducting films. The best magnetic field sensitivity was achieved with semiconducting (Si-doped GaAs) probes and sensors as small as 100 nm in lateral size were fabricated, with ∼1 G resolution. FIB induced damage is probably the main limitation to their performances (SNR) and this problem needs to be overcome for size reduction below 100nm. Employing different materials (such as room temperature high mobility InSb) can further improve both field sensitivity and ultimate lateral size.

Metal probes (Au) were found to be essentially insensitive to FIB patterning and no particular shrinking effects were observed, so size reduction to tens of nm seems feasible. In addition, they operate properly from room temperature down to 4 K. Metallic Hall magnetometers could be used for applications for which the spatial resolution is of particular importance.

Chapter 4

High Spin Molecular Cluster

In this chapter, I will present part of the results we obtained working on two families of ferric molecular clusters, namely Fe_{14} and Fe_{17}. This project started in 2004, in collaboration with the chemist groups of Manchester and Edinburgh, with the purpose to synthesize and characterize magnetic clusters with large spin S and small anisotropy values. Systems with such properties are indeed very appealing candidate for the magnetocaloric effect at low temperatures, as it was found for the Cr_7Cd molecular ring [75]. These clusters, showing a very high Spin S ground state and hence a huge magnetic signal, revealed to be also an ideal research field to exploit our Hall probe magnetometry technique. Employing micro probes to measure small crystals of ≈ 100 μm in size, I successfully obtained magnetization, susceptibility and relaxation measurements in the ^{3}He-temperature region. These low T magnetic data allow us to enlighten new interesting physical phenomena, such as the huge magnetocaloric effect of the Fe_{14} molecule, and the competition between dipolar ordering and single molecule behavior in the Fe_{17} cluster. I will discuss the first in Section 4.1 and the latter in Section 4.2.

4.1 Spin-enhanced magnetocaloric effect in Fe_{14} molecular nanomagnet

4.1.1 Introduction

The magnetocaloric effect (MCE) is intrinsic to any magnetic material and is based on the change of the magnetic entropy upon application of a magnetic field. Besides the fundamental interest on related thermodynamical properties of novel materials, MCE is of great technological importance since it can be used for cooling applications [76–78] according to a process known as adiabatic demagnetization [79, 80]. To this purpose, most attention was devoted to date to lanthanide compounds and alloys that posses relatively large magnetic entropy variations [76–78]. Concerning the low temperature-range, also nanomagnets are considered good candidates for enhanced magnetocaloric effect (MCE) and therefore are of interest for applications as magnetic refrigerants [81, 82]. This is mostly because large magnetic moments S, resulting in large magnetic entropies, are attainable in this class of materials. Large S, however, is often associated with large particle magnetic anisotropy. The larger is the particle magnetic anisotropy, the higher is the blocking temperature and the lower is the isothermal magnetic entropy change [83]. Ideal materials would rather be nanomagnets with large S and small anisotropy [75]. Opportunities are provided by molecule-based clusters, which are collections of identical nanomagnets. Recently, quantum effects were taken into account to explain the MCE of high-spin molecular clusters, such as Mn_{12} and Fe_8 [84], whereas chemical engineering was proposed to enhance MCE in Cr-based molecular rings [75].

We found that the Fe_{14} molecular nanomagnet [85] has a huge MCE in the liquid helium T region, which, to our knowledge, is much larger than that of any other known material. This comes out from a combination of several features, such as the spin ground-state that amounting to $S = 25$ is amongst the highest ever reported, and the highly symmetric cluster core that results in small cluster magnetic anisotropy. The latter enables the occurrence of long-range magnetic

order (LRMO) below $T_N = 1.87$ K, probably of antiferromagnetic nature. Also low-lying excited S states additionally enhance the MCE of Fe_{14}.

This Section is organized as follows. Firstly, I will introduce the magnetocaloric effect and describe the magnetic structure of the Fe_{14} cluster core. Then, I will present and discuss the magnetization and specific heat experiments, whose results are used in the last part to calculate the MCE parameters.

4.1.2 Magnetocaloric Effect

When a material is magnetized by application of a magnetic field H, the entropy associated with the magnetic degree of freedom, S_{m}, is changed as the field changes the magnetic order of the material. The MCE and the associated principle of adiabatic demagnetization is readily understood looking at Figure 4.1. The system, assumed to be a paramagnetic material, is initially in state A, at temperature T_i and field H_i. When the magnetic field is isothermally changed to H_f, the system goes to state B with an entropy change of ΔS_m. Thus, a slow decrease of the field from H_f to H_i causes the system to adiabatically cool down by $\Delta T_{ad} = T_i - T_f$ to state C. Both ΔS_m and ΔT_{ad} represent the characteristic parameters of the MCE. It is easy to see that if the magnetic change ΔH reduces the entropy ($\Delta S_m < 0$), then ΔT_{ad} is positive, whereas if ΔH is such that $\Delta S_m > 0$, then $\Delta T_{ad} < 0$ (Figure 4.1).

Large magnetic moments are often attainable in superparamagnetic clusters, resulting therefore in large entropies. Moreover, for certain ranges of field, temperature and cluster size, it is easier in superparamagnets than in pure materials to change the magnetic entropies by application of a field [81]. Obviously, this leads to an interest in superparamagnets in terms of MCE. The picture depicted in Figure 4.1 is still valid for a superparamagnet with S as net cluster moment, provided that it is at temperatures above the blocking temperature. The cluster magnetic anisotropy, which indeed determines the blocking temperature, can be considered as a drawback in the MCE efficiency of superparamagnets. This because, by shifting the maxima of $\Delta S_m(T)$ and $\Delta T_{ad}(T)$ towards higher temper-

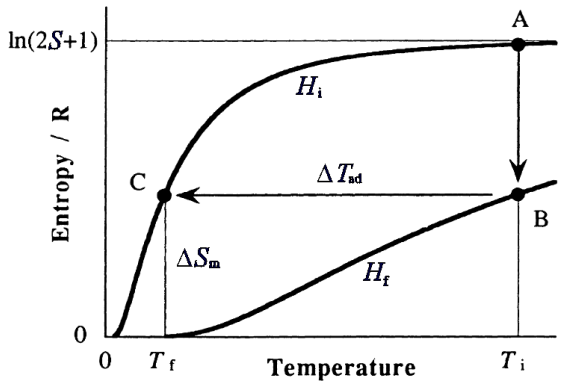

Figure 4.1: Molar entropy of a (super)paramagnet with spin S per formula unit, as a function of temperature, for magnetic field H_i and $H_f > H_i$. AB process: isothermal magnetization. BC process: adiabatic demagnetization.

atures, it tends to lower the values of the MCE response [81–83]. Ideal candidates for MCE applications, would then be magnetic clusters with large S and small anisotropy.

4.1.3 Fe_{14} molecular nanocluster

In the following, I will briefly focus on the Fe_{14} compound, nominally $Fe_{14}(bta)_6O_6(OMe)_{18}Cl_6$ [85]. Figure 4.2 shows the highly symmetric core, comprising fourteen Fe^{3+} $s = \frac{5}{2}$ spins, which can be described as a hexacapped hexagonal bipyramid with the caps on alternate faces. The three face capping iron ions (Fe2, Fe3, Fe4 and symmetry equivalents) and the apical iron (Fe1 and symmetry equivalent) on either half of the molecule form two $[Fe_4(bta)_3Cl_3]$ units each separated from a central $\{Fe_6\}$ ring, which has an almost planar symmetry. The Fe−O−Fe bridges fall into two categories: those that connect the apical iron ions (Fe1 and symmetry equivalent) to the face cap and equatorial iron ions, and those characterized by much smaller angles that connect all other iron ions. If we assume that the larger angles will lead to the strongest antiferromagnetic exchange, thus dominating the other interactions, then we are left with a situation whereby the spins on Fe1 and symmetry equivalent are antiferromagnetically

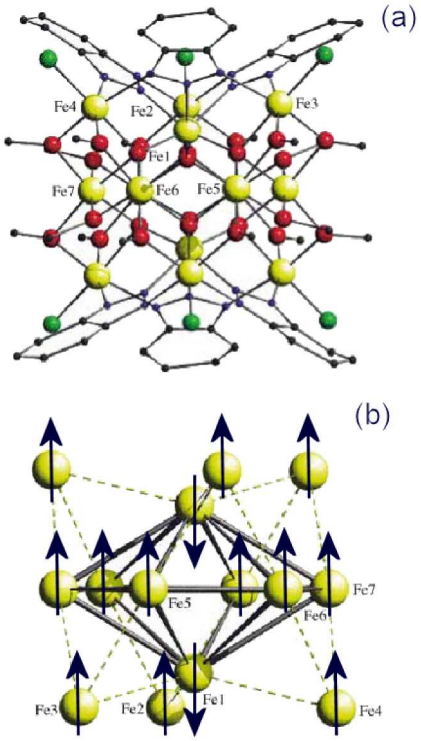

Figure 4.2: (a) Molecular structure of $Fe_{14}(bta)_6O_6(OMe)_{18}Cl_6$. Colour scheme: Fe, yellow; O, red; N, blue; Cl, green. After Ref. [85]. (b) Sketch of the symmetric core containing fourteen exchange-coupled Fe^{3+} ions, yielding a total spin $S = 25$. The arrows illustrate the alignment of the Fe^{3+} $s = \frac{5}{2}$ spins inside the cluster.

coupled to all other spins, which should lead to twelve $s = \frac{5}{2}$ spins up and two $s = \frac{5}{2}$ spins down, and an overall $S = 25$ cluster spin ground-state (Figure 4.2). Also preliminary characterizations [85] and simulations [86] agree that the Fe_{14} molecule has a spin ground-state as large as $S = 25$ and small cluster magnetic anisotropy.

4.1.4 Experimental results

Magnetization measurements down to 2 K and specific heat measurements using the relaxation method down to ≈ 0.35 K on powder samples, were carried out in

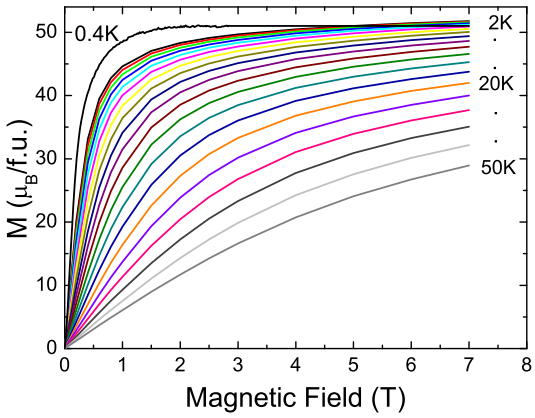

Figure 4.3: Isothermal $M(H)$ curves measured at different temperatures from 2 K to 50 K. Also the curve taken at 0.4 K is shown.

our Quantum Design PPMS set-up for the $0 < H < 7$ T magnetic field range. Magnetization and susceptibility measurements below 2 K were performed using the Hall microprobe magnetometer installed in the same set-up. In this case the sample used consisted in a single grain of c.a. 10^{-3} mm^3. Data taken by Hall magnetometry are initially in arbitrary units, and successively are properly scaled with the high-T measurement from the commercial magnetometer. Figure 4.3 shows isothermal magnetization measurements at low-T. It corroborates the high-spin $S = 25$ ground state of the Fe_{14} nanocluster. For instance, a fit of $M(H)$ data collected at $T = 2$ K provides $S = 25$, $g = 2.06$ and uniaxial zero-field splitting as low as $D = 0.04$ K. Figure 4.4 shows the magnetic susceptibility $\chi(T)$ and specific heat $C(T)$ data of Fe_{14}. The main feature is given by the sharp anomaly at $T_N = (1.87 \pm 0.02)$ K, that can be seen in both $\chi(T)$ and $C(T)$, and that we attribute to LRMO. The maximum χ at T_N corresponds to ~ 56 emu/mol (Figure 4.4, upper panel), which is smaller than that expected for paramagnetic $S = 25$ spin. This suggests that a full ordered $S = 25$ state inside the cluster is not achieved at T_N, likely because (i) internal degrees of freedom allow spin states other than $S = 25$ to contribute, and/or (ii) intercluster interactions are similar in magnitude to the intracluster ones. The observed behavior is compatible with an

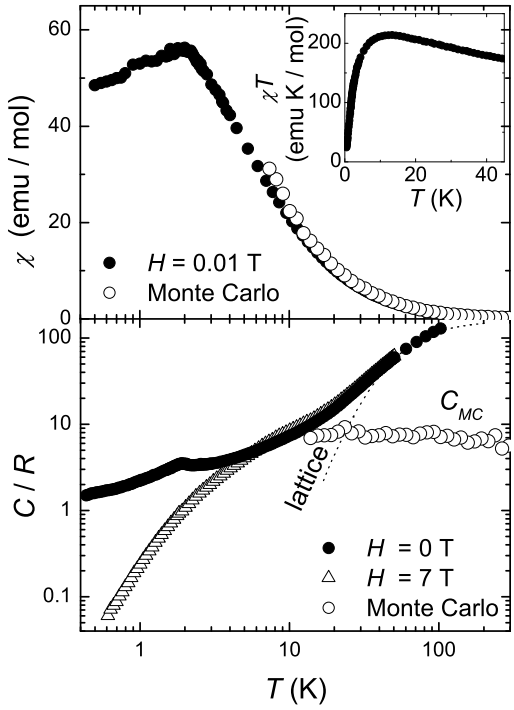

Figure 4.4: Top: dc-$\chi(T)$ (and dc-$\chi T(T)$ in the inset) taken for $H = 0.01$ T. Bottom: $C(T)$ for $H = 0$ and 7 T. Empty dots are MC simulations for $H = 0$ (see text). Dotted line is the lattice contribution.

antiferromagnetic nature of the ordered phase, as suggested by the sharp decrease of $\chi T(T)$ at low T (inset of Figure 4.4).

The specific heat data C/R, shown in the lower panel of Figure 4.4 for $H = 0$ and 7 T, corroborate the interpretation of the χ data: the λ-type anomaly in the zero-field C at T_N, revealing the onset of LRMO, is quickly removed by the application of an external H, proving its magnetic origin. The occurrence of LRMO implies relatively small cluster magnetic anisotropy, otherwise superparamagnetic blocking above T_N should be observed. However, even a small anisotropy may become important for a S as large as that of Fe_{14}. This is reflected, for instance, in the relative height of the transition peak at T_N that, amounting to $\approx 1.2\ R$, is apparently a bit too small for such a large S, suggesting that a large portion of

the magnetic entropy is not available for the ordering mechanism. The C data measured above 20 K show a large increase, that we associate with the lattice contribution [1].

4.1.5 Evaluation of MCE

I will now evaluate the magnetocaloric effect for the Fe_{14} molecular compound from experimental data, as described in Reference [87]. This procedure includes the evaluation of the isothermal magnetic entropy change ΔS_m and adiabatic temperature change ΔT_{ad} from measured specific heat. For comparison, ΔS_m also from magnetization data has been evaluated.

MCE from specific heat.

From the specific heat data of Figure 4.4(lower panel) the total entropies at applied magnetic fields $H = 0$ and 7 T as functions of temperature can be determined using the following equation:

$$S(T)_H = \int_0^T \frac{C(T)_H}{T}\, \mathrm{d}T. \tag{4.1}$$

The result of the numerical integration $S(T)_H$ is plotted in the bottom inset of Figure 4.5 for both applied fields. The magnetic entropy change and adiabatic temperature change is than calculated for this field change $\Delta H = (7 - 0)$ T, as $\Delta S_m(T)_{\Delta H} = [S(T)_{7\mathrm{T}} - S(T)_0]_T$ and $\Delta T_{ad}(T)_{\Delta H} = [T(S)_{7\mathrm{T}} - T(S)_0]_S$, respectively. [2] The results are displayed as filled dots in Figure 4.5. It can be seen that, for $\Delta H = (7 - 0)$ T, Fe_{14} reaches a maximum $-\Delta S_m$ of $\approx 4.5\ R$ (or equivalently ≈ 15.9 J/Kg K) and ΔT_{ad} of ≈ 5 K, both at $T \simeq 6$ K. It is worth to mention that the entropy is calculated starting from the lowest experimentally achieved temperature (≈ 0.35 K) and, obviously, not from $T = 0$ K as requested by 4.1.

[1] Lattice contribution above 20 K is modelled with $n = 55$ optic-like modes having Einstein temperature $\theta_E = 68$ K (dotted curve in Figure 4.4)

[2] The estimation of the lattice contribution is irrelevant for our calculation, since we consider the difference between the total entropies at different fields.

Therefore, the so-obtained $\Delta S_m(T)$ and $\Delta T_{ad}(T)$ should be considered as underestimates. Upper limits are roughly obtained by extrapolating linearly the experimental specific heat below T_N for $T \to 0$ K. The results, plotted in Figure 4.5 as error bars, show that we estimate at $T = 6$ K for $\Delta H = (7 - 0)$ T the magnetic entropy change and adiabatic temperature change as $-\Delta S_m = (5.0 \pm 0.8)\ R$, or equivalently (17.6 ± 2.8) J/Kg K, and $\Delta T_{ad} = (5.8 \pm 0.8)$ K, respectively.

MCE from magnetization.

In an isothermal process of magnetization, the total magnetic entropy change ΔS_m due to the application of a magnetic field, can be derived from Maxwell relations by integrating over the magnetic field change $\Delta H = H_f - H_i$, i.e.,

$$\Delta S_m(T)_{\Delta H} = \int_{H_i}^{H_f} \left(\frac{\partial M(T,H)}{\partial T} \right)_H \mathrm{d}H. \tag{4.2}$$

From the magnetization data of Figure 4.3, $\Delta S_m(T)$ has been calculated using Eq. 4.2. The so-obtained magnetic entropy change for the magnetic field change $\Delta H = (7 - 0)$ T [3] is displayed as function of temperature in the top panel of Figure 4.5, together with ΔS_m as obtained from specific heat data for comparison. It can be noticed that, within the error, the result fully agrees with the previous estimate inferred from specific heat, suggesting that both (independent) procedures can be effectively used to characterize the Fe_{14} molecular nanocluster with respect to its magnetocaloric properties.

The high spin value of Fe_{14} accounts only partially for the large MCE we measured. The experimental $\Delta S_m(T)$ exceeds, indeed, the entropy expected for a $S = 25$ spin system, that is $R \ln (2S + 1) \simeq 3.9\ R$ (Figure 4.5). To explain where the observed excess of magnetic entropy change comes from, the magnetic and thermal properties of an isolated Fe_{14} molecule in zero-applied-field has been modelled by classical Monte Carlo (MC) simulations using the metropolis algorithm. As already mentioned and looking at the bottom inset of Figure 4.4,

[3] For practical reasons, the measurements at the lowest applied field were carried out for $H_i = 10^{-3}$ T, which in our calculations was approximated to zero-applied-field.

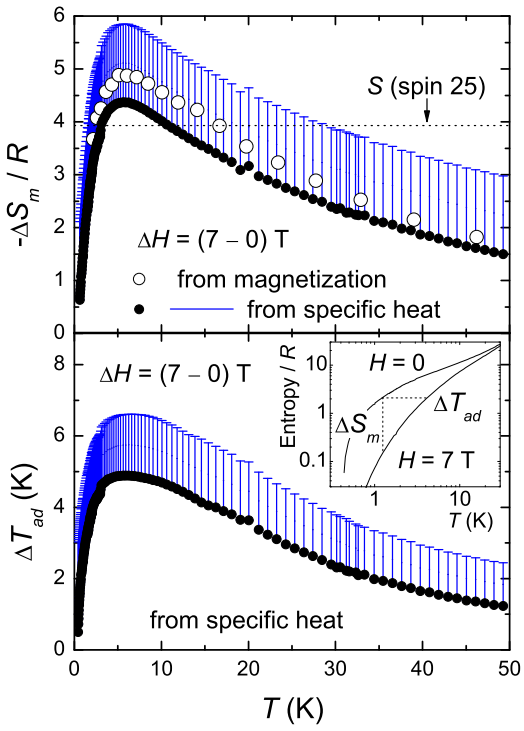

Figure 4.5: Top panel: Temperature dependence of the isothermal magnetic entropy change ΔS_m as obtained from specific heat (filled dots and error bars, see text) and magnetization data (empty dots), both for $\Delta H = (7-0)$ T. Shown as dotted line is the limiting entropy of a $S = 25$ spin system. Lower panel: Temperature dependence of the adiabatic temperature change ΔT_{ad} as obtained from specific heat data (filled dots and error bars, see text) for $\Delta H = (7-0)$ T. In the inset: Experimental entropy of Fe_{14} vs temperature for $H = 0$ and 7 T.

two primary categories of the Fe−O−Fe bridges have been identified [85]: those that connect the apical iron ions to the face cap and equatorial iron ions (whose exchange coupling we indicate as J_1), and those characterized by much smaller angles that connect all other iron ions (J_2). We consider therefore the Hamiltonian $\mathcal{H} = -\sum_{i=1,2}\sum_{(j,k)} J_i\, \mathbf{s_j}\cdot\mathbf{s_k}$, for all possible (j,k) pairs of exchange-coupled Fe^{3+} spins. Thus, we calculate $\chi(T)$ to fit the experimental data (Figure 4.4), obtaining estimates for J_1 and J_2. To avoid the influence of inter-cluster interactions, only data for $T > 20$ K are taken into account. Assuming $g = 2.06$ as deduced

from the saturation of the magnetization, the fit provides $J_1/k_B \simeq -60.0$ K and $J_2/k_B \simeq -25.2$ K, where negative sign indicates that they are both antiferromagnetic. A similar analysis of $\chi(T)$ for Fe_{14} is already reported in Ref. [86]. The so-obtained J_i values are next used to calculate the specific heat C_{MC} associated with internal degrees of freedom of the molecule. A relatively large contribution is obtained $C_{MC} \sim 7 \div 9\ R$ for 20 K $< T <$ 300 K (Figure 4.4), that implies the presence of excited states close in energy to the $S = 25$ ground-state. Likely, large C_{MC} values have to be expected in the lower-T region as far as excited states remain populated. Recalling the uncomplete achievement of the $S = 25$ spin state deduced from experimental $\chi(T)$ at T_N, and on basis of these MC simulations, we identify the entropy associated with this contribution as that responsible for the observed enhancement of the MCE of Fe_{14}. Additionally, the transition to LRMO is certainly contributing as well to the MCE parameters below $\sim$ 2 K. However, on basis of the relatively small height of the ordering peak (Figure 4.4), this contribution is not expected to be the dominant one. Indeed, no apparent anomaly is seen in the $\Delta S_m(T)$ and $\Delta T_{ad}(T)$ curves at T_N.

4.1.6 Concluding remarks

The values of $\Delta S_m(T)$ and $\Delta T_{ad}(T)$ obtained in Fe_{14} are exceptionally large, even more than the ones obtained with intermetallic materials known to be, so far, the best magnetic refrigerant materials in the temperature range below 10 K [77, 88]. For instance, the best representative is the recently studied [88] $(Er_{1-x}Dy_x)Al_2$ alloy that, for $x \geq 0.5$ concentrations, presents MCE parameters below 10 K which are at least 30 % smaller than that of Fe_{14}. Among systems of superparamagnetic particles and molecular magnets, the gap is even more pronounced. For instance, because of their well-defined spin ground state in this temperature and field range, it is easy to show that the well known Fe_8 and Mn_{12}-ac molecular nanoclusters cannot exceed values of $-\Delta S_m \simeq 12.5$ and 11 J/Kg K, respectively, thus much smaller than that of Fe_{14}. Moreover in these materials, as in most molecular magnets, an additional complication (with respect to MCE

parameters) is added by the cluster magnetic anisotropy. Because of this, cluster spins are usually blocked in the liquid helium temperature range, causing the spin-lattice relaxation to slow down dramatically. Therefore, cluster spins tend to loose thermal contact with the lattice [89,90] resulting in lower magnetic entropies and, consequently, lower MCE parameters. Ideally, it is desirable to keep the spin-lattice relaxation at sufficiently high rates down to lowest temperatures, in order to have a more efficient material in terms of MCE. For this reasons, materials with small cluster anisotropy are preferable [75].

Summing up, Fe_{14} molecular nanomagnet is unique in terms of MCE due to the combination of the following characteristics: (i) unusually large spin ground-state; (ii) small cluster magnetic anisotropy; (iii) excess of entropy resulting from low-lying excited S states; (iv) long-range magnetic ordering. For these reasons, Fe_{14} has therefore high potentiality to work as magnetic refrigerant within a temperature range below 10 K.

4.2 Tunable Dipolar Magnetism in Fe_{17} Molecular Cluster

4.2.1 Introduction

A rejuvenated interest in phase transitions driven only by dipolar interactions has emerged since the experimental discovery that the magnetic molecular materials Cr_4 [91] and Mn_6 [92, 93] provide attractive examples of pure dipolar magnets. These are nanostructured such that molecular clusters replace what atoms are to conventional materials. Quantum-mechanical superexchange interactions within each molecule result in net (high-)spin values per molecule at low temperatures. In parallel, dipolar interactions provide the only source of coupling between the molecular spins arranged in crystallographic lattices. Assuming each molecule as a high-spin point-like dipole, the macroscopic properties of dipolar magnets can be precisely predicted because dipole-dipole interactions are calculated without involving any adjustable parameter [93–97]. These ideal materials are however very difficult to obtain. As often is the case, intermolecular superexchange interactions may not be negligible at very low temperatures where long-range magnetic order (LRMO) takes place. The consequence is that correlations between the molecules are often established by quantum-mechanical superexchange interactions at short ranges, whose macroscopic prediction is made difficult by their strong dependence on electronic details. Indeed, intermolecular superexchange interactions were found to be responsible for the observed LRMO in the high-spin molecular clusters Fe_{19} [98], Mn_4Br [99], Mn_4Me [90], and Fe_{14} [100], while they likely play a mayor role also in Mn_{12} [101].

The absence of any superexchange pathway between the molecules is not the only prerequisite needed for the experimental observation of dipolar order. An obvious requirement is that molecules should have large molecular spins to lead to accessible ordering temperatures. Another complication is added by the cluster magnetic anisotropy. Crystal-field effects give rise to anisotropy energy barriers for each molecule that result in slow magnetic relaxation below a certain blocking

temperature. The cluster anisotropy energies favor the molecular spin alignment along dictated directions, thus competing with the intermolecular coupling. The anisotropy therefore has to be very small, such that the spin-lattice relaxation is kept sufficiently fast down to temperatures low enough for LRMO to be observed [90, 92].

We have studied the Fe_{17} molecular nanomagnet [102] that, carrying very-large spin $S = 35/2$ and axial anisotropy as small as $D \simeq -0.02$ K, represents an excellent candidate for these studies. In addition, these molecules are only bound together in the crystal by van der Waals forces thus prohibiting any intermolecular superexchange pathway. What makes Fe_{17} a *unique* model system is that it is possible, by changing the crystallization conditions, to change the molecular packing *without* affecting the individual molecules, that is keeping the surrounding ligands, the molecular high-spin ground-state and magnetic anisotropy unaltered. In other words, it is possible to tune the dipolar coupling between molecules with respect to the single-molecule properties. The resulting interplay gives rise to macroscopic behaviors ranging from superparamagnetic blocking to LRMO.

4.2.2 Fe_{17} molecular cluster

The Fe_{17} molecules are synthesized by the group of Dr. E. Brechin in Edinburgh. They contain 17 Fe^{3+} atoms linked via oxygen atoms (Figure 4.6) and are obtained by dissolving either $FeBr_3$ or $FeCl_3$ in a coordinating base, e.g. pyridine (pyr), beta-picoline (b-pic) or iso-quinoline (iso-qui) that also acts as solvent. To crystallize the product (Fe_{17}), a second (often non-coordinating) co-solvent like diethyl-ether (Et_2O), acetone (Me_2CO), acetonitrile (MeCN), iso-propylalcohol (IPA), *etc.* is slowly diffused into the basic solution. The product is generally soluble in the first solvent (e.g. pyr) but insoluble in the second (e.g. Et_2O) and by slowly diffusing the second solvent in, the product is crystallezed. In this way several derivatives having the same Fe_{17} magnetic core are obtained [4]. Whilst

[4]For instance, the reaction between $FeCl_3$ and pyr in the presence of MeOH produces the complex $Hpyr[Fe_{17}O_{16}(OH)_{12}(pyr)_{12}Cl_4]Cl_4$ whose structure and preliminary magnetic prop-

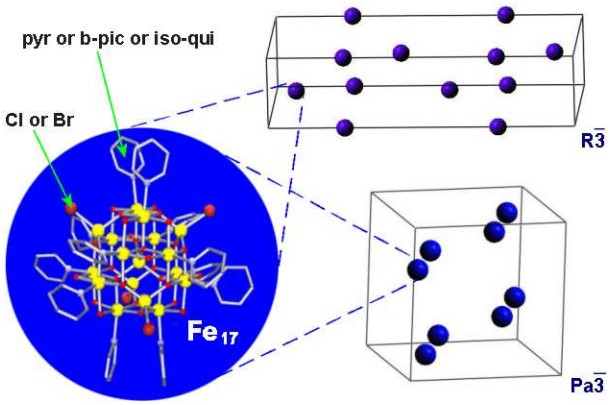

Figure 4.6: The Fe_{17} molecule containing 17 magnetically coupled Fe^{3+} atoms (Fe = yellow balls; Cl or Br = red balls ; O = small red balls), together with the packing in two different unit cells: $R\bar{3}$ (trigonal) and $Pa\bar{3}$ (cubic).

the spin value is preserved throughout the whole Fe_{17} family, the anisotropy may change significantly. Chemists have synthesized a number of new Fe_{17} clusters containing bromide ions in which they can either (i) exchange the pyr ligands for b-pic or iso-qui ligands 4.6 thus modifying only the outer organic coating of the Fe_{17}, such that the major change is purely intramolecular (*anisotropy*); or (ii) change the crystallizing co-solvent such that only the packing (*space group*) of the molecules in the crystal is changed. For example, the reaction between $FeBr_3$ and pyr in the presence of Me_2CO affords the Fe_{17} magnetic core crystallized in the trigonal space group $R\bar{3}$, whilst the same reaction but in the presence of IPA gives an identical Fe_{17} magnetic core but crystallized in the cubic space group $Pa\bar{3}$ (Fig. 1). By defining the organic ligand and subsequent crystallizing conditions, they can therefore reproducibly generate different arrays of this molecular magnet.

We intensively studied the above-mentioned Br derivatives of the Fe_{17} molecule having trigonal or cubic symmetries. [5]

erties were recently reported in [102], where it is showed that it has $S = 35/2$ and small cluster anisotropy.

[5]The compound Fe_{17}-trigonal crystallizes in space group $R\bar{3}$ with $a = b = 16.2552(6)$ Å, $c =$

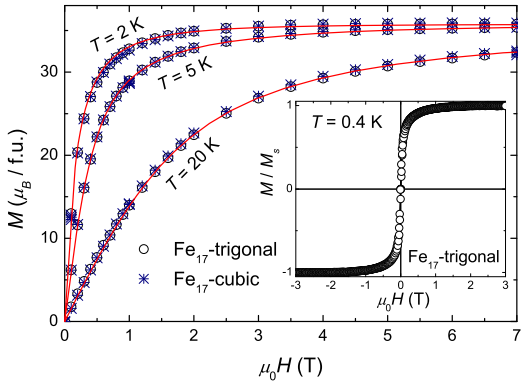

Figure 4.7: Isothermal molecular magnetization for both Fe_{17}-trigonal ($\circ$) and Fe_{17}-cubic ($*$) collected at $T = 2, 5$ and 20 K. Solid lines are the results of the fit (see text), yielding net molecular spin $S = 35/2$ and axial $D = -0.023$ K. Inset: Hysteresis loop of Fe_{17}-trigonal at $T = 0.4$ K.

4.2.3 Experimental Results

We performed measurements of magnetization down to 2 K and specific heat down to ≈ 0.3 K on powder samples, using our PPM-system in the $0 < H < 7$ T magnetic field range. Magnetization, susceptibility and relaxation measurements below 2 K were performed using Hall microprobes. Raw data were scaled with measurements taken with the commercial apparatus. The samples used were single grains of c.a. 10^{-3} mm^3. For measurements performed on powder samples, the calculated fits were obtained taking into account spin random orientations.

71.919(5) Å, whereas Fe_{17}-cubic crystallizes in space group $Pa\bar{3}$ with $a = b = c = 29.2854(3)$ Å. From the unit cell volumes, the mean values of the intermolecular separations (assumed as the centroid to centroid distances) has been obtained: 13.9 Å for Fe_{17}-trigonal, and the slightly larger value of 14.6 Å for Fe_{17}-cubic. CCDC-612322 and CCDC-612323 contain the supplementary crystallographic data for Fe_{17}-cubic and Fe_{17}-trigonal, respectively. These data can be obtained free of charge via www.ccdc.cam.ac.uk/conts/retrieving.html (or from the Cambridge Crystallographic Data Centre, 12 Union Road, Cambridge CB21EZ, UK; fax: (+44)1223-336-033; or deposit@ccdc.cam.ac.uk).

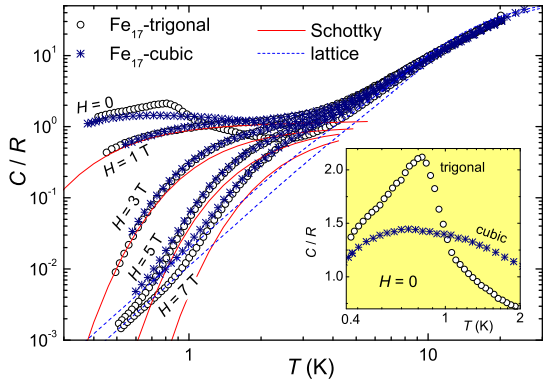

Figure 4.8: Specific heat of Fe_{17}-trigonal and Fe_{17}-cubic for several applied-fields, as labelled. Drawn curves are explained in the text. Inset: Magnification of the low-T / zero-field range showing the different ordering behaviors.

Field-dependencies of the molar magnetization $M(H)$ for both Fe_{17}-trigonal and Fe_{17}-cubic were collected for $T = 2, 5$ and 20 K (Figure 4.7). The important result is that the $M(H)$ curves depend on the applied-field in an *identical* manner regardless of the trigonal or cubic symmetry. This implies that the Fe_{17} magnetic molecule (that is the spin ground-state and anisotropy) is the same in both complexes. If we consider the single-spin Hamiltonian $\mathcal{H} = DS_z^2 + g\mu_B \overrightarrow{H} \cdot \overrightarrow{S}$, the magnetization in the whole field-range can be well fitted with net molecular spin $S = 35/2$, zero-field splitting $D = -0.023$ K and $g = 2.06$ for both complexes. Although smaller trigonal components could be present, the data do not justify a more sophisticated fitting.

Figure 4.8 shows the collected specific heat $C(T, H)$ data of both Fe_{17} molecular compounds as function of temperature for several applied-fields. At first sight and as for the $M(H)$ data (Figure 4.7), the $C(T, H)$ of Fe_{17}-trigonal does not differ from that of Fe_{17}-cubic, at least for $H > 0$. The main difference is in the zero-applied field data for which a λ-type anomaly centered at $T_C = 0.81$ K is observed for trigonal symmetry (inset of Figure 4.8). Anticipating the discussion below, this feature reveals the onset of LRMO, the magnetic nature is indeed

proven by its disappearance upon application of H. Clearly, the λ-type anomaly arises on top of a much broader one, which shifts with increasing applied-field towards higher temperatures. Because of the small anisotropy ($D \simeq -0.02$ K), it is expected that the magnetic contribution to $C(T, H)$ for $H \geq 1$ T is due to Schottky-like Zeeman splitting of the otherwise nearly degenerate energy spin states. Indeed, the calculated Schottky curves (solid lines in Figure 4.8) arising from the field-split levels accounts very well for the experimental data. The same behavior is followed by Fe_{17}-cubic except that no sign of LRMO is apparently observed.

As particularly evident in the low-T / high-H region of Figure 4.8, phonon modes of the crystal lattice contribute differently to $C(T)$ of Fe_{17}-trigonal and Fe_{17}-cubic. We estimated the lattice contributions (dashed lines in Figure 4.8) by fitting to a model given by the sum of a Debye term for the acoustic low-energy phonon modes plus an Einstein term that likely arises from intramolecular vibration modes. From the field-dependencies of $M(T, H)$ and $C(T, H)$, we have already deduced that the individual Fe_{17} molecule remains identical regardless of space group. Therefore, it is not surprising that the fit provides the same Einstein temperature $\theta_E \simeq 42$ K for both compounds (Figure 4.8). Contrary, low-energy phonon modes result in different Debye temperatures whose values are $\theta_D \simeq 23$ K and 28 K for Fe_{17}-cubic and Fe_{17}-trigonal, respectively. Because Fe_{17}-cubic has larger intermolecular distances [6], softer low-energy modes, yielding smaller θ_D, are indeed to be expected. The so-obtained lattice contributions allow us to estimate the entropy changes ΔS by using the relation $\Delta S/R = \int_0^\infty C_m(T)/(RT)\mathrm{d}T$ where $C_m(T)$ is the magnetic contribution obtained from $C(T)$ after subtraction of the respective lattice contribution. For both compounds, the obtained ΔS amounts to 3.7 R, which is in good agreement with the entropy expected $R\ln(2S+1) \simeq 3.6\ R$, given $S = 35/2$. As already anticipated, $T_C = 0.81$ K can therefore be safely attributed to the LRMO temperature of the molecular spins in Fe_{17}-trigonal.

Susceptibility measurements (Figure 4.9) reveal sharp anomalies that take place at $\sim T_C$ for Fe_{17}-trigonal, corroborating the LRMO deduced from spe-

[6] see footnote 5

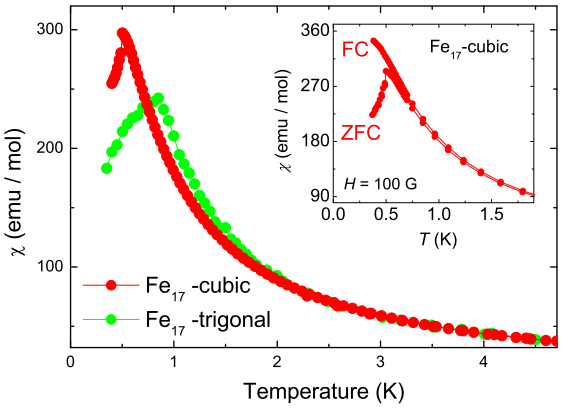

Figure 4.9: Magnetic susceptibility of Fe_{17}-trigonal and Fe_{17}-cubic for $H = 0.01$ T. Inset: Zero-field cooled (ZFC) and field cooled magnetization data for Fe_17-cubic, elucidating the superparamagnetic blocking nature of the peak at $T_B \simeq 0.5$ K (see text).

cific heat data and at $T_B \simeq 0.5$ K for Fe_{17}-cubic, whose nature is discussed below. For $T > 4$ K, both susceptibilities tend to overlap each other (Figure 4.9). The observed behavior in Fe_{17}-trigonal is compatible with a ferromagnetically ordered phase, in which demagnetization effects become important. The measured susceptibility at T_C is close to the estimated limit for a ferromagnetic grain-like sample, $\chi_N = 1/\rho N \simeq 227$ emu/mol (see Figure 4.9), where $\rho = 3.32$ g/cm^3 is the density of Fe_{17}-trigonal, and $N = 4\pi/3$ is the demagnetizing factor of the grain-like sample, approximated to a sphere. For the 5 K $\lesssim T \lesssim$ 80 K temperature range, the fit to the Curie-Weiss law $\chi = C/(T - \theta)$ for the susceptibility of Fe_{17}-trigonal corrected for the demagnetizing field, $\chi = \chi\prime/(1 - \rho N \chi\prime)$, provides $C = 175.4$ emuK/mol and $\theta = 0.9$ K, in agreement with the observed ferromagnetic order at $T_C \simeq 0.8$ K. The Curie constant C equals (within error) the expected value of a (super)paramagnet with spin $S = 35/2$ and $g = 2.06$, as deduced above from the magnetization data. This analysis is corroborated by the hysteresis loop we collected in the ordered phase (inset of Figure 4.7), for which Fe_{17}-trigonal behaves as a soft ferromagnet with a coercivity of ~ 60 Oe. We recall that from $M(H)$ curves, we estimated the anisotropy $D = -0.023$ K,

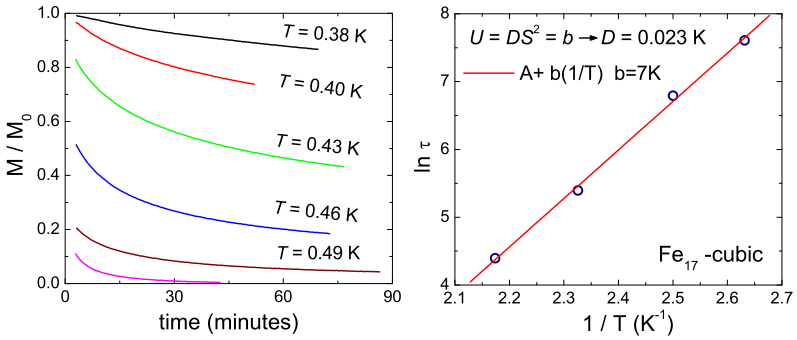

Figure 4.10: Left: Time decay of M for Fe_{17}-cubic, measured at zero-applied-field after saturation for the indicated temperatures. Right: T-dependence of τ following an Arrhenius behavior; from the linear fit the activation energy U is calculated.

which likely causes a pinning of the domain-wall motions responsible therefore for the slow decrease of the experimental susceptibility below T_C (Figure 4.9).

The occurrence of a sharp peak at $T_B \simeq 0.5$ K in the susceptibility of Fe_{17}-cubic (Figure 4.9) has apparently no counterpart in the specific heat (inset of Figure 4.8). We therefore exclude LRMO as a possible source. We recall that intermolecular distances for Fe_{17}-cubic are slightly larger than that of Fe_{17}-trigonal. It is then reasonable to assume that in Fe_{17}-cubic the intermolecular coupling is weaker, and that the molecular anisotropy is the predominant energy. This would lead to superparamagnetic blocking at T_B of the molecular spins along preferred directions dictated by the anisotropy. To better elucidate this point we performed magnetic relaxation experiments in Fe_{17}-cubic at temperatures below T_B (Figure 4.10 left panel). We firstly applied a field necessary to saturate the magnetization of the sample at 2 K. We then cooled down to a given temperature below T_B and, upon removing the field, we followed the relaxation of the Fe_{17} molecules to thermal equilibrium by collecting the time decay of the magnetization. Results are shown in the left panel of Figure 4.10, where it is seen that the decay neatly slows down below T_B, as expected for a superparamagnet. Magnetization data are well described by a stretched exponential decay $M/M_0 = \exp(-t/\tau)^\beta$ where M_0 is the initial magnetization, β the stretched parameter and τ the character-

istic decay time. The T-dependence of τ (Figure 4.10 right panel) follows an Arrhenius law providing the activation energy $U = 7.0$ K, that given $S = 35/2$ and $U = -D(S^2 - 1/4)$, corresponds to $D \simeq -0.023$ K, in well agreement with that estimated above. We note that U of the Fe_{17} molecule is about eight times smaller than that of the well-known single-molecule magnet Mn_{12}-ac [9]. As a result of similar spin dynamics, the same ratio holds for the respective blocking temperatures as well.

4.2.4 Discussions and Conclusions

The Fe_{17} molecules are magnetically isolated from each other as evidenced by the large intermolecular distances, for instance *all* Fe-Fe distances are greater than 8.7 Å for adjacent molecules in Fe_{17}-trigonal. A close inspection of the crystallography of both materials does not reveal any intermolecular superexchange pathway nor any evidence of π-stacking of the pyridine rings. These facts show that the dipolar interaction is solely responsible for the observed macroscopic behaviors. By switching from trigonal to cubic symmetry not only the arrangement and reciprocal distances of the Fe_{17} molecules are changed, but accordingly also the *dipolar interaction energies* E_{dip}. Dr. M. Evangelisti performed extensive calculations of E_{dip} assuming several magnetic configurations of $S = 35/2$ point-like dipoles arranged in analogous crystallographic lattices to that of Fe_{17}-trigonal and Fe_{17}-cubic. In particular, the position of the spins was fixed accordingly to molecular centroids. Interestingly, for E_{dip} we found up to an order of magnitude change by switching from cubic to trigonal symmetry. Since the distance between nearest neighbors change by less than 10% by switching from Fe_{17}-cubic to Fe_{17}-trigonal, one has to conclude that lattice symmetries play the major role in determining E_{dip}. This neatly illustrates that the nature of the magnetic order should not be deduced by simply comparing the ordering temperature with the interaction energy between a pair of nearest spins.

For Fe_{17}-trigonal the magnitude of the calculated E_{dip} does justify that LRMO is here driven by dipolar coupling between the molecules. We do not have, how-

ever, enough evidence to discriminate which magnetic structure is realistically the most probable one. Among the magnetic structures considered in our simulations and on basis of our experimental data suggesting a ferromagnetic nature of the ordered phase, promising candidates seem to be the alignment of the molecular spins along the [100] direction and that along the $[2\bar{2}1]$ direction. These configurations have indeed the lowest calculated values ($-E_{dip} \simeq 0.8$ K and 0.6 K, respectively), which are of the correct order with respect to the experimental $k_B T_C$. Preliminary neutron diffraction experiments performed by C. Vecchini and O. Moze (Modena) [103] have recently corroborated the onset of the magnetic phase transition for Fe_{17}-trigonal.

In conclusion, our low-temperature magnetization experiments demonstrated that Fe_{17} molecular cluster undergo either LRMO or superparamagnetic blocking of the spins depending on the symmetry. This results from the interplay of the dipolar magnetic coupling between the molecular spins, with respect to the single-molecule magnetic anisotropy. That supramolecular chemistry leads to fascinating ordered arrangements of identical high-spin nanomagnets is no novelty; that these arrangements can be achieved without affecting the magnetic properties of the individual nanomagnets (e.g. keeping unaltered the cluster spin ground-state and magnetic anisotropy) is a step forward in the manipulation of the magnetic interactions at the nanometer scale. The Fe_{17} system is therefore a test model material for the modelization of phase transitions purely driven by dipolar interactions.

Chapter 5

Linking AF molecular rings for Quantum Computation

In this chapter, I will show our characterization of AF molecular rings, linked together by supramolecular cage complexes assembly, that could have potential applications as quantum gates in quantum data processing. I will first introduce the general problem, then present the Cr_7Ni-molecular ring, which has been identified as a suitable candidate for quantum bit (qubit) encoding [104]. Finally, I will report chemical synthesis and show experimental characterization (employing PPMS magnetometry and heat capacity as well as Hall probes) of octanuclear Cr_7Ni-rings linked together into supramolecular dimers bridged by both organic and metal-organic fragments.

5.1 Introduction

It is now well established that molecular magnets are electron spin systems sufficiently decoupled from the environment to exhibit a coherent quantum dynamics: this makes them potentially interesting in view of the quantum-information processing (QIP) implementation. In a seminal paper by M. Leuenberg and D. Loss [10], high spin molecular clusters, such as Mn12, are proposed for the implementation of the Grover's algorithm, which speeds up the search of an item

in an unsorted database by a factor $\sqrt{\mathrm{N}}$ with respect to any known classical algorithm, being N the size of the database. The efficiency of this approach, where the quantum hardware consists in a single, large effective spin, essentially arises from the linear superposition of the input states and from the quantum interference between the respective outputs. In order to fully exploit the computational potentiality of a quantum system and to achieve exponential speedups, however, a quantum computer should consist in a collection of two-level subsystems (qubits), and their states be massively entangled during the time evolution. The most powerful quantum algorithms, such as the one by Shor for factorizing large integers, where shown to require proper sequences of single- and two-qbit gates, i.e. unconditional rotations of single subsystems and unitary transformations of interacting couples [105]. Indeed, this selective addressing of the different qubits and the timely tuning of the couplings between them are among the most experimentally demanding achievements on the way to the QIP implementation.

Very recently, F. Meier, J. Levy, and D. Loss [106, 107] have asserted the suitability to the application of this approach of those antiferromagnetic spin clusters characterized by a ground-state doublet, each cluster corresponding to an effective two-level system. One of the main advantages with respect to previously proposed single-spin encodings (i.e., one qubit per electron spin [108]) would arise from the largest size of the molecules, and from the resulting reduction of the spatial resolution which is required for the selective addressing of the qbits by means of pulsed magnetic fields.

5.2 The molecular Cr_7Ni as qubit

Among the above mentioned antiferromagnetic spin clusters, it has been shown by our group that the heterometallic ring $[Me_2\text{-}NH_2]^+$-$[Cr_7NiF_8(O_2CCMe_3)_16]^-$ (Cr_7Ni in short [109]) is a suitable candidate for the qubit encoding [104, 110]. The substitution of one $Cr^{III}(S = 3/2)$ ion with a $Ni^{II}(S = 1)$ provides an extra spin $S = 1/2$ to the otherwise compensated molecule, and indeed Cr_7Ni shows a $S = 1/2$ ground state. This is the first requirement for single qubit operation in a

universal quantum computation (QC) scheme. Moreover, it also posses energetic spectrum and symmetries that allow to perform the required rotations within the computational space, while keeping the occupancy of the excited states (i.e. *leakage*) negligible. This has been established performing low-temperature specific heat measurements [104,110] and successive high-field torque magnetometer [111] and inelastic neutron scattering (INS) experiments [112] to characterize the lowest lying states of the Cr_7Ni molecule. It turned out that the system exhibits at zero field a ground state consisting in a (approximated) Kramers doublet, with total spin $S = 1/2$, separated by an energy $\Delta_0/k_B = 13$ K from the first excited multiplet $S = 3/2$. While in principle anisotropy and Zeeman terms tend to mix different multiplets (S-mixing [113]), this effect is found to not significantly influence the implementation of qbit operations at low field [104, 111, 112] and S can be considered a good quantum number.

With these results, the computational basis is identified with the ground-state doublet $S = 1/2 : |\mathbf{0}\rangle|S_z = -1/2\rangle$and $|\mathbf{1}\rangle|S_z = +1/2\rangle$. The working static field and temperature are selected to initialize the system to its $|\mathbf{0}\rangle$ state, that is obtained cooling the ring to a temperature much lower than the energy splitting between the computational states, i.e. $T < B_0\mu_B/k_B$. At the same time, high energy separation between basis state and the first excited must be preserved, to avoid leakage ($L = 1 - [|\langle 0|\psi(t)\rangle|^2 + |\langle 1|\psi(t)\rangle|^2]$). This is defined as the population loss from the ground-state doublet to the higher states, that might occur during spin manipulation when dealing with *effective*, rather than a *true*, two-level systems. A reasonable compromise turns out to be $B_0 \approx 2$ T, and $T \leq 1$ K. Any quantum algorithm (i.e. rotation of the total spin S within the basis states) can be obtained by applying sequences of pulsed magnetic fields $B_1(t)$ orthogonal to the static field B_0. A further requirement for qubit encoding is that the system must have decoherence rate much higher than gating time. The latter is essentially determined by the minimum field pulse needed to perform transitions without population loss to excited states[1]; the first is caused by the coupling of the system with the solid state environment that spoils its coherent

[1]Generally, longer field pulses avoid leakage.

evolution. Calculations [104] show that, because of the relatively high value of Δ_0, a gating time of the order of 150 ps can be enough to keep leakage below 10^{-4}. Concerning the decoherence rate, specific experiments have been performed. A preliminary evaluation, obtained by magnetization measurements with resonant photon absorption, gave lower bound for $\tau_d \sim 25$ ns [114]. More recent works [115] pointed out that the main source of decoherence in the Cr_7Ni molecule is to be ascribed to the coupling to the nuclear moments of protons in the vicinity of the cluster and estimated the intrinsic τ_d as 3.8 μs for the per-deuterated Cr_7Ni-analogue. This value is much higher than the gating time, thus allowing quantum transitions to be implemented.

5.3 Molecular rings linked through Diamines and Clusters

Even if the Cr_7Ni ring represent an appealing candidate for quantum processes, an efficient implementation of a quantum computer requires the creation of a two bit quantum gate [106,107,116], that in turns requires entanglement between two Cr_7Ni rings. Such systems have been obtained by the chemist group of Dr. G.A. Timco and Prof. R.E.P. Winpenny in Manchester.

Since the ring is templated about protonated amine cations, a straightforward method is to use a diamine with a carbon chain of sufficient length so that a Cr7Ni ring at either end can be attached. In initial experiments they find that amines that work include 1,8-diaminooctane (1,8-dao), 1,9-diaminononane (1,9-dan), while slightly more complex diamines such as 1,3-di(piperidine)propane (1,3-dpp) also produces a pair of linked clusters. Longer diamines also work, e.g. 1,12-diaminododecane (1,12-dad), but the resulting crystal structures are significantly disordered. The linked clusters, [1,8-daoH$_2$][$Cr_7NiF_8(O_2CCMe_3)_{16}$]$_2$(**1**), [1,9-danH$_2$][$Cr_7NiF_8(O_2CCMe_3)_{16}$]$_2$(**2**) and [1,3-dppH$_2$][$Cr_7NiF_8(O_2CCMe_3)_{16}$]$_2$(**3**) have been structurally characterised [2] (See Figure 5.1).

[2]for more details on the chemical synthesis method we refer to [117] and references therein

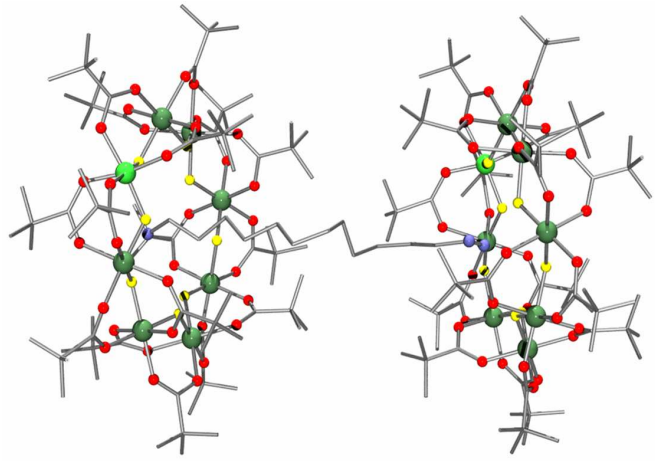

Figure 5.1: Crystal structure of **1** (Hydrogen atoms and methyl groups have been omitted for clarity; Cr green, Ni light green, F yellow, O red, N blue, C black). Selected bond-length ranges: M−F 1.891−1.964, M−O 1.872−2.016 Å. Average estimated standard deviation (av esd): 0.012 Å.

A further step forward will be to include switchable magnetic links between the rings. To this end chemists have synthesized $[EtNH_2CH_2py][Cr_7NiF_8(O_2CCMe_3]_{16}]$ (**4**; py=pyridine) knowing that the ring will encapsulate the secondary ammonium group leaving the pyridine free to bind to further metal sites. To illustrate the potential of such an approach they reacted **4** with dinuclear metal complexes, $[Cu_2(O_2CCMe_3)_4(HO_2CCMe_3)_2]$ and $[M_2(H_2O)(O_2CCMe_3)_4(HO_2CCMe_3)_4]$ (M = Ni or Co). This gave the structures $[M_2(O_2CCMe_3)_4[EtNH_2CH_2py][Cr_7NiF_8$-$(O_2CCMe_3]_{162}]$ (**5:** M = Cu; **6:** Ni; **7:** Co) [117] depicted in Figure 5.2. The pyridine from **4** binds to the axial sites of the metal dimer. The M−M distance is fairly constant at 2.63 Å in **5** in 2.61 Å in **6**. The Cu−Cu distance is similar to that in a previous copper dimer bridged by pivalate [118]. In related Ni dimers [119] the Ni−Ni distance depends on the terminal ligands, being ca. 2.60 Å for pyridine and longer for lutidines (ca. 2.72 Å). Complex **4** therefore appears to be similar to pyridine in its donating properties. While these dimers are not switchable, equivalent supramolecules can be made, where M = a 4d or 5d metal and where the interaction between the $[Cr_7MF_8(O_2CCMe_3)_{16}]$ complexes can be varied by

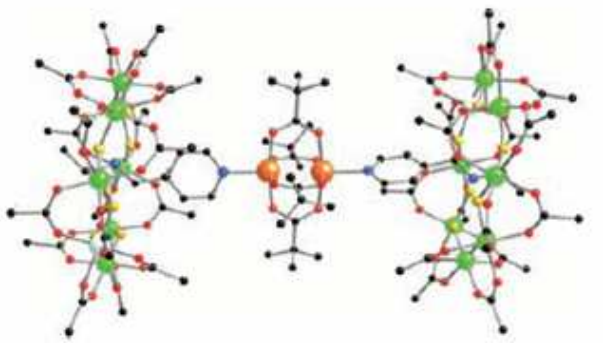

Figure 5.2: Crystal structure of **5** (see Figure 5.1 for color scheme; Cu orange). Selected bond length ranges: M−F 1.909−1.967, M−O 1.914−1.997, Cu−O 1.953−1.960 Å. Av esd: 0.008 Å.

redox chemistry or photoexcitation of the multiply bonded dimer [120].

5.4 Experimental Results

Magnetic and specific heat studies of **1**−**3** and **5**−**7** were performed. The ac susceptibility was measured in the temperature range 2−100 K on different derivatives(Figure 5.3). Data were collected on polycrystalline samples using the Quantum Design PPM system. Each linked ring essentially show the same χT versus T behavior for this temperature range and, after normalization to half a mole, the $\chi T(T)$ curves overlap that of molecular Cr_7Ni ring, i.e. isolated $[Cr_7MF_8(O_2CCMe_3)_{16}]$ complexes. The anomalies in the χ versus T plot (reported in the inset of Figure 5.3) were related to the pattern of the lowest lying states in a single Cr_7Ni ring [104, 109] that comprises a $S = 1/2$ as a ground state and a $S = 3/2$ as first excited multiplet. The field-dependencies of the magnetization as collected at $T = 0.4$ K for each linked ring (employing the Hall probe magnetometer) almost overlap one another and, since at this temperature only the ground state is significantly populated, no deviation from the Brillouin curve calculated for $S = 1/2$ is observed (Figure 5.4).

The temperature-dependencies of the specific heat c, normalized to the gas constant R, were recorded for the range 0.4 K $< T <$ 10 K, using the PPMS

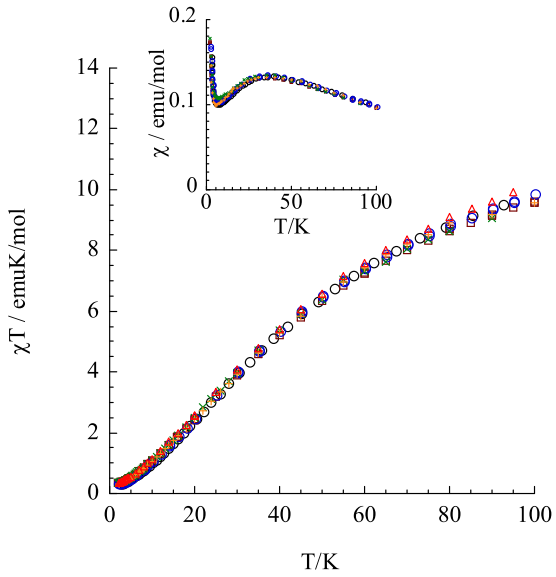

Figure 5.3: The χT product of Cr_7Ni (black circles) and of the molecular dimers **1** (brown squares), **2** (blue circles), **3** (red triangle), **5** (green crosses), **6** (yellow crosses) (in the case of **1**−**6**, was normalized to half a mole) for the temperature range 2−100 K. Note that χT values saturate al low T to the Curie value expected for a $S = 1/2$ for all the derivatives. Inset: temperature-dependence of the ac susceptibility χ.

microcalorimeter and Helium-3 insert. Figure 5.5 shows that also in this case, after normalization to half a mole for the dimers, the data overlap one another and with those of Cr_7Ni. The hump in the $c(T)$ curves at $3 - 5$ K confirms the Schottky anomaly related to the main energy gap, approximately 9 cm^{-1}, between the ground state $S = 1/2$ doublet and the $S = 3/2$ quartet. As a magnetic field is applied, these multiplets are split and the Schottky anomaly evolves for all derivatives similarly to what observed for Cr_7Ni ring [104]. This behavior is well accounted by the spin hamiltonian of a single wheel:

$$\begin{aligned}\mathcal{H} &= \sum_i J\boldsymbol{S_i}\cdot\boldsymbol{S_{i+1}} + \sum_i d_i[S_{z,i}^2 - S_i(S_i+1)/3] \\ &\quad + \sum_{i<j}\boldsymbol{S_i}\cdot\boldsymbol{D_{ij}}\cdot\boldsymbol{S_j} + \mu_B\sum_i g_i\boldsymbol{S_i}\cdot\boldsymbol{B}\end{aligned} \tag{5.1}$$

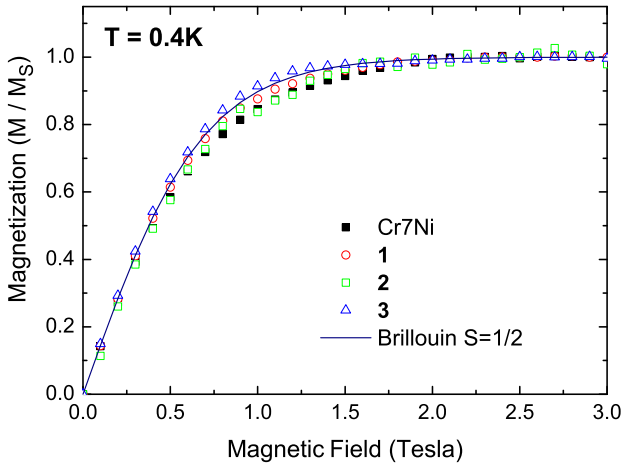

Figure 5.4: Magnetization of Cr_7Ni and derivatives **1**−**3** at 0.4 K, measured by Hall probe. No deviations from the Brillouin behavior of an effective $S = 1/2$ are evident.

where the first term corresponds to the dominant antiferromagnetic Heisenberg exchange between nearest neighboring spins; the second and third anisotropic terms account for the coupling due to the crystal field and for the intracluster dipole-dipole interaction, respectively; the fourth term accounts for the Zeeman coupling to the external field. The microscopic parameters can be determined by fitting the magnetic-field dependent specific heat data and, within the experimental accuracy, for all derivatives the best set of parameters was: $J_{Cr-Cr} = 1.46$ meV, $J_{Cr-Ni} = 1.69$ meV, $d_{Cr} = -0.03$ meV, $d_{Ni} = -0.35$ meV, $g_{Cr} = 1.98$ and $g_{Ni} = 2.2 \pm 0.2$. The addition of a coupling term between two wheels does not improve the quality of the fit for $T > 0.4$ K.

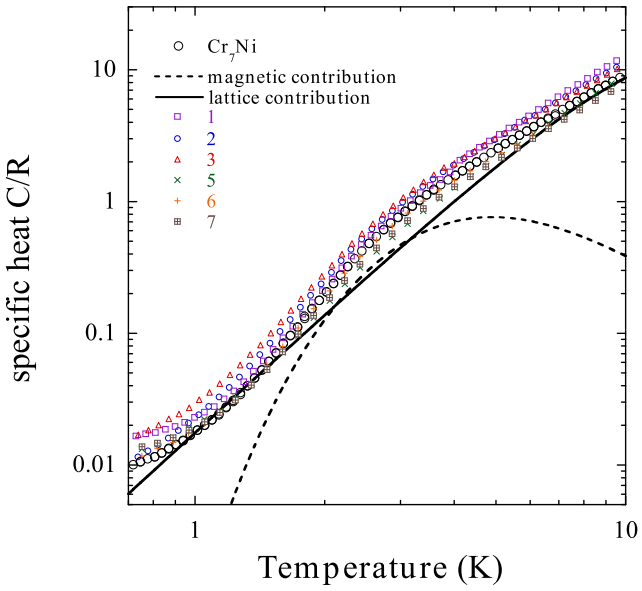

Figure 5.5: Specific heat C, normalized to the gas constant R, of Cr_7Ni (squares) and of the molecular dimers **1**−**3** and **5**−**7** (in these cases C was normalized to half a mole for comparison with Cr_7Ni) measured as a function of temperature in zero field. Continuous and dotted lines represent the estimated lattice and magnetic contribution respectively.

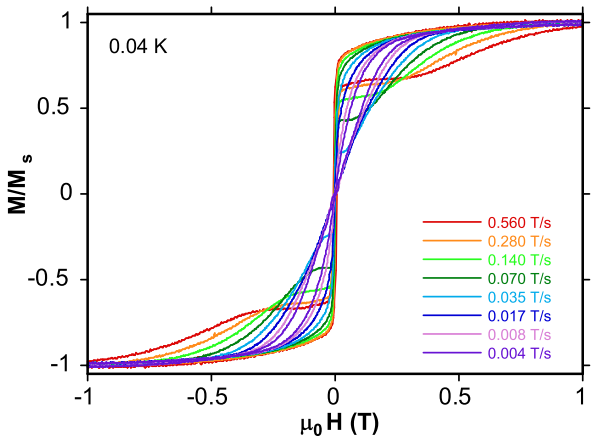

Figure 5.6: Magnetization cycles measured on derivative **5** at 40 mK at different sweeping rates. No anomalies are evident at small fields, indicating that the magnetic link between two rings is vanishing. The hysteresis is quite similar to what observed for Cr_7Ni reported in [114], where it is ascribed to phonon bottleneck.

5.5 Conclusions

The above results show, therefore, that for all these complexes the pattern of the lowest lying states of a single wheel is very close to that of the isolated Cr_7Ni ring. An upper limit for a possible coupling between two wheels has been estimated to be weaker than ~ 0.1 cm^{-1}. To check this, in collaboration with Dr. W. Wernsdorfer (Grenoble) the magnetization of micro-crystallites of **5** between 40 mK and 400 mK has been measured using a micro-SQUID array (Figure 5.6). No evidence for an interaction between the Cr_7Ni rings has been found even at this temperature.

At one level the lack of a sizeable magnetic coupling may seem disappointing, however this work proves that $[Cr_7MF_8(O_2CCMe_3)_{16}]$ complexes are relatively stable and that they can be attached to one another by different linkers. At another level, implementation of quantum computing will require one state where the single qubits in the gate do not communicate. These results show that the rings can be brought into close proximity without changing magnetic behavior

due to through-space exchange.

In future works we will study clusters with switchable interactions, using light or redox-chemistry, employing other metal-organic linkers.

Chapter 6

High Temperature Slow Relaxation of the Magnetization in the Ni_{10} molecule

In this chapter, our experimental measurements on a novel family of molecular clusters containing 10 Ni-ions will be discussed. Ni_{10} has been magnetically characterized in our laboratory employing PPMS-magnetometry options and Hall probes. It presents very slow relaxation of magnetization at temperature as high as $\sim$ 15 K that can not be explained in the framework of conventional mechanisms, since it occurs in the absence of anisotropy barrier, intermolecular exchange or disorder, or phonon bottleneck. In collaboration with the group of prof. Giuseppe Amoretti, Prof. Paolo Santini and Dr. Stefano Carretta (Parma) we attributed this extraordinary feature to the atypical magnetic spectrum of Ni_{10}, that shows a dense band of low-lying energy levels. This causes resonant phonon trapping to occur, breaking the standard picture of phonon-assisted relaxation and hence leading to the blocking of M.

6.1 Introduction

One of the most debated issues in the physics of magnetic molecules is how the spin dynamics are affected by interactions of spins with other degrees of freedom, in particular nuclear spins and phonons [2, 9, 121–124]. These interactions induce decoherence of the spin dynamics, usually leading to relaxation of molecular observables to their thermal equilibrium value. The comprehension of these relaxation mechanisms in crystals containing magnetic molecules is not only an intriguing issue of fundamental interest, but it is also of critical importance for the envisaged technological applications of these molecules as classical or quantum bits. For temperature $T \gtrsim 1$ K relaxation is due to spin-phonon interactions, with phonons behaving as heat bath and inducing thermalization by irreversible exchange of energy with spins. When T is increased, relaxation times drop because phonon populations n_{ph} rise very rapidly. The class of molecules relaxing in macroscopic times at the highest T ($\lesssim 3$ K) is that of molecular nanomagnets [2, 9, 122], where the reversal of the magnetization M is hampered by a uniaxial anisotropy energy-barrier. Other mechanisms potentially leading to blocking of M are intermolecular exchange interactions or, at very low T ($\lesssim 1$ K), phonon bottleneck due to the smallness of the lattice heat capacity.

We studied a family of molecular crystals, containing *noninteracting* magnetic Ni_{10} molecules, which we find to display slow relaxation of M below about 17 K in the lack of any anisotropy barrier. Thus, Ni_{10} is not a molecular nanomagnet: the high-T non-equilibrium behavior is completely different from that observed in nanomagnets and cannot be explained within the above-outlined framework of phonon-assisted relaxation. The distinguishing feature of Ni_{10} is a magnetic spectrum with a dense band-like group of states at low-energy, well separated (by 14 meV) from all other levels. We suggest that this causes an unprecedented form of resonant phonon trapping [125], and a resulting breakdown of the heat-bath assumption for phonons: phonon populations n_{ph} are not fixed solely by the thermostat temperature, but also result from the very slow joint dynamics of phonons and spins. The resulting cooperative many-time-scales magnetic dy-

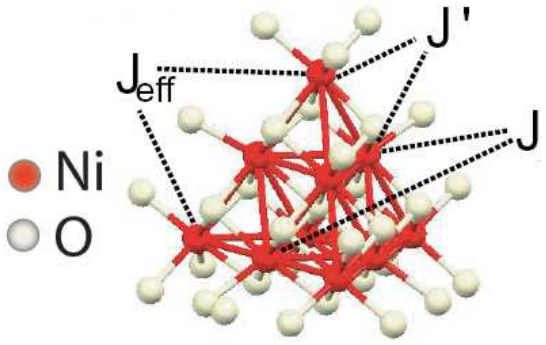

Figure 6.1: Molecular structure of Ni_{10}(EtOH). Ni-Ni bonds are guides to the eye.

namics partially recalls that of spin-glasses, but here it is associated to neither interactions nor disorder.

6.2 The Ni_{10} Molecule

The Ni_{10} family of compounds has been synthesized by the group of Dr. E.J.L. McInnes (Manchester). Every compound has a magnetic core consisting in 10 Ni^{2+} ions arranged on a super-tetrahedron (Figure 6.1 and [126]). Ni_{10} cores are well separated and embedded in crystalline-ordered molecular structures, where the molecular and crystal symmetries are dictated by the specific organic ligands used. The preparation and the structure of $[Ni_{10}(O)(thme)_4(dbm)_4(O_2CPh)_2(EtOH)_6]$ ("Ni_{10}(EtOH)") have been previously reported [126].

The six Ni ions bisecting the edges of the supertetrahedon can be divided into three pairs, each pair of ions being connected by a linear Ni-O-Ni superexchange bridge passing through the center of the tetrahedron. This bridge yields a very strong antiferromagnetic (AF) interaction $J\mathbf{s}_a \cdot \mathbf{s}_b$ between the s=1 spins of the two Ni ions in each pair. Other superexchange interaction constants are expected to be much weaker, in particular the one (J') between these six Ni ions and the four Ni ions at the vertices. Therefore, we expect the six central Ni ions to be frozen in a nonmagnetic singlet state for $k_BT \ll J$, separated by a large gap of

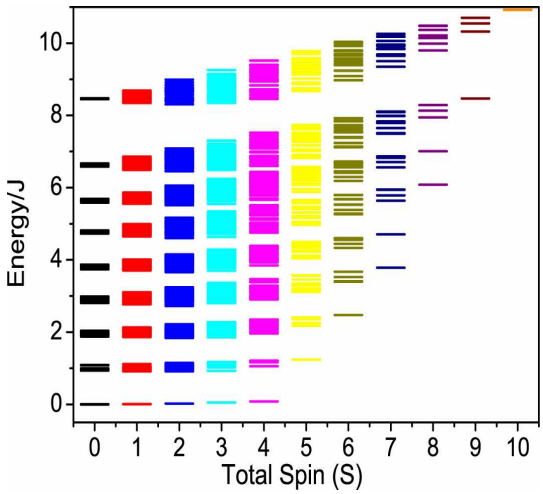

Figure 6.2: Energy of exchange multiplets of Ni10 as a function of the total spin S. The band-like structure is clearly visible. The energy separation between contiguous bands is of the order of J.

order J from excited states. The four vertex Ni ions are then coupled to each other only in second and higher order perturbation theory with respect to J'/J. Thus, the exchange energy spectrum consists of a series of bands of states of width $\simeq J'^2/J$ separated by large gaps of order J (Figure 6.2). The lowest-energy band contains 19 total-spin multiplets for a total 81 levels, and its exchange structure is approximately described by an AF effective Hamiltonian

$$\mathcal{H}_{\text{eff}} = J_{\text{eff}}/2 \sum_{i \neq j=1,4} \mathbf{s}_i \cdot \mathbf{s}_j \tag{6.1}$$

with $J_{\text{eff}} \propto J'^2/J$.

6.3 Experimental Results

The spectral structure sketched above is confirmed by fits of the T- and field-dependence of the dc-magnetization M measured on powder and single-crystal samples (Figures 6.3 and 6.4). The Ni_{10} molecule has been experimentally characterized in the temperature range $2-300$ K, employing PPMS magnetometry on

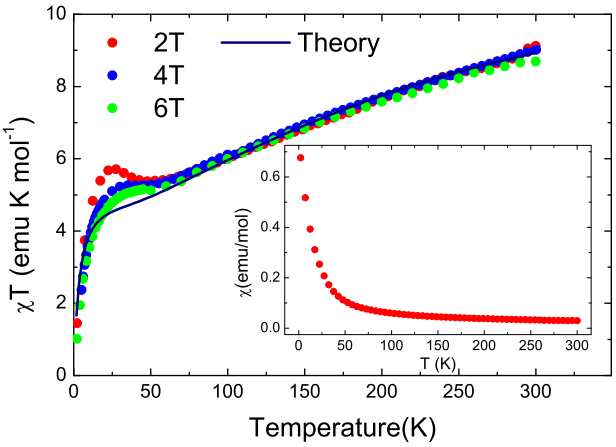

Figure 6.3: Measured T- and H-dependence of $\chi_{dc}T$ ($\chi_{dc} = M/H$). The blue curve is the theoretical fit assuming equilibrium. Inset: $\chi_{\rm dc}$ at 2 T displays no anomalies.

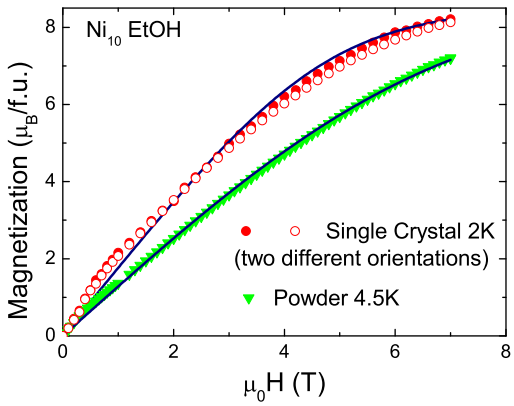

Figure 6.4: Magnetization measurements performed at 2 K on single crystal in two different orientation with respect to the applied field (red circles empty and filled) and at 4.5 K on powder sample (green). Absolute values were scaled with powder data.

powder samples and by means of Hall probe for single crystal measurements. By diagonalizing the full Hamiltonian of the 10 Ni spins, $J \simeq 14.6$ meV, $J' \simeq 1.1$ meV and a Ni^{2+} gyromagnetic factor $g \simeq 2.25$ have been found. The spectrum contains a low-lying band of states well separated (by about 14 meV) from higher-lying

states (see Figure 6.2). All these parameters have been determined by fitting only high-T and/or high-field magnetization data, since, as it will be shown later, for small fields H and temperatures T the Ni_{10} molecule is not at equilibrium on the time scale used for this type of measurements (indeed for small H $\chi_{\rm dc}T$ displays a peak below ~ 20 K that is not reproduced by our model). However, we found that at high-T and/or high-field preparation-dependence and nonlinearity tend to disappear.

As far as magnetic anisotropy is concerned, we have made measurements on different single-crystals and we have found *no angular dependence* of M within our experimental accuracy. [1] The most important anisotropic contribution is the coupling of the four vertex s=1 Ni^{2+} spins with the crystal-field (CF) generated by their ligands. The local symmetry at the vertex sites is very low, with a first shell of ligands forming distorted octahedra. A simple possible choice for the local CF is a coupling of the form $H_{CF} = \sum_{i=1,4} d(s_{\zeta_i}^2 - s(s+1)/3)$, where s_{ζ_i} is the component of the spin of the ith vertex ion along the corresponding tetrahedron axis. For Ni^{2+} in distorted octahedral environment the CF parameters have typically values of a few cm^{-1} [127]. Thus, for the theoretical calculations, d has been fixed to $= -1$ $cm^{-1} \simeq -0.12$ meV. This CF has overall tetrahedral symmetry and produces only tiny dependence of $M(\mathbf{H})$ on the orientation of $\mathbf{H}$, as found experimentally. We have checked that other choices for the sign and the value of d or other possible forms of $\mathcal{H}_{\rm CF}$ lead to similar results. At last, the small intramolecular dipolar interaction is evaluated in the point-dipole approximation. The calculated lowest energy band is shown in Figure 6.11**a**.

In Figure 6.3, $\chi_{\rm dc}T$ shows a bump at ~ 20 K. In Ref. [126] this behavior had been tentatively ascribed to the appearance of long-range magnetic order. Yet, this looked odd since no intermolecular exchange pathway could be identified and $\chi_{dc}(T)$ displays no anomalies, as shown in the inset of Figure 6.3. By synthesizing and analyzing various Ni_{10} derivatives we have also established that changing the ligands, and therefore the packing and distances between different molecules

[1] an exemplum is given in Figure 6.4, where magnetization data taken on single crystals at two different orientations with respect to the external field are shown.

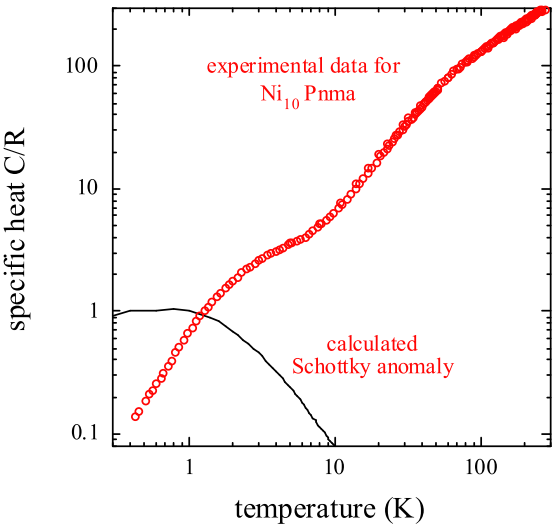

Figure 6.5: Temperature dependence of specific heat C (normalized to the gas constant $R = 8.314\ Jmol^{-1}K^{-1}$) measured by using the two-tau relaxation method on two (0.7 and 2.6 mg) polycrystalline Ni_{10} samples. Typical relaxation times were of the order of tens of seconds for each point. The magnetic contribution C_m is calculated by considering the lowest lying energy band of Ni_{10}.

leaves the susceptibility behavior almost unaffected. Moreover, we have also measured the specific heat of Ni_{10}(EtOH) and we find no anomalies in its T-dependence (Figure 6.5). Thus, long-range magnetic order must be ruled out.

The low-T behaviour is a nonequilibrium and this is directly evidenced by the fact that the low-field magnetization M is markedly time- and history-dependent for $T \lesssim 17$ K. In particular, M exhibits different behavior if a zero field cooling (ZFC) or field cooling (FC) procedure is used (Figure 6.6). The ZFC curves lie below the FC one, and with $H = 100$ G the opening of the ZFC and FC curves occurs at $\sim$15 K close to the temperature of the maximum in the ZFC magnetization curve (Figure 6.6). Furthermore, $M(H)$ at fixed T displays hysteretic behavior (Figure 6.7).

To clarify these points, we measured the time evolution of M using different preparation procedures. Some results are reported in Figure 6.8. The typical

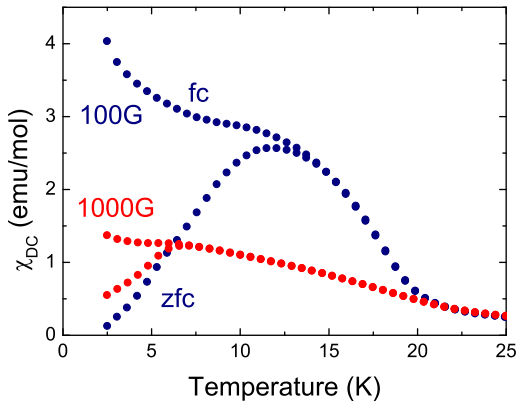

Figure 6.6: ZFC and FC powder susceptibility. The procedures was the following: T is initially set to 40 K and H to zero. The sample is cooled at 2 K/min down to 2 K. At 2K, H is switched on. ZFC measurements are taken by warming the sample up to 25 K, typically in ∼1 hr. FC measurements are taken by cooling down to 2K at the same rate, keeping the field switched on.

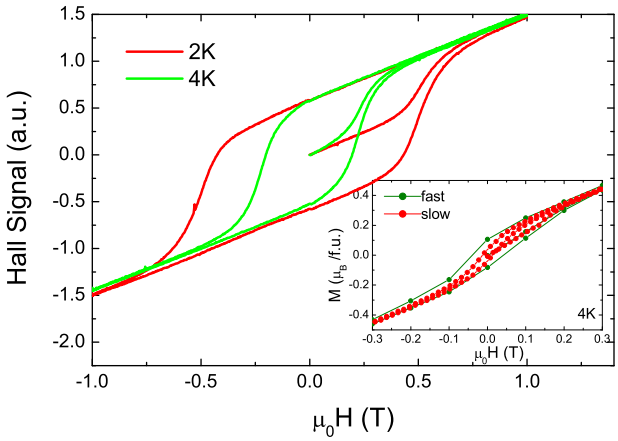

Figure 6.7: Low temperature magnetization of a Ni_{10} single crystal measured at 2 K with a Hall probe, showing hysteretic behavior. Inset: zoom view of the powder curve at 4 K. The hysteresis curve is different for powder and single crystal due to a different surface/volume ratio and hence different thermal coupling with the cryostat. In addition, it also depends on sweeping rate: here the green curve is measured ten times faster than the red.

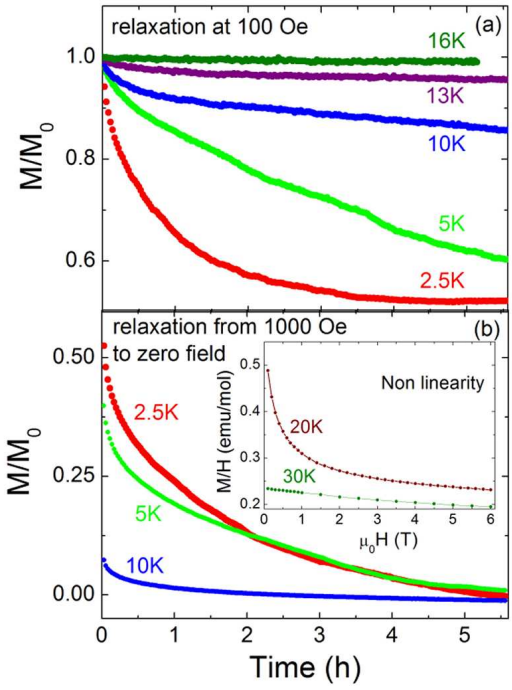

Figure 6.8: **(a)** Relaxation of M after preparation in FC conditions. A powder sample is cooled in a field of 100G from 40K at 2K/min down to a fixed temperature $\tilde{T}$. When $\tilde{T}$ is reached, relaxation starts (time t=0). $M_0 = 0.075, 0.074, 0.059, 0.049, 0.034$ μ_B/f.u. from bottom to top. **(b)** Relaxation in the same condition as in **(a)**, but the cooling is in 1000G and the field is switched off as soon as $\tilde{T}$ is reached. $M_0 = 0.25, 0.24, 0.2$ μ_B/f.u. from top to bottom. Inset: M/H vs H, clearly showing the nonlinear behaviour of M, even for T as high as 20K or 30K.

relaxation behavior is multi-exponential: a first fast decay (few seconds and less) followed by a second relaxation time-scale of few minutes, a further decay on the time scale of a few hours, and finally a slow drift on the time scale of days or even longer. Starting from the ZFC curve, M increases with time, whereas it decreases when starting from the FC curve. In addition, the long-time value of M is significantly different for FC and ZFC protocols (Figure 6.9). This means that the system does not relax to equilibrium within the experimental timescale, but rather it gets trapped in preparation-dependent out-of-equilibrium states. Remarkably, if Ni_{10} is field-cooled in a magnetic field, when the field is switched

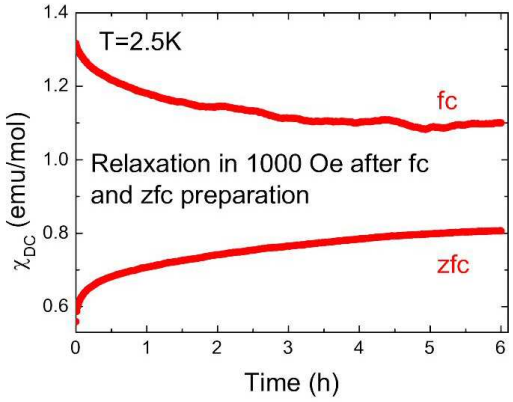

Figure 6.9: Relaxation after preparation in ZFC and FC conditions. ZFC: powder sample is cooled in zero field from 40 K at 2 K/min down to 2.5 K ($T = T_0$). Then the field is switched on and relaxation starts (time $t = 0$); FC: powder sample is cooled in field ($H_{\rm ext} = 1000$ Oe) from 40 K at 2 K/min down to 2.5 K ($T = T_0$). When T_0 is reached, relaxation starts ($t = 0$). Note that the two saturation values are different, meaning that they are not the true equilibrium states. The system is relaxing towards states of metastable equilibrium (history dependents), in agreements with our predictions.

off a sizeable fraction of the magnetization M is retained for hours (Figure 6.8**b**).

The ac-susceptibility $\chi_{ac}(T, f)$ has been measured at different frequencies f. Both the in-phase $\chi_{ac}\prime$ and the out-of-phase component $\chi_{ac}\prime\prime$ (Figure 6.10 abruptly increase below 20 K, and they show peaks at ∼17.5 K, ∼13 K and ∼8 K. We define a blocking temperature T_0 in correspondence of the first peak in $\chi_{ac}\prime\prime$. The temperature at which χ_{ac} peaks depends very weakly on frequency. This behavior is remarkably different from that of a nanomagnet and an unphysical value of the anisotropy barrier is obtained by assuming an activated Arrhenius mechanism. Moreover, there is evidence that Ni_{10} is still in a nonequilibrium long-living state up to ∼2 T_0. In fact, $M(H)$ is nonlinear even for tiny H (inset of Figure 6.8**b**), where any equilibrium model would predict perfect linearity since $\mu_{\rm B}H/k_{\rm B}T \ll 1$. However, this is not accompanied by relaxation on the time scale of few hours for $T > T_0$.

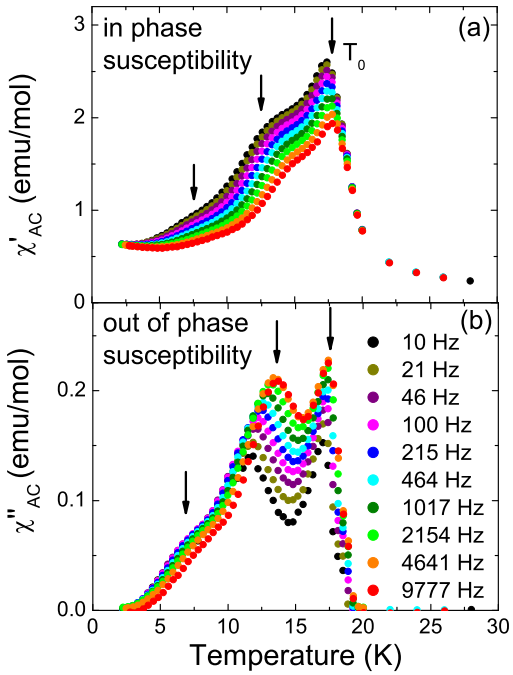

Figure 6.10: In-phase **(a)** and out-of-phase **(b)** components of χ_{ac} measured on powder Ni_{10}(EtOH) with an AC field of 10 Oe at different frequencies. Data are taken on cooling, and a typical measurement from 30K to 2K lasts ∼2 hrs.

6.4 Theoretical Model

The above mentioned experimental results show that Ni_{10} displays nonexponential relaxation with many time scales below T_0 and it is characterized by a nonlinear $M(H)$ up to $\sim 2T_0$. Since Ni_{10} has no anisotropy barrier, the observed long relaxation times cannot originate from the same phonon-assisted barrier-crossing mechanism as in nanomagnets. The relaxation properties of Ni_{10} have been theoretically analyzed by Dr. Stafano Carretta, prof. Paolo Santini and prof. G. Amoretti (Parma). When the Ni_{10} is in contact with the phonon heat bath, the main contribution to the magnetoelastic (ME) coupling comes from the modulation of the electric-quadrupole moment of each Ni ion by phonons [124], which leads to a relaxation dynamics for the spins described by transition rates W_{st} between levels t and s given by

$$W_{st} = \alpha\pi^2\Delta_{st}^3 n_{ph}(\Delta_{st}) \sum_{i,j=1,10} \sum_{q_1,q_2=x,y,z} \langle s|O_{q_1,q_2}(\mathbf{s}_i)|t\rangle\langle s|O_{q_1,q_2}(\mathbf{s}_j)|t\rangle \qquad (6.2)$$

where the first sum runs over Ni ions, $O_{q_1,q_2}(\mathbf{s}_i) = (s_{q1,i}s_{q2,i} + s_{q2,i}s_{q1,i})/2$ are quadrupolar operators, $n(x) = (e^{\hbar x/k_B T} - 1)^{-1}$ and $\Delta_{st} = (E_s - E_t)/\hbar$. Equation 6.2 is based on the simplest conceivable Debye model for phonons in which each Ni ion experiences a spherically symmetric ME coupling, but results do not depend qualitatively on this specific choice. The single free parameter α characterizes the coupling strength, and it is expected for Ni^{2+} to be of the order of 10^{-4} THz^{-2}. At $T = 5$ K this yields relaxation times of less than about 10^{-8} sec, i.e. hugely shorter than the observed times. Thus, the observed high-T nonequilibrium behavior cannot be explained within the conventional framework of phonon-assisted relaxation.

In the preceding analysis, a crucial assumption is that phonons behave like a heat bath, establishing thermal contact with the thermostat instantaneously. This assumption requires that once a phonon is emitted by a molecule, it is not further reabsorbed by other molecules. The issue of the behavior of a system in which this assumption breaks down is an old and very complex one, which for simple 2-level model systems has been tackled in the past from several perspec-

tives [125, 128, 129]. Reabsorption by nearby spins may lead to resonant trapping of the phonons involved in the relaxation process. An intuitive picture [125] for an ensemble of 2-level systems is that a resonant phonon is continuously emitted and reabsorbed until by chance it is emitted on the wing of the resonance line, where its free path is larger than the sample size L. Let $K(E)$ be the absorption coefficient, i.e. the probability of phonon absorption per unit length. By defining the energy E_c such that $K(E_c)L = 1$, the trapping time τ in units of emission time T_1 will be approximately the ratio of the whole line intensity to the intensity beyond E_c. Magnetic molecules have generally well-separated energy levels, and are qualitatively similar to the above-mentioned 2-level systems. Therefore we may generally expect effects on relaxation similar to those of 2-level systems, i.e. at very low T only.

However, two features of Ni_{10} make it atypical: the first one is the presence of a dense band of low-lying levels. The second one is the highly non-axial character of the anisotropy. As a result, the ME interaction, which is quite large for Ni^{2+}, can induce transitions between virtually all pairs of levels, and the energies of many of these transitions are close to each other on the scale of level widths (typically a few μeV [130]). Thus, the E-dependence of the absorption coefficient $K(E)$ is very different from that of a two-level system and recalls that of a band (Figure 6.11**b**). The red line in Figure 6.11**b** represents a typical phonon emission spectrum corresponding to a given transition. By using the same rough line of reasoning as above, τ should be proportional to the ratio of the whole red line intensity to its intensity beyond $E_c/k_B \sim 9$ K. This number is clearly huge, implying that phonons with $E < E_c$ experience almost complete trapping, and the crystal is opaque to them[2]. As a result, the phonon populations $n_{ph}(E)$ are not fixed to their thermal-equilibrium value as in Equation 6.2, but evolve slowly in time jointly with spin populations. Modelling this dynamics is nontrivial even for the much simpler single-resonance two-level systems [128, 129]. Here, besides having thousands of involved resonances, there is the additional fundamental

[2]Spatial diffusion of the trapped phonons is neglected as the diffusion time to the thermostat is huge.

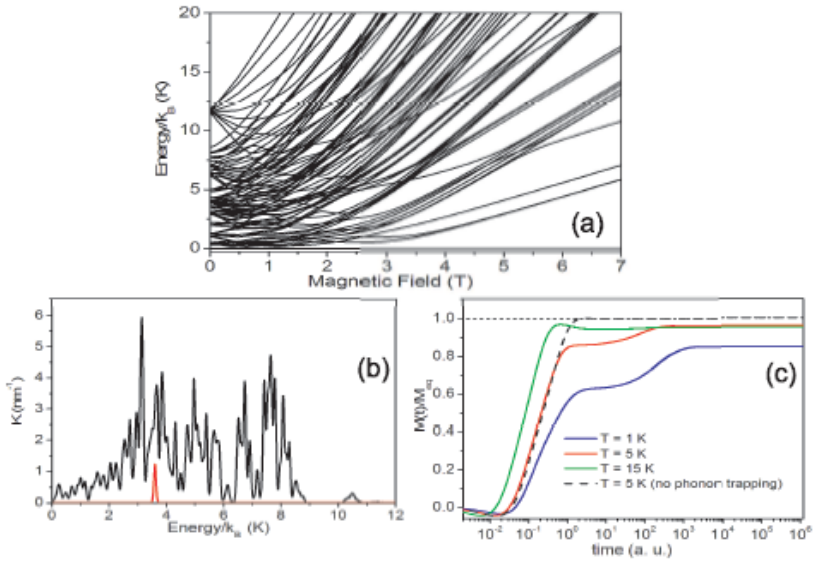

Figure 6.11: **(a)** Energy levels of the lowest-lying band as a function of **H** (oriented along one of the four tetrahedron axes). **(b)** High-T absorption coefficient $K(E)$, calculated as $K(E) = \sum_{s>t} W_{st}(N/V)P_{st}(E)/(81c\rho(E))$, where W_{st} are given by Equation 6.2 with $\alpha = 10^{-4}$ THz^{-2}, $c = 3 \times 10^5$ cm/sec is the sound velocity, $\rho(E)$ is the phonon density of states (assumed Debye), and $P_{st}(E)$ is a lineshape, assumed to be a gaussian centered at $E_s - E_t$ with a standard deviation $\sigma/k_B = 0.04$ K ($H = 100$ G). Lorentzians yield an even denser spectrum. **(c)** Calculated time-dependence of M/M_{eq} (M_{eq} being the equilibrium value of M) for three representative temperatures (continuous lines) and $H = 100$ G. The dashed line represents $M(t)$ at 5 K calculated by neglecting phonon trapping. Initial conditions are equipopulation for magnetic levels and equilibrium occupations for phonons.

difficulty that since relaxation times are longer than the experimental window, initial conditions for populations depend in unknown way from the system history.

To grasp some essential features of the relaxation behavior of Ni_{10} in the trapped-phonon regime, it has been modelled by a system of coupled integro-differential master equations. These describe the joint evolution of the populations of the molecular magnetic levels of the lowest band $p_l(t)$ ($l = 1, 81$), and of the occupation numbers of Debye acoustical phonons $n_{ph}(E, t)$(as in, e.g. [128]). The t-dependence of p_l and n_{ph} is calculated numerically. Some results are shown in Figure 6.11**c**. The model captures several key properties evidenced by experimental data. First of all, it displays virtually infinite relaxation times even for a degree of trapping much smaller than that expected from Figure 6.11**b**. At large times the dynamics gets trapped in non-equilibrium states, as experimentally observed. The calculated time-dependence (Figure 6.11**c**) is preparation-dependent and non-exponential, similarly to what observed experimentally (Figure 6.8). As T is increased, phonon trapping progressively gets less effective, and observables relax faster to non-equilibrium values closer to equilibrium ones. In addition, if the applied field intensity is increased, trapping is reduced because of the progressive opening of transparency windows in the phonon absorbance $K(E)$. This agrees, for example, with the lowering of the FC-ZFC splitting temperature, and with the fact that peaks in the ac-susceptibility (Figure 6.10) disappear when H is increased.

The model only mimics the lowest energy band of Ni_{10}, while real Ni_{10} has an additional energy scale, i.e. the gap (about 14 meV) separating ground- and first-excited bands. Thus, Ni_{10} can also relax by Orbach processes exploiting high-E phonons to bridge this gap. This induces an abrupt fastening of the relaxation dynamics around 20 K, and we interpret the characteristic temperature-scale T_0 as the one marking the onset of these inter-band processes.

6.5 Conclusions

Our experimental data have showed that Ni_{10} provides the first example of a novel kind of slow magnetic dynamics which occurs in the lack of magnetic interactions and anisotropy barriers. This high-T nonequilibrium behavior is completely different from that observed in molecular nanomagnets and cannot be explained within the conventional framework of phonon-assisted relaxation. In collaboration with the group of Parma, we propose an unprecedented form of resonant phonon trapping to occur, leading to a breakdown of the heat-bath assumption for phonons. Similar slow dynamics, even at higher T, is expected to characterize molecular systems with analogous energy spectrum.

Chapter 7

General Conclusions

In this work, I succeeded to implement Hall micro probes for magnetometry within a commercial Quantum Design PPM-System. I showed that they can be mounted in different inserts (standard Sample Puck, Horizontal Rotator, Helium-3, etc...) in combination with the P-400 Resistivity Option or even in a custom-made probe, that, for example, could allow to take measurements in the presence of different types of excitation (in our case, light or microwaves). For this system, Hall probes thus represent a sensitive magnetometers that can be employed even at temperatures below 1.8 K. Using the implemented set-up I investigated the magnetic properties of novel classes of molecular nanoclusters in temperatures down to 0.3 K and in an applied filed range of $0 - 7$ T.

Fe_{14} molecular nanomagnet has shown huge magnetocaloric effect for temperatures below ~ 10 K, mainly because of the special combination of low anisotropy and unusually large ground state spin S. Researches are currently in progress on a new family of Mn-clusters (namely Mn_{24} and Mn_{32}), that add to low anisotropy and large spin a third key ingredient for MCE: frustration. It is indeed known that when it is not possible to satisfy all the interactions, the system will show a multiplicity of similar low energy levels rather than a well defined unique ground state. As partially enlightened also in the Fe_{14} molecule, this increases the total amount of entropy associated with the system, enhancing the magnetocaloric effect.

Employing Hall probes for magnetometry in the Helium-3 temperature region, we studied the competition between single molecule anisotropy and dipolar coupling in the Fe_{17} nanomagnet. We revealed how it can be tuned by changing the symmetry with supra-molecular chemistry, leading to either long range magnetic order or superparamagnetic blocking of the spins. More detailed study on the magnetic phase transition (measurement of the critical exponents, determination of the actual magnetic structure) are currently carried on by neutron diffraction and heat capacity experiments on single-crystalline samples.

Possible routes towards the implementation of molecular gate for quantum computation have also been investigated. I presented our experimental characterization of Cr_7Ni rings linked together by supramolecular chemistry and showed that at least they are relatively stable and can be attached to one another without changing their properties. Since the magnetic signal is tiny (spin ground state of Cr_7Ni molecule is $S = 1/2$), the high sensitivity of Hall probes magnetometry is useful to study these systems down to the lowest accessible temperatures. In collaboration with the chemist group of Manchester (Prof. R. Winpenny) we are exploring more effective linking bridges as well as clusters with switchable interactions, that could be activated or de-activated for example with electromagnetic excitation, like visible light or microwaves. We are also planning to employ microwave pulses to perform rotations of the magnetization vector of the molecule, to directly study the coherent dynamic of the system.

Finally, I showed the experimental evidences of the high-temperature slow-relaxation of the magnetization in the Ni_{10} molecule and why it can not be explained within the conventional framework of phonon-assisted relaxations. In collaboration with the group of Prof. G. Amoretti (Parma) we developed a new model where resonant phonon trapping freezes the magnetization in a non equilibrium state, leading to a very slow dynamic. Other derivatives of the Ni_{10} molecule as well as different systems with similar band-like energy spectrum are under investigation.

All my measurements have been obtained on small crystals, containing a collection ($\approx 10^{14}$) of ordered identical molecules. However, many challenging ap-

plications, such as the implementation of quantum bits with magnetic nanoclusters, require single molecules to be addressed and hence magnetically detected. At present time, few experimental techniques reach such an impressive sensitivity [131]. In Chapter 3 I demonstrated the realization of Hall nano-probes by focused ion beam milling. These sensors have high flux sensitivity and can be also used for magnetic imaging with high spatial resolution. Moreover, they constitute a step towards the realization of probes of nanometer scale (≈ 10 nm) that, as I have already pointed out, can be capable to detect even single electron spin placed near the active area. Miniaturization of the sensor is fundamental to optimize the coupling with the magnetic flux originated by the sample. However, while charge depletion at the borders is the main difficult for semiconductor probes, metallic sensors are limited by their tiny Hall coefficient. We are currently exploiting two different technical strategies to overcome these issues: one is to employ control gate voltages over highly-doped 2DEG heterostructures, while the other is the use of graphene (i.e. a single layer of graphite) as the sensor material.

Depositing nano-electrodes to shrink the conductive channel is a known method, with which Quantum Wires and Quantum Point Contacts are usually made, measuring even the conduction of a single electron [132, 133]. Combining the four-electrodes geometry with alternative 2DEG materials, like $In_{0.75}Ga_{0.25}As/GaAs$ (that has zero Schottky barrier and hence less charge depletion than traditional 2DEG structures [134]) it will be possible to obtain Hall nano probes suitable for high sensitivity magnetometry.

On the other hand, graphene, or few layer graphite, or even thin film of high quality graphite, essentially show properties of a 2DEG that means low number of carriers (i.e. high Hall coefficient) and high mobility and hence high conductivity (i.e. low resistance values and low noise in electrical measurements in spite of the small number of carriers). Moreover, since graphite structures have shown to be of metallic nature, scalability to true nanometer sizes appears feasible [135–137].

We believe that with these strategies magnetometers with enough sensitivity to probe single magnetic molecules deposited on surfaces can be developed.

Acknowledgments

It's a real pleasure to thank all the people that helped me during the years of my Ph.D. fellowship in Modena.

First I want to thank my advisor prof. Marco Affronte for the possibility to carry my research activity, for his continuous help and support. Also thank to him and the CNR-INFM National Research Center S3 and the Dipartimento di Fisica, Università di Modena e Reggio Emilia for funding! Thanks to the other members of the Low Temperature laboratory, Alberto Ghirri and Dr. Marco Evangelisti, not only for the help in experimental measurements or data analysis (or manuscripts writing!), but most of all for their friendship.

All of the Hall probe used in this work (and not only) were made by the group of prof. Lucia Sorba, at the CNR-INFM TASC laboratory, in Trieste: Dr. Giorgio Biasol, Dr. Giorgio Mori, my Ph.D.-colleague Daniele Ercolani and Tomaž Mlakar. Thanks for all the discussions and all the work they made for me. Without them most of my activity would not have been possible.

I am extremely grateful to the theoretical group of Parma, Dr. Stefano Carretta, prof. Paolo Santini and prof. G. Amoretti. Thanks for all the calculations and especially for the instructive and fruitful discussions.

For the Hall nano-probes showed in Chapter 3 I am in deep debt with Dr. Gian Carlo Gazzadi, thanks for all the time spent milling my probes with FIB. Thank also to Dr. Alessandro di Bona, Dr. Caludia Menozzi and especially to Elena Angeli for the help in lithographic processes.

All of the molecular samples studied in this work are made by the chemist group of Manchester and the chemist group of Edinburgh: I am very grateful for this fruitful collaboration with prof. Winpenny, prof. Timco, prof. McInnes, prof. Brechin and all their co-workers.

Thanks to Dr. I. Sheikin for the time I spent at the high magnetic field laboratory in Grenoble. Thanks to Dr. W. Wernsdorfer and all the Grenoble group for all the stimulating and instructive discussions.

A special thank to my friends of the Physics Department (Ph.D. students and not) and especially to my dear friend feffe.

Thanks to my family, my parents Antonio and Gianna and my sister Antonella for their continuous support.

Finally, the most important acknowledgment is for Elena, old girlfriend and now darling wife. This thesis is dedicated to her.

Andrea Candini
Modena. January 2007

Bibliography

[1] O. Kahn. Molecular Magnetism. Wiley-WCH, New York 1993

[2] D. Gatteschi, R. Sessoli. Quantum Tunneling of Magnetization and Related Phenomena in Molecular Materials. *Angewandte Chemie International Edition* **42** (2003) 268

[3] B. Barbara. Quantum nanomagnet. *C.R. Physique* **6** (2005)

[4] M. Evangelisti, F. Luis, L.J. de Jongh, M. Affronte. Magnetothermal properties of molecule-based materials. *Journal of Materials Chemistry* **16** (2006) 2534-2549

[5] S.D. Bader. *Colloquium*: Opportunities in nanomagnetism. *Reviews of Modern Physics* **78** (January 2006)

[6] S.A. Wolf, D.D. Awschalom, R.A. Buhrman, J.M. Daughton, S. von Molnar, M.L. Roukes, A.Y. Chtchelkanova, D.M. Treger. Spintronics: A spin-based electronics vision for the future. *Science* **294** (2001) 1488-1495

[7] T. Lis. *Acta Crystallographica Section B* **36** (1980) 2042

[8] A. Caneschi, D. Gatteschi, R. Sessoli, A.L. Barra, L.C. Brunel, M. Guillot. Alternating current susceptibility, high field magnetization, and millimeter band EPR evidence for a ground S = 10 state in $[Mn_{12}O_{12}(Ch_3COO)_{16}(H_2O)_4]2CH_3COOH$ $4H_2O$. *Journal of the American Chemical Society* **113** (1991) 5873-5874

[9] R. Sessoli, D. Gatteschi, A. Caneschi, and M.A. Novak. Magnetic bistability in a metal-ion cluster. *Nature* (London) **365** (1993) 141

[10] M. Leuenberger, D. Loss. Quantum computing in molecular magnets. *Nature* **410** (2001) 789

[11] H.B. Heersche, Z. de Groot, J.A. Folk, H.S.J. van der Zant, C. Romeike, M.R. Wegewijs, L. Zobbi, D. Barreca, E. Tondello, A. Cornia. Electron transport through single Mn-12 molecular magnets. *Physical Review Letters* **96** (2006) 206801

[12] R.S. Popovic, Hall Effect Devices, Adam Hilger, Bristol, 1991

[13] N.W. Ashcroft, N.D. Mermin. Solid State Physics, Thomson Learning 1976

[14] Xin-Qi Li, F.M. Peeters, A.K. Geim. The Hall effect of an inhomogeneous magnetic field in mesoscopic structures. *Journal of Physics: Condensed Matter* **9** (1997) 8065-8073

[15] S. Liu, H. Guillou, A.D. Kent, G.W. Stupian, M.S. Leung. Effect of probe gempetry on the Hall response in an inhomogeneous magnetic field: a numerical study. *Journal of Applied Physics* **83** (1998) 6161-6165

[16] S.J. Bending, A. Oral. Hall effect in a highly inhomogeneous magnetic field distribution. *Journal of Applied Physics* **81** (1997) 3721-3725

[17] K.S. Novoselov, S.V. Morozov, S.V. Dubonos, M. Missous, A.O. Volkov, D.A. Christian, A.K. Geim. Submicron probes for Hall magnetometry in the extended temperature range from helium to room temperature. *Journal of Applied Physics* **93** (2003) 10053-10057

[18] G. Boero, M. Demierre, P.-A. Besse, R.S. Popovic. Micro Hall devices: performance, tachnologies and application. *Sensors and Actuoators A* **106** (2003) 314-320

[19] A.D. Kent, S. von Molnár, S. Gider, D.D. Awschalom. Properties and measurement of scanning tunneling microscope fabricated ferromagnetic particle arrays. *Journal of Applied Physics* **76** (1994) 6656-6660

[20] A.K. Geim, S.V. Dubonos, J.G.S. Lok, I.V. Grigorieva, J. C. Maan, L. Theil Hansens, P.E. Lindelof. Ballistic Hall micromagnetometry. *Applied Physics Letters* **71** (1997) 2379-2381

[21] A.M. Chang, H.D. Hallen, L. Harriott, H.F. Hess, H.L. Kao, J. Kwo, R.E. Miller, R. Wolfe, J. van der Ziel. Scanning Hall probe microscopy. *Applied Physics Letters* **61** (1992) 1974-1976

[22] A. Oral, S.J. Bending, M. Henini. Real-time scanning Hall probe microscopy. *Applied Physics Lettters* **69** (1996) 1324-1326

[23] S. Gider, J. Shi, D.D. Awschalom, P.F. Hopkins, K.L. Campman, A.C. Gossard, A.D. Kent, S. von Molnár. Imaging and magnetometry of switching in nanometer-scale iron particles. *Applied Physics Lettetrs* **69** (1996) 3269-3271

[24] J.G.S. Lok, A.K. Geim, J.C. Maan, S.V. Dubonos, L. Theil Kuhn, P.E. Lindelof. Memory effects in individual submicrometer ferromagnets. *Physical Review B* **58** (1998) 12201-12206

[25] D. Grundler, G. Meier, K.-B. Broocks, Ch. Heyn, D. Heitman. Magnetization of small arrays of interacting single-domain particles. *Journal of Applied Physics* **85** (1999) 6175-6177

[26] D. Schuh, J. Biberger, A. Bauer, W. Breuer, D. Weiss. Hall-Magnetometry on Ferromagnetic Dots and Dot Arrays. *IEEE Transactions on Magnetics* **37** (2001) 2091-2093

[27] Y. Li, P. Xiong, S. von Molnár, S. Wirth, Y. Ohno, H. Ohno. Hall magnetometry on a single iron nanoparticle. *Applied Physics Letters* **80** (2002) 4644-4646

[28] M. Rahm, M. Schneider, J. Biberger, R. Pulwey, J. Zweck, D. Weiss, V. Umansky. Vortex nulceation in submicrometer ferromagnetic disks. *Applied Physics Letters* **82** (2003) 4110-4112

[29] D.A. Brawner, N.P. Ong, Z.Z. Wang. Novel field-induced asymmetry in the remanent magnetization of the superconductor $YBa_2Cu_3O_7$. *Nature* **358** (1992) 567

[30] A.K. Geim, I.V. Grigorieva, S.V. Dubonos, J.G.S. Lok, J.C. Maan, A.E. Filippov, F.M. Peeters. Phase transitions in individual sub-micrometre superconductors. *Nature* **390** (1997) 259

[31] A. Oral, J.C. Barnard, S.J. Bending, I.I. Kaya, S. Ooi, T. Tamegai, M. Henini. Direct Observation of Melting of the Vortex Solid in $Bi_2Sr_2CaCu_2O_{8+\delta}$ Single Crystal. *Physical Review Letters* **80** (1998) 3610-3614

[32] A.K. Geim, S.V. Dubonos, I.V. Grigorieva, K.S. Novoselov, F.M. Peeters, V.A. Schweigert. Non-quantized penetration of magnetic field in the vortex state of superconductors. *Nature* **407** (2000) 55

[33] T. Fukumura, H. Sugawara, T. Hasegawa, K. Tanaka, H. Sakaki, T. Kimura, Y. Tokura. Spontaneous Bubble Domain Formation in a Layered Ferromagnetic Crystal. *Science* **284** (1999) 1969-1971

[34] A. Sandhu, H. Masuda, A. Oral, S.J. Bending. Room temperature magnetic imaging of magnetic storage media and garnet epilayers in the presence of external magnetic fields using a sub-micron GaAs SHPM. *Journal of Crystal Growth* **227-228** (2001) 899-905

[35] J. Bekaert, D. Buntix, C. van Haesendonck, V.V. Moshchalkov, J. de Boeck, G. Borghs, V. Metlushko. Noninvasive magnetic imaging and magnetization measurement of isolated mesoscopic Co rings. *Applied Physics Letters* **81** (2002) 3413-3415

[36] K.S. Novoselov, A.K. Geim, S.V. Dubonos, E.W. Hill, I.V. Grigorieva. Subatomic movements of a domain wall in the Peierls potential. *Nature* **426** (2003) 812

[37] R.B.G. Kramer, V.S. Egorov, V.A. Gasparov, A.G.M. Jansen, W. Joss. Direct Observation of Condon Domains in Silver by Hall Probes. *Physical Review Letters* **95** (2005) 267209

[38] P.-A, Besse, G. Boero, M. Demierre, V. Pott, R.S. Popovic. Detection of a single magnetic microbead using a miniaturized silicon Hall sensor. *Applied Physics Letters* **80** (2002) 4199-4201

[39] K. Togawa, H. Sanbonsugi, A. Lapicki, M. Abe, H. Handa, A. Sandhu. High-Sensitivity InSb Thin-Film Micro-Hall Sensor Arrays for Simultaneous Multiple Detection of Magnetic Beads for Biomedical Applications. *IEEE Transactions on Magnetics* **41** (2005) 3661-3663

[40] S.A. Solin, R.A. Stradling, T. Thio, J.W. Bennet. Thin, horizontal-plane Hall sensors for read heads in magnetic recording. *Measurement Science and Technology* **8** (1997) 1174-1181

[41] F.G. Monzon, M. Johnson, M.L. Roukes. Strong Hall voltage modulation in hybrid ferromagnet/semiconductor microstructures. *Applied Physics Letters* **71** (1997) 3087-3089

[42] M. Johnson, B.R. Bennett, M.J. Yang, M.M. Miller, B.V. Shanabrook. Hybrid Hall effect device. *Applied Physics Letters* **71** (1997) 974-976

[43] G. Boero, P.-A. Besse, R.S. Popovic. Hall detection of magnetic resonance. *Applied Physics Letters* **79** (2001) 1498-1500

[44] K. Petukhov, W. Wernsdorfer, A.-L. Barra, V. Mosser. Resonant photon absorption in Fe-8 single-molecule magnets detected via magnetization measurements. *Physical Review B* **72** (2005) 052401

[45] T. Schweinböck, D. Weiss, M. Lipinski, K. Eberl. Scanning Hall probe microscope with shear force distance control. *Journal of Applied Physics* **87** (2000) 6496-6498

[46] A. Sandhu, H. Masuda, A. Oral, S.J. Bending, A. Yamada M. Konagai. Room temperature scanning Hall probe microscopy using GaAs/AlGaAs and Bi micro-hall probes. *Ultramicroscopy* **91** (2002) 97-101

[47] Jin Jinshuang and Li Xin-Qi. Measurement of single electron spin with submicron Hall magnetometer. *Applied Physics Letters* **86** (2005) 143504

[48] M. Myronov, T. Irisawa, O.A. Mironov, S. Koh, Y. Shiraki, T.E. Whall, E.H.C. Parker. Extremely high room-temperature two-dimensional hole gas mobility in $Ge/Si_{0.33}Ge_{0.67}Si(001)$p-type modulation-doped heterostructures. *Applied Physics Letters* **80** (2002) 3117-3119

[49] A. Pross, A.I. Crisan, S.J. Bending, V. Mosser, M. Konczykowski. Second-generation quantum-well sensors for room-temperature scanning Hall probe microscopy. *Journal of Applied Physics* **97** (2005) 096105

[50] D. Petit, D. Atkinson, S. Johnston, D. Wood, R.P. Cowborn. Room temperature performance of submicron bismuth Hall probes. *IEE Proceedings -Science, Measurement Technology* **151** (2004) 127-130

[51] A. Sandhu, A. Okamoto, I. Shibasaki, A. Oral. Nano and micro Hall-effect sensors for room-temperature scanning hall probe microscopy. *Microelectronic Engineering* **73-74** (2004) 524-528

[52] A. Sandhu, K. Kurosawa, M. Dede, A. Oral. 50 nm Hall Sensors for Room Temperature Scanning Hall Probe Microscopy. *Japanese Journal of Applied Physics* **43** (2004) 777-778

[53] G. Boero, I. Utke, T. Bret, N. Quack, M. Torodova, S. Mouaziz, P. Kejik, J. Brugger, R.S. Popovic, P. Hoffman. Submicrometer Hall devices fabricated by focused electron-beam-induced deposition. *Applied Physics Letters* **86** (2005) 042503

[54] V. Cambel, D. Gregušová, J. Fedor, R. Kúdela, S.J. Bending. Scanning vector Hall probe microscopy. *Journal of Magnetism and Magnetic Materials* **272-276** (2004) 2141-2143

[55] A. Oral, M. Kaval, M. Dede, H. Masuda, A. Okamoto, I. Shibasaki, A. Sandhu. Room-Temperature Scanning Hall Probe Microscope (RT-SHPM) Imaging og Garnet FIlms Using New High-Performance InSb Sensors. *IEEE Transactions on Magnetics* **38** (2002) 2438-2440

[56] A. Sandhu, H. Masuda, H. Senoguchi, T. Togawa. A novel variable temperature scanning nano-Hall probe microscope system for large area magnetic imaging incorporating piezoelectric actuators maintained at room temperature. *Nanotechnology* **15** (2004) S410-S413

[57] L. Bokacheva, A.D. Kent, M.A. Walters. Crossover between Thermally Assisted and Pure Quantum Tunneling in Molecular Magnet Mn_{12}-Acetate *Physical Review Letters* **85** (2000) 4803-4806

[58] L. Sorace, W. Wernsdorfer, C. Thirion, A.-L. Barra, M. Pacchioni, D. Mailly, B. Barbara. Photon-assisted tunneling in a Fe_8 single-molecule magnet. *Physical Review B* **68** (2003) 220407(R)

[59] E. del Barco, A.D. Kent, E.M. Rumberger, D.N. Hendrickson, G. Christou. Symmetry of Magnetic Quantum Tunneling in Single Molecule Magnet Mn_{12}-Acetate. *Physical Review Letters* **91** (2003) 047203

[60] L. Rolland, V. Simonet, W. Wernsdorfer, L. Bogani, R. Sessoli. Micro-Hall magnetometry on a Co-organic chain compound. *Journal of Magnetism and Magnetic Materials* **272** (2004) 1079-1080

[61] E. del Barco, A.D. Kent, E.C. Yang, D.N. Hendrickson. Quantum Superposition of High Spin States in the Single Molecule Magnet Ni_4 *Physical Review Letters* **93** (2004) 157202

[62] W. Wernsdorfer, R. Clerac, C. Coulon, L. Lecren, H. Miyasaka. Quantum nucleation in a single-chain magnet. *Physical Review Letters* **95** (2005) 237203

[63] W. Wernsdorfer, M. Murugesu, G. Christou. Resonant tunneling in truly axial symmetry Mn-12 single-molecule magnets: Sharp crossover between thermally assisted and pure quantum tunneling. *Physical Review Letters* **96** (2006) 057208

[64] Quantum Design, *PPMS Hardware and Option Manual*. San Diego, CA, U.S.A. See also http://www.qdusa.com/products/ppms.html

[65] Kulicke and Soffa Industries, INC. *Model 4123 Universal Wedge Bonder Operation Manual*. Willow Groove, PA, U.S.A.

[66] P. Ǵutlich, Y. Garcia, T. Woike. Photoswitchable coordination compounds. *Coordination Chemistry Reviews* **219-221** (2001) 839-879

[67] C. Thirion, W. Wernsdorfer, D. Mailly. Switching of magnetization by nonlinear resonance studied in single nanoparticles. *Nature Materials* **2** (2003) 523-527

[68] M. Clemente-Leon, H. Soyer, E. Coronado, C. Mingotaud, C.J. Gomez-Garcia, P. Delhaes. Langmuir-Blodgett films of single-molecule nanomagnets. *Angewandte Chemie Interantional Edition* **37** (1998) 2842-2845

[69] A. Cornia, A.C. Fabretti, M. Pacchioni, L. Zobbi, D. Bonacchi, A. Caneschi, D. Gatteschi, R. Biagi, U. Del Pennino, V. De Renzi, L. Gurevich, H.S.J. Van der

Zant. Direct observation of single-molecule magnets organized on gold surfaces. *Angewandte Chemie Interantional Edition* **42** (2003) 1645-1648

[70] M. Cavallini, F. Biscarini, J. Gomez-Segura, D. Ruiz, J. Veciana. Multiple length scale patterning of single-molecule magnets. *Nanoletters* **3** (2003) 1527-1530

[71] J.S. Steckel, N.S. Persky, C.R. Martinez, C.L. Barnes, E.A. Fry, J. Kulkarni, J.D. Burgess, R.B. Pacheco, S.L. Stoll. Monolayer and multilayer films of [Mn12O12(O2CMe)(16)]. *Nanoletters* **4** (2004) 399-402

[72] R. Amigó, J.M. Hernandez, A. García Santiago, J. Tejada. Microwave absorption and magnetization tunnelling in Mn_{12}-acetate molecular cluster. *Physical Review B* **67** (2003) 220402(R)

[73] J.M. Herrera, V. Marvaud, M. Verdaguer, J. Marrot, M. Kalisz, C. Mathonièr. Reversible Photoinduced Magnetic Properties in the Heptanuclear Complex $[Mo^{IV}(CN)_2(CN\text{-}CuL)_6)]^{8+}$: a Photomagnetic High-Spin Molecule. *Angewandte Chemie International Edition* **43** (2004) 5468-5471

[74] R.J. Young, J.R.A. Cleaver, H. Ahmed. Characteristics of gas-assisted focused ion beam etching. *Journal Vacuum Science and Technology B* **11** (1993) 234-241

[75] M. Affronte, A. Ghirri, S. Carretta, G. Amoretti, S. Piligkos, G.A. Timco, R.E.P. Winpenny. Engineering molecular rings for magnetocaloric effect. *Applied Physics Letters* **84** (2004) 3468-3470

[76] C. Zimm, A. Jastrab, A. Sternberg, V.K. Pecharsky, K.A. Gschneidner Jr., M. Osborne, I. Anderson, in *Advances in Cryogenic Engineering* **43** (1998) 1759.

[77] V.K. Pecharsky, K.A. Gschneidner Jr. Magnetocaloric effect and magnetic refrigeration. *Journal of Magnetism and Magnetic Matererials* **200** (1999) 44-56

[78] K.A. Gschneidner Jr., A.O. Pecharsky, V.K. Pecharsky, in *Cryocoolers II*, R.S. Ross Jr. (Ed.), Kluwer Academic / Plenum Press, New York, 2001, p. 433.

[79] P. Debye. Some observations on magnetisation at a low temperature. Annalen der Physik **81** (1926) 1154-1160

[80] W.F. Giauque. A thermodynamic treatment of certain magnetic effects. A proposed method of producing temperatures considerably below 1 absolute. *Journal of the American Chemical Society* **49** (1927) 1864-1870

[81] R.D. McMichael, R.D. Shull, L.J. Swartzendruber, L.H. Bennett, R.E. Watson. Magnetocaloric effect in superparamagnets. *Journal of Magnetism and Magnetic Materials* **111** (1992) 29-33

[82] L.H. Bennett, R.D. McMichael, H.C. Tang, R.E. Watson. Monte Carlo simulations of the magnetocaloric effect in superferromagnetic clusters having uniaxial magnetic anisotropy. *Journal of Applied Physics* **75** (1994) 5493-5495

[83] X.X. Zhang, H.L. Wei, Z.Q. Zhang, L. Zhang. Anisotropic Magnetocaloric Effect in Nanostructured Magnetic Clusters. *Physical Review Letters* **87** (2001) 157203

[84] F. Torres, J.M. Hernández, X. Bohigas, J. Tejada. Giant and time-dependent magnetocaloric effect in high-spin molecular magnets. *Applied Physics Letters* **77** (2000) 3248-3250

[85] D.M. Low, L.F. Jones, A. Bell, E.K. Brechin, T. Mallah, E. Rivière, S.J. Teat, E.J.L. McInnes. Solvothermal Synthesis of a Tetradecametallic Fe^{III} Cluster. *Angewandte Chemie International Edition* **42** (2003) 3781-3784

[86] G. Rajaraman, J. Cano, E.K. Brechin, E.J.L. McInnes. Density functional calculations of a tetradecametallic iron(III) cluster with a very large spin ground state. *Chemical Communication* (2004) 1476

[87] V.K. Pecharsky, K.A. Gschneidner Jr. Magnetocaloric effect from indirect measurements: Magnetization and heat capacity. *Journal of Applied Physics* **86** (1999) 565-575

[88] A.L. Lima, K.A. Gschneidner Jr., V.K. Pecharsky, A.O. Pecharsky. Disappearance and reappearance of magnetic ordering upon lanthanide substitution in $(Er_{1-x}Dy_x)Al_2$. *Physical Review B* **68** (2003) 134409

[89] M. Evangelisti, F. Luis, F.L. Mettes, N. Aliaga, G. Aromí, G. Christou, L.J. de Jongh. Through quantum tunneling to dipolar order: the effect of varying magnetic

anisotropy in three structurally related Mn_4 molecular clusters. *Polyhedron* **22** (2003) 2169-2173

[90] M. Evangelisti, F. Luis, F.L. Mettes, N. Aliaga, G. Aromí, J.J. Alonso, G. Christou, L.J. de Jongh. Magnetic Long-Range Order Induced by Quantum Relaxation in Single-Molecule Magnets. *Physical Review Letters* **93** (2004) 117202

[91] A. Bino, D.C. Johnston, D.P. Goshorn, T.R. Halbert, E.I. Stiefel. $[Cr_4S(O_2CCH_3)_8(H_2O)_4](BF_4)_2H_2O$: Ferromagnetically Coupled Cr_4S Cluster with Spin 6 Ground State. *Science* **241** (1988) 1479-1481

[92] A. Morello, F.L. Mettes, F. Luis, J.F. Fernández, J. Krzystek, G. Aromí, G. Christou, L.J. de Jongh. Long-Range Ferromagnetic Dipolar Ordering of High-Spin Molecular Clusters. *Physical Review Letters* **90** (2003) 017206

[93] A. Morello, F.L. Mettes, O.N. Bakharev, H.B. Brom, L.J. de Jongh, F. Luis, J.F. Fernández, G. Aromí. Magnetic dipolar ordering and relaxation in the high-spin molecular cluster compound Mn_6. *Physical Review B* **73** (2006) 134406

[94] P. Panissod and M. Drillon in *Magnetism: molecules to materials IV*, edited by J.S. Miller and M. Drillon (Wiley-VCH, Weinheim, Germany, 2002), Chapter 7.

[95] J.F. Fernández, J.J. Alonso. Ordering of dipolar Ising crystals. *Physical Review B* **62** (2000) 53-56; see also *ibid.* **65**, 189901(E) (2002); *ibid.* **73**, 024412 (2006).

[96] J.F. Fernández. Dipolar ordering of molecular magnets. *Physical Review B* **66** (2002) 064423

[97] X. Martínez-Hidalgo, E.M. Chudnovsky, A. Aharony. Dipolar ordering in Fe_8?. *Europhysics Letters* **55**(2001) 273-279

[98] M. Affronte, J.C. Lasjaunias, W. Wernsdorfer, R. Sessoli, D. Gatteschi, S.L. Heath, A. Fort A. Rettori. Magnetic ordering in a high-spin Fe_19 molecular nanomagnet. *Physical Review B* **66** (2002) 064408

[99] A. Yamaguchi, N. Kusumi, H. Ishimoto, H. Mitamura, T. Goto, N. Mori, M. Nakano, K. Awaga, J. Yoo, D.N. Hendrickson, G. Christou. Observation of Magnetic

Transition in Quantum Nanomagnet Mn_4Br. *Journal of the Physical Society of Japan* **71** (2002) 414-417

[100] M. Evangelisti, A. Candini, A. Ghirri, M. Affronte, E.K. Brechin, E.J.L. McInnes. Spin-enhanced magnetocaloric effect in molecular nanomagnets. *Applied Physics Letters* **87** (2005) 072504

[101] F. Luis, J. Campo, J. Gómez, G.J. McIntyre, J. Luzón, D. Ruiz-Molina. Long-Range Ferromagnetism of Mn_12 Acetate Single-Molecule Magnets under a Transverse Magnetic Field. *Physical Review Letters* **95** (2005) 227202

[102] G.W. Powell, H.N. Lancashire, E.K. Brechin, D. Collison, S.L. Heath, T. Mallah, W. Wernsdorfer. Building Molecular Minerals: All Ferric Pieces of Molecular Magnetite. *Angewandte Chemie International Edition* **43** (2004) 5772-5775

[103] Experimental report No. RB510053, Instr. GEM, ISIS, Rutherford Appleton Laboratory, (2005); Experimental report No. CNBC-615, Instr. C2, Canadian Neutron Beam Centre, (2006)

[104] F. Troiani A. Ghirri, M. Affronte, P. Santini, S. Carretta, G. Amoretti, S. Piligkos, G.A. Timco, R.E.P. Winpenny. Molecular Engineering of Antiferromagnetic Rings for Quantum Computation. *Physical Review Letters* **94** (2005) 207208

[105] M.A. Nielsen, I.L. Chuang. Quantum computation and quantum information, Cambridge University Press (2000).

[106] F. Meier, J. Levy, D. Loss. Quantum Computing with Spin Cluster Qubits. *Physical Review Letters* **90** (2003) 047901

[107] F. Meier, J. Levy, D. Loss. Quantum computing with antiferromagnetic spin clusters. *Physical Review B* **68** (2003) 134417

[108] D. Loss, D.P. DiVincenzo. Quantum computation with quantum dots. *Physical Review A* **57** (1998) 120-126

[109] F.K. Larsen, E.J.L. McInnes, H. El Mkami, J. Overgaard, S. Piligkos, G. Rajaraman, E. Rentschler, A.A. Smith, G.M. Smith, V. Boote, M. Jennings, G.A. Timco,

R.E.P. Winpenny. Synthesis and chracterization of heterometallic [Cr7M] wheels. *Angewandte Chemie International Edition* **42** (2003) 101-105

[110] M. Affronte, F. Troiani, A. Ghirri, A. Candini, M. Evangelisti, S. Carretta, P. Santini, G. Amoretti, S. Piligkos, G.A. Timco, R.E.P. Winpenny. AF molecular rings for quantum computation. *Polyhedron* **24** (2005) 2562-2567

[111] S. Carretta, P. Santini, G. Amoretti, M. Affronte, A. Ghirri, I. Sheikin, S. Piligkos, G.A. Timco, R.E.P. Winpenny. Topology and spin dynamics in magnetic molecules. *Physical Review B* **72** (2005) 060403

[112] R. Caciuffo, T. Guidi, G. Amoretti, S. Carretta, E. Liviotti, P. Santini, C. Mondelli, G.A. Timco, C.A. Muryn, R.E.P. Winpenny. Spin dynamics of heterometallic Cr7M wheels (M=Mn, Zn, Ni) probed by inelastic neutron scattering. *Physical Review B* **71** (2005) 174407

[113] E. Liviotti, S. Carretta, G. Amoretti. S-mixing contributions to the high-order anisotropy terms in the effective spin Hamiltonian for magnetic clusters. *Journal of Chemical Physics* **117** (2002) 3361-3368

[114] W. Wernsdorfer, D. Mailly, G.A. Timco, R.E.P. Winpenny. Resonant photon absorption and hole burning in Cr7Ni antiferromagnetic rings. *Physical Review B* **72** (2005) 060409

[115] A. Ardavan, O. Rival, J.J.L. Morton, S.J. Blundell, A.M. Tyryshkin, G.A. Timco, R.E.P. Winpenny. Will spin-relaxation times in molecular magnets permit quantum information processing? quant-ph/0609143 *accepted for pubblication* (2006)

[116] F. Troiani, M. Affronte, P. Santini, S. Carretta, G. Amoretti. *Physical Review Letters* Proposal for Quantum Gates in Permanently Coupled Antiferromagnetic Spin Rings without Need of Local Fields. **94** (2005) 190501

[117] M. Affronte, I. Casson, M. Evangelisti, A. Candini, S. Carretta, C.A. Muryn, S.J. Teat, G.A. Timco, W. Wernsdorfer, R.E.P. Winpenny. Linking Rings through Diamines and Clusters: Exploring Synthetic Methods for Making Magnetic Quantum Gates. *Angewandte Chemie International Edition* **44** (2005) 6496-6500

[118] M.A. Golubnichaya, S.E. Nefedov, I.B. Baranovskii, I.A. Olshnitskaya, O.G. Ellert, V.M. Novotortsev, L.T. Eremenko, D.A. Nesterenko. *Zhurnal Neorganicheskoi Khimii* **41** (1996) 2029-2043

[119] I.L. Eremenko, S.E. Nefedov, A.A. Sidorov, M.A. Golubnichaya, P.V. Danilov, V.N. Ikorskii, Y.G. Shvedenkov, V.M. Novotortsev, I.I. Moiseev. Bi- and Mononuclear Nickel(II) Trimethylacetate Complexes with Pyridine Bases as Ligands. *Inorganic Chemistry* **38** (1999) 3764-3773

[120] F.A. Cotton, R.A. Walton. Multiple Bonds Between Metal Atoms, 2nd Ed., Clarendon Press, Oxford, 1993

[121] F. Ritort, P. Sollich. Glassy dynamics of kinetically constrained models. *Advances in Physics* **52** (2003) 219-342

[122] W. Wernsdorfer, M. Murugesu, G. Christou. Resonant Tunneling in Truly Axial Symmetry Mn_{12} Single-Molecule Magnets: Sharp Crossover between Thermally Assisted and Pure Quantum Tunneling. *Physical Review Letters* **96** (2006) 057208

[123] A. Fort, A. Rettori, J. Villain, D. Gatteschi, R. Sessoli. Mixed Quantum-Thermal Relaxation in Mn_{12} Acetate Molecules. *Physical Review Letters* **80** (1998) 612-615

[124] P. Santini, S. Carretta, E. Liviotti, G. Amoretti, P. Carretta, M. Filibian, A. Lascialfari, E. Micotti. NMR as a Probe of the Relaxation of the Magnetization in Magnetic Molecules. *Physical Review Letters* **94** (2005) 77203

[125] P.W. Anderson. Spectral Diffusion, Phonons, and Paramagnetic Spin-Lattice Relaxation. *Physical Review* **114** (1959) 1002-1005

[126] R. Shaw, I.S. Tidmarsh, R. H. Laye, B. Breeze, M. Helliwell, E.K. Brechin, S.L. Heath, M. Murrie, S. Ochsenbein, H.-U. Gdel, E.J.L. McInnes. Supertetrahedral decametallic Ni(II) clusters directed by 6-tris-alkoxides. *Chemical Communication* (2004) 1418

[127] A. Abragam, B. Bleaney. Electron paramagnetic resonance of transition ions. Clarendon Press, Oxford, 1970

[128] P.L. Scott, C.D. Jeffries. Spin-Lattice Relaxation in Some Rare-Earth Salts at Helium Temperatures; Observation of the Phonon Bottleneck. *Physical Review* **127** (1962) 32-51

[129] D.L. Huber. Trapping of a Resonant Phonon in a Paramagnetic Spin System. *Physical Review* **142** (1966) 137-142

[130] A. Mukhin, B. Gorshunov, M. Dressel, C. Sangregorio, D. Gatteschi. Optical spectroscopy of crystal-field transitions in the molecular magnet Fe_8. *Physical Review B* **63** (2001) 214411

[131] J.-P. Cleziou, W. Wernsdorfer, V. Bouchiat, Th. Ondarçuhu, M. Monthioux. Carbon nanotube superconducting quantum interference device. *Nature Nanotechnology* **1** (2006) 53-59

[132] M.A. Topinka, B.J. LeRoy, R.M. Westervelt, S.E.J. Shaw, R. Fleischmann, E.J. Heller, K.D. Maranowski, A.C. Gossard. Coherent branched flow in a two-dimensional electron gas. *Nature* **410** (2001) 183

[133] J.M. Elzerman, J.M. Elzerman, R. Hanson, L.H. Willems van Beveren, B. Witkamp, L.M.K. Vandersypen, L.P. Kouwenhoven. Single-shot read-out of an individual electron spin in a quantum dot. *Nature* **430** (2004) 431

[134] F. Carillo, G. Biasiol, D. Frustaglia, F. Giazotto, L. Sorba, F. Beltram. $In_{0.75}Ga_{0.25}As$ on GaAs submicron rings and their application for coherent nanoelectronic devices. *Physica E* **32** (2002) 53-56

[135] K.S. Novoselov, A.K. Geim, S.V. Morozov, D. Jiang, Y. Zhang, S.V. Dubonos, I.V. Grigorieva, A.A. Firsov. Electric Field Effect in Atomically Thin Carbon Films. *Science* **306** (2004) 666

[136] Y. Zhang, Y.-W. Tan, H.L. Stormer, P. Kim. Experimental observation of the quantum Hall effect and Berry's phase in graphene. *Nature* **438** (2005) 201

[137] K.S. Novoselov, A.K. Geim, S.V. Morozov, D. Jiang, M.I. Katsnelson, I.V. Grigorieva, S.V. Dubonos, A.A. Firsov. Two-dimensional gas of massless Dirac fermions in graphene. *Nature* **438** (2005) 197

Curriculum Vitae

Andrea CANDINI
Born in Modena (MO), 10 June 1979
Address: c.so Adriano 96, 41100 Modena (MO) ITALY
mail: candini.andrea@unimore.it
Tel: (mobile phone) 340 30 40 360

Professional experiences

- **2004 - today**
  Ph.D. fellowship, CNR-INFM National Research Centre S3 (Modena) and Dipartimento di Fisica, Università di Modena e Reggio Emilia. Research subject: study of the magnetic properties of molecular magnets. My research activity was primary focused to develop the experimental technique of Hall micro-probe magnetometry to measure the magnetization of small crystals of molecular magnets. I implemented this technique in the Quantum Design PPM-system in the low temperatures laboratory, in Modena. I also employed different experimental methods (AC/DC magnetometry, Heat Capacity, Torque) and worked in different laboratories (Low Temperatures laboratory in Modena and Grenoble High Field Laboratory in Grenoble, France) using different equipments and cryostats. A significant part of my activity was also to develop novel Hall sensors of nano-metric

sizes to improve flux resolution and detect small magnetic objects. These sensors are fabricated by lithography (optical and electron beam) and focused ion beam milling.
Supervisor: prof. Marco Affronte (affronte@unimore.it).
Other contact: dr. Marco Evangelisti (evange@unimore.it)

- **November - December 2003**
  Collaboration with INFM - Dipartimento di Fisica, Università di Modena e Reggio Emilia. Research subject: fabrication and characterization of Hall micro-probes Scientific Advisor: prof. Marco Affronte.

- **August 2002**
  Neutron diffraction measurements, at ROTAX diffractometer, ISIS neutron source, Rutherford Appleton Laboratory, Didcot, UK. Experimental Report RB13463 (18 July 2003) Topic: magnetic structures of the intermetallic compounds Mn_{5-x} Fe_x Si_3 (x = 0, 1, 2, 3, 3.5, 4) The data were refined using the Rietveld method and analyzed for my laurea thesis.
  Tutors: prof. O. Moze(moze@unimore.it); Dr. W. Kockelmann

Education

- **2004 - today**
  Ph.D. student, XIX ciclo, CNR-INFM National Research Centre S3 (Modena) and Dipartimento di Fisica, Università di Modena e Reggio Emilia.
  Thesis title: "Hall probe magnetometry for the study of molecular nanomagnets"
  Tutor: prof. Marco Affronte.

- **26 Sept 2003**
  Laurea degree in Physics at Università degli Studi di Modena e Reggio Emilia. Thesis title: "Diffrazione Neutronica e Strutture Magnetiche dei

Composti Intermetallici Mn_{5-x} Fe_x Si_3 (x = 0, 1, 2, 3, 3.5, 4)".
Supervisor: prof. O. Moze.
Mark: 110/100 cum laude.

- **July 1998**
  High School degree "Diploma di Maturità Scientifica" at "Liceo Scientifico Statale A. Tassoni", Modena.
  Mark: 60/60

Other Activities

Teaching :

Assistant of the course of "Electromagnetismo I" for physics and mathematics students (years 04-05 and 05-06)

Schools :

- IFF Spring School "Magnetism goes nano" 14-25 February 2005, Juelich, Germany
- Scuola SISM "Focused Ion Beam: nanostrutturazione e analisi 3d dei materiali", 20-22 Settembre 2004, Modena, Italy
- INFM-ICTP Spring School on "Magnetic Properties of condensed matter investigated by neutron scattering and synchrotron radiation", 19-28 May 2003, Abdus Salam ICTP - Trieste, Italy
- VI Scuola di Spettroscopia Neutronica "Francesco Paolo Ricci": "I neutroni come sonda microscopica di sistemi disordinati"; 23 Settembre - 3 Ottobre 2002, Palau (SS), Italy

Conferences and Workshops :

- European Conference on Molecular Magnetism (ECMM), 10-15 October 2006, Tomar, Portugal.
  "Effects of opening antiferromagnetic spin rings"(Poster)
- International Conference on Magnetism (ICM), 20-25 August 2006, Kyoto, Japan.
  "Hall nano probes fabricated by focused ion beam"(Oral)
- MagMaNet Advanced Workshop on "Organizing and Addressing Molecules on Surfaces (OAMS)", 24-28 May 2006, Platja de Aro - Bracelona, Spain.
  "Hall nano-probes fabricated by focused ion beam" (Poster)
- MMD Meeting, 22-24 June 2005, Genova, Italy.
  "Hall μ-probes for magnetization measurements" (Poster)
  "Focused-Ion-Beam Fabricated Submicrometer Hall probes for Magnetometry and Magnetic Scanning Microscopy" (Poster)

List of Publications

1. **Candini A** Gazzadi GC, di Bona A, Affronte M, Ercolani D, Biasiol G and Sorba L, "Focused Ion Beam Patternd Hall nano-sensors", JOURNAL OF MAGNETISM AND MAGNETIC MATERIALS, *in press* (2007)

2. Carretta S, Santini P, Amoretti G, Affronte M, **Candini A**, Ghirri A, Tidmarsh IS, Laye RH, Shaw R, McInnes EJL, "High-Temperature Slow Relaxation of the Magnetization in Ni10 Magnetic Molecule", PHYSICAL REVIEW LETTERS **97**, 207201 (2006)

3. Evangelisti, M, **Candini, A**, Ghirri, A, Affronte, M, Powell, GW, Gass, IA, Wood, PA, Parsons, S, Brechin, EK, Collison, D, Heath, SL, "Tunable dipolar magnetism in high-spin molecular clusters", PHYSICAL REVIEW LETTERS **96**, 167202 (2006)

4. **Candini A**, Gazzadi GC, di Bona A, Affronte M, Ercolani D, Biasiol G and Sorba L, "Hall nano-probes fabricated by focused ion beam", NANOTECHNOLOGY **17** 2105, (2006)

5. Affronte M, Troiani F, Ghirri A, **Candini A**, Evangelisti M, Carretta S, Santini P, Amoretti G, Piligkos S, Timco G and Winpenny REP, "AF molecular rings for quantum computation", POLYHEDRON 24, 2562 (2005)

6. Evangelisti M, **Candini A**, Ghirri A, Affronte M, Piligkos S, Brechin EK and McInnes EJL, "Molecular nanoclusters as magnetic refrigerants: The case of Fe-14 with very large spin ground-state", POLYHEDRON **24**, 2573 (2005)

7. Affronte M, Casson I, Evangelisti M, **Candini A**, Carretta S, Muryn C, Teat SJ, Timco GA, Wernsdorfer W and Winpenny REP, "Linking rings through diamines and clusters: Exploring synthetic methods for making magnetic quantum gates", ANGEWANDTE CHEMIE-INTERNATIONAL EDITION **44**, 6496 (2005)

8. Evangelisti M, **Candini A**, Ghirri A, Affronte M, Brechin EK and McInnes EJL, "Spin-enhanced magnetocaloric effect in molecular nanomagnets", APPLIED PHYSICS LETTERS **87**, 072504 (2005)

9. Carretta S, Santini P, Amoretti G, Guidi T, Caciuffo R, **Candini A**, Cornia A, matteschi D, Plazanet M and Stride JA, "Intra- and inter-multiplet magnetic excitations in a tetrairon(III) molecular cluster", PHYSICAL REVIEW B, **70**, 214403 (2004)

10. **Candini A**, Moze O, Kochelmann W, Cadogan J, Bruck E and Tegus O, "A Revised Magnetic Phase Diagram for Fex Mn5-x Si3 Intermetallics", JOURNAL OF APPLIED PHYSICS **95**, 6819 (2004)